NATIONAL AERONAUTICS AND SPACE ADMINISTRATION

Technical Memorandum No. 33-236

Mars Entry and Landing Capsule

W. J. Carley
Senior Author and Editor

jpl JET PROPULSION LABORATORY
CALIFORNIA INSTITUTE OF TECHNOLOGY
PASADENA, CALIFORNIA

July 1, 1965

NATIONAL AERONAUTICS AND SPACE ADMINISTRATION

Technical Memorandum No. 33-236

Mars Entry and Landing Capsule

W. J. Carley
Senior Author and Editor

P. K. Eckman

P. K. Eckman, *Manager*
Advanced Missions,
Advanced Technical Studies Office

M. E. Alper

M. E. Alper, *Manager*
Applied Mechanics Section

JET PROPULSION LABORATORY
CALIFORNIA INSTITUTE OF TECHNOLOGY
PASADENA, CALIFORNIA

July 1, 1965

Prepared Under Contract No. NAS 7-100
National Aeronautics & Space Administration

CONTENTS

CONTENTS (Cont'd)

TABLES

TABLES (Cont'd)

FIGURES

FIGURES (Cont'd)

FIGURES (Cont'd)

FOREWORD

The results reported here are based on the work done in one phase of a continuing study of a Mars entry capsule design. More work and study will be needed before a complete analysis of related problems and constraints is available.

ACKNOWLEDGMENT

The following authors provided the information contained herein: R. Bamford, J. Brayshaw, W. Carley, L. Gold, J. Hasbrouck, W. Layman, J. Long, J. Lucas, R. Nagler, T. Thostesen. The task of coordinating, organizing, and compiling the material was performed by W. Carley.

ABSTRACT

The problems involved in delivering an *Apollo*-type entry capsule to Mars, entering and descending through its atmosphere, and placing a scientific payload on its surface are probed in some depth. Results indicating the feasibility and complexity of various approaches to this mission are given.

I. INTRODUCTION AND GUIDELINES

Landing a scientific payload—even a payload of modest capabilities—on the surface of Mars involves many unique functions and operations. This report presents the results of a study in which many of the problems of descent and landing operations were considered in some depth. Major objectives were to size the structure and heat shields and to uncover problem areas in the capsule and payload. A JPL internal communication (Ref. 1) contains information about the problems considered here but is related to a smaller capsule. Generally, these problems are studied in more detail here.

In reading this report it should be remembered that several guidelines and constraints were adopted at the outset which influenced the study results; conclusions reached might not be valid if they were replaced or changed. These guidelines and constraints include:

1. Use of Apollo-type capsule shape.
2. Consideration of two descent modes:
   a. Ballistic to impact (with parachute experiment).
   b. Ballistic entry with the parachute as a prime terminal decelerator.
3. Conformance to existing *Saturn IB/Centaur* shroud envelope.
4. Spacecraft to support capsule during launch.
5. Communications requirement to include:
   a. VHF relay link for pre-entry and entry.
   b. S-band direct link on landed payload.
6. Capsule shell to be rf-transparent.
7. Science capabilities:
   a. Entry science data to be transmitted on relay link and stored in landed payload for playback after impact.
   b. Landed science designed for:
      (1) High-g impact survival sphere (ballistic mode).
      (2) Parachute landing (parachute mode).
8. Mission life for landed science:
   a. 1½ days for 7b(1).
   b. 6 months for 7b(2).

This study reflects the influence of several disciplines. Accordingly, the study was divided into sections, each of which greatly influenced the others. An attempt was made to keep all results consistently factored into the other sections. However, some results were derived late in the study period and are not reflected throughout this report.

II. SUMMARY OF STUDY RESULTS

Study results are summarized as follows:

1. The impact velocity for the ballistic mode is so high for the design atmosphere that no landed payload exists using current properties of balsa wood and omnidirectional attenuator. There are some indications of an increase in these capabilities, but the payload will still be small in the ballistic mode. Descent payload capability exists, but all data would have to be relayed to the spacecraft prior to capsule impact.

2. The parachute mode of terminal deceleration makes a landed payload feasible if the center-of-gravity location can be kept within critical limits. The two-stage parachute configuration considered in this study does not meet this criterion. Using only a subsonic parachute appears to bring the center of gravity within critical limits, but it is outside the range used in this study's trajectory analyses. Entering the atmosphere at a low angle and controlling the angle of attack to 90 deg improves the payload capability significantly.

3. The Mars surface and wind definitions have a pronounced effect on the landed payload weight.

4. The landed payload operations are very complex and the complexity increases with the sophistication of the scientific instruments.

5. Spherical payloads capable of omnidirectional impact are practicable only for small payloads supporting up to 50 lb of scientific instruments. Landing of larger scientific payloads will require control which will limit the landing attitude of the payload system.

6. Structural shell and heat shield weights comprise ⅔ to ¾ of the capsule weight for a 90-deg path angle entry case and slightly more than 50% for the 45-deg path angle entry case.

7. Landed payload configurations show that direct-link scientific instrument deployment and antenna orientation will require removal of the impact attenuation materials after impact. A flotation scheme of antenna orientation shows promise if science does not have to be deployed.

8. Fabrication of the capsule shell from fiberglass sandwich material will require an extension of the current practices to meet the weight and dimensional tolerances required for a large, low-ballistic-coefficient entry body.

9. Temperature control of a payload on the surface of Mars will require good thermal isolation from the Mars environment. Removal of the impact attenuator material for antenna and instrument deployment will make this difficult to accomplish.

10. The low entry path angle trajectory controls the heat shield weight requirements, though by only about 10%. The heat shield function is essentially one of insulation rather than ablation.

11. A study should be made to minimize the structure plus heat shield weight as a function of the temperature at their interface.

12. The forebody heat shield weight must be increased by about 15% to accommodate an rf transparency requirement.

13. The heat shield weight decreases by 15% if the entry velocity is decreased from 25,000 to 23,000 ft/sec. Decelerations for which the structure is designed also decrease.

14. Provision for passive (aerodynamic) rearward entry capability decreases the landed payload.

15. A capsule diameter increase causes the peak deceleration and impact velocity for steep entry angles to increase slightly. Little effect is shown on the altitude for parachute deployment.

16. The parachute system should reduce the payload impact velocity to 100–150 ft/sec to maximize the landed payload.

17. The current SIB shroud envelope constrains the capsule size to 16 ft (Apollo-type shape), with the spacecraft on the bottom configuration. However, the space vehicle weight allocation to the capsule may be an overriding size limitation (except for low ballistic coefficients).

18. A preliminary investigation was made of a balloon-type gas bag, with the payload suspended in its center. This device serves as a combined decelerator and impact attenuator. Sufficient advantages were found to warrant further analytical and experimental study.

19. Continuing effort is required in every area investigated to refine analyses and verify assumptions used. All areas need investigation to more depth to uncover the problems which must be solved before a significantly large payload can successfully return scientific data to Earth.

III. TRAJECTORY DYNAMICS, MARS LANDER ENTRY

Capsule dynamics during entry have an important bearing on capsule design. Aeroshell structure and heat shield, internal black boxes, etc., will be designed with regard to the environment produced by the history of entry motion; that is, varying inertial and aerodynamic loads, attitude changes, thermal inputs, etc.

This study was performed using the JPL planetary entry dynamic trajectory program on the JPL IBM 7094 computer. This program can describe the motion of a body in six degrees of freedom. However, for easier interpretation and separation of effects, only planar motion (pitch rotation and altitude and range translation) was investigated. Aerodynamic coefficients of an *Apollo*-type entry shape were assumed. The planet was assumed to be spherical and rotating. Initial altitude was 800,000 ft; wind was assumed calm. Capsule moments of inertia were estimated from analytical models of weight distribution as an aeroshell plus forward-placed cylindrical payload. No configuration change was made from entry to impact.

A. Design Parameters

More than 85 dynamic trajectories with the *Apollo* shape were computed. Comparisons of these computations with others made on blunt cone and flare shapes are reported in Ref. 2. The initial conditions, lander ballistic coefficients, size, and atmosphere model were the primary inputs varied. Not all combinations of parameters were investigated, but the following are the values used in each parameter category (values to be emphasized are indicated by asterisks):

Entry velocity V_E, Kft/sec 19, 21, 23, 25*

Ballistic coefficient ($M/1.4A$), slugs/ft^2 . . . . . 0.187*, 0.26, 35*

Corresponding gross weight, lbs (at $D = 16$ ft) 1700, 2360, 3170

Center of gravity (from nose)/D 0.12, 0.17*

Lateral maximum diameter, ft 13, 16*, 19

Initial angle of attack (α_E), deg 0, 90, 170*

Initial flight path angle ($-\gamma_E$), deg 20, 45, 90*

Atmosphere model (see Table 1 and Ref 3) 5*, 6*, 10

Table 1. Properties of the Mars atmosphere models

Property	Symbol	Dimension	M69-5	M69-6	M69-10
Surface pressure	p_0	mb lb/ft^2	14 29.2	14 29.2	14 29.2
Surface density	ρ_0	(gm/cm^3)10^5 (slugs/ft^3)10^5	1.74 3.38	1.74 3.38	2.62 5.09
Surface temperature	T_0	°K °R	300 540	300 540	200 360
Stratospheric temperature	T_S	°K °R	100 180	260 468	100 180
Acceleration of gravity at surface	g	cm/sec^2 ft/sec^2	375 12.3	375 12.3	375 12.3
Composition CO_2 (by mass) CO_2 (by vol) N_2 (by mass) N_2 (by vol)			 28.2 20.0 71.8 80.0	 28.2 20.0 71.8 80.0	 28.2 20.0 71.8 80.0
Molecular weight	M	mol^{-1}	31.2	31.2	31.2
Specific heat of mixture	C_p	cal/gm-°C	0.228	0.234	0.225
Specific heat ratio	γ		1.39	1.37	1.39
Adiabatic lapse rate	Γ	°K/km °R/1000 ft	−3.93 −2.16	−3.83 −2.10	−3.98 −2.18
Tropopause altitude	h_T	km kilo/ft	50.9 167	10.4 34.1	25.1 82.4
Inverse scale height (stratosphere)	β	km^{-1} ft^{-1} × 10^5	0.140 4.26	0.0541 1.65	0.140 4.26
Mean surface wind speed	$\bar{v}$	ft/sec	100	100	100
Peak surface wind speed[a]	v_{max}	ft/sec	330	330	330
Mean vertical Wind gradient	$\frac{d\bar{v}}{dh}$	ft/sec/1000 ft	2	2	2

[a]The parameter has been scaled with surface pressure rather than surface density. The difference resulting from various surface temperatures will be small.

B. Parameter Variations

Variations of the above parameters produced motion and environmental histories which include the following resultant lander performance and usage.

1. Angle-of-attack stability, defining distribution of thermal input to surface of entry body.
2. Altitude–velocity relationships available, for terminal decelerator deployment.
3. Accelerations for structural design.
4. Impact velocity—influencing payload shock protection design for ballistic lander.
5. Velocity vs density profiles for heat shield design; reported in Section III.
6. Gross entry time, look angle, and communications blackout period considerations for approach system sequencing.
7. Comparative effects of possible atmospheric variations on entry conditions.

Figures 1 through 7 present the following selected effects as functions of lander ballistic coefficient and diameter, with initial conditions α_E and γ_E as parameters, the purpose being to display general trends:

1. Peak axial acceleration.
2. Impact velocity.
3. Altitude when slowed to Mach 3.
4. Angle-of-attack envelope at peak convective heating rate.

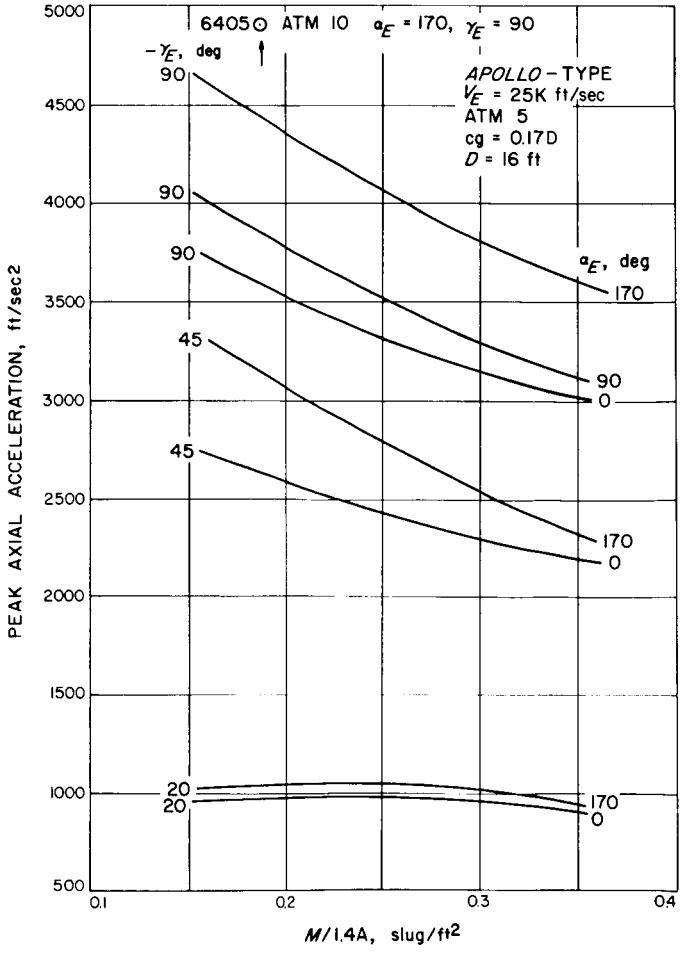

Fig. 1. Effect of capsule ballistic coefficient on peak axial acceleration

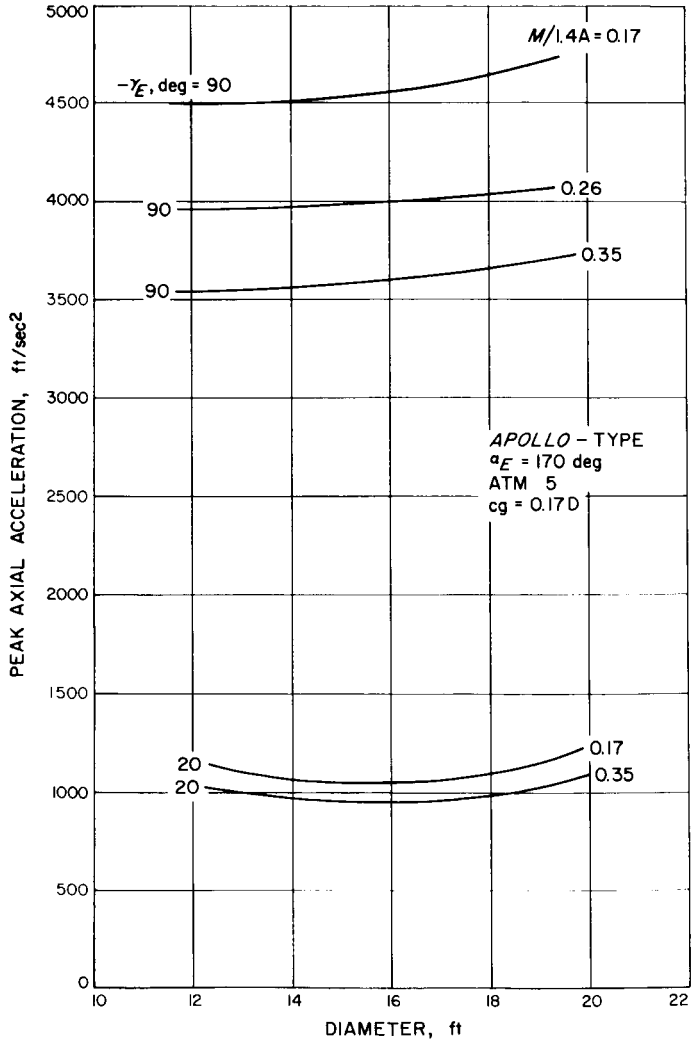

Fig. 2. Effect of capsule diameter on peak axial acceleration

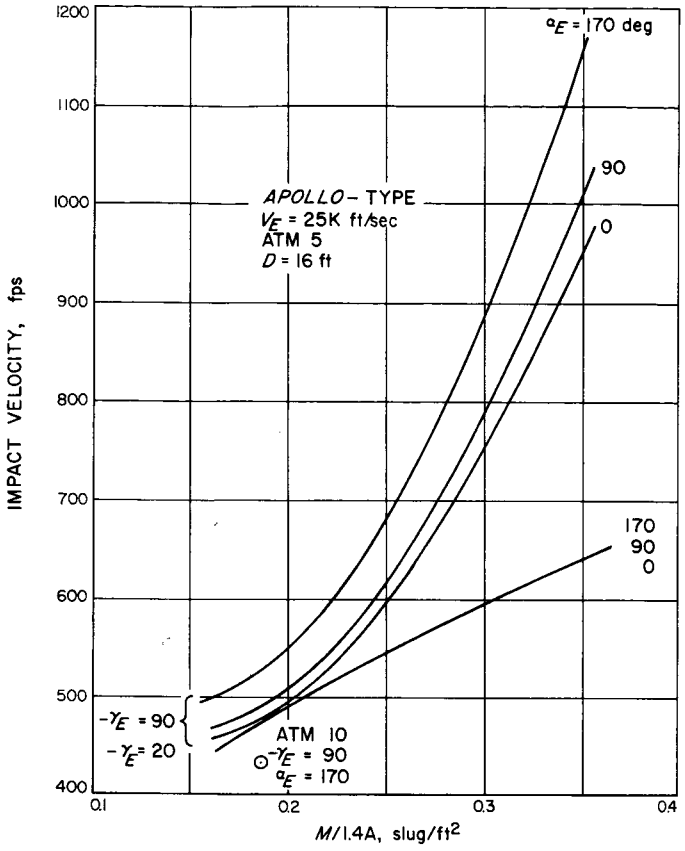

Fig. 3. Effect of capsule ballistic coefficient on impact velocity

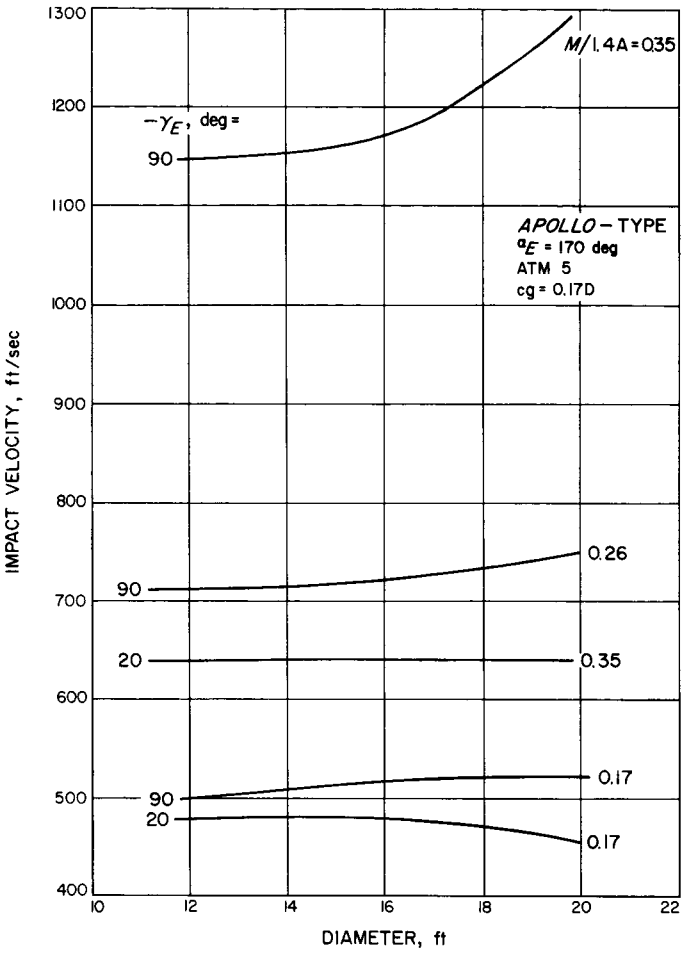

Fig. 4. Effect of capsule diameter on impact velocity

The effects of variations in design parameters on the performance of an *Apollo*-shaped Mars lander are discussed in the following subsections.

1. Ballistic Coefficient

Peak axial acceleration a_{max} decreases as ballistic coefficient increases. This decrease is due to penetration of the troposphere before a_{max} has occurred, producing part of the preceding drag impulse in an environment whose density gradient is less severe than that in the stratosphere.

Impact velocity increases rapidly with increase in ballistic coefficient, although less so for shallow initial path angles where terminal velocity is reached at higher altitude.

Altitude for decelerator initiation, defined here as altitude for Mach 3, decreases with ballistic coefficient increase.

2. Initial Angle of Attack

Both a_{max} and the impact velocity are greater for larger (backward) initial angle of attack. The effect decreases to a negligible amount for shallow initial path angle.

Decelerator-initiation altitude is lower for larger angles of attack. Again the effect is unimportant for shallow initial path angle.

The initial angle of attack produces a damped pitch oscillation throughout the trajectory, causing the entry vehicle to produce less average drag force than it would under strict vehicle-path ($\alpha_E = 0$) alignment. For $\alpha_E = 0$, the body shape under consideration produces the greatest overall drag impulse.

3. Capsule Diameter

Increases in this parameter slightly increase peak acceleration and impact velocities for the steeper initial path angles.

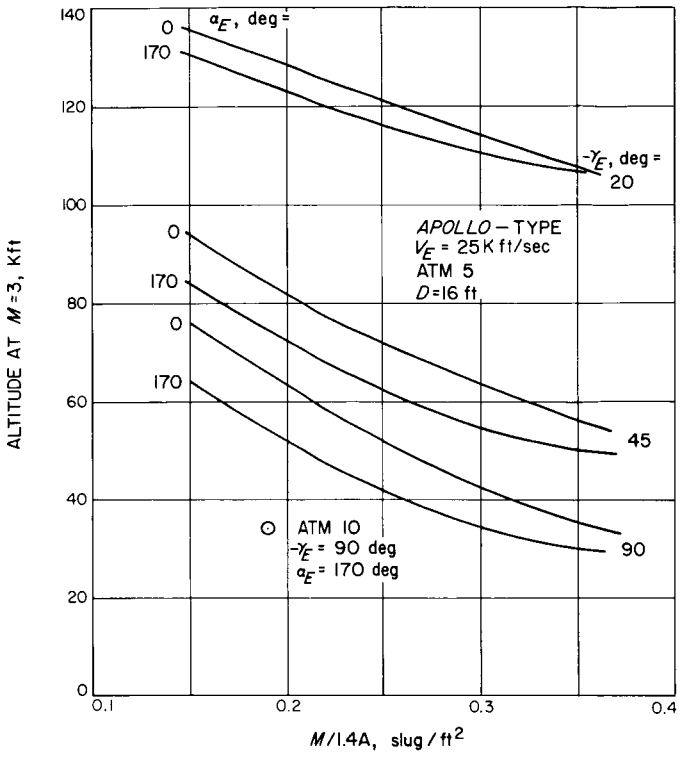

Fig. 5. Effect of capsule ballistic coefficient on trisonic altitude

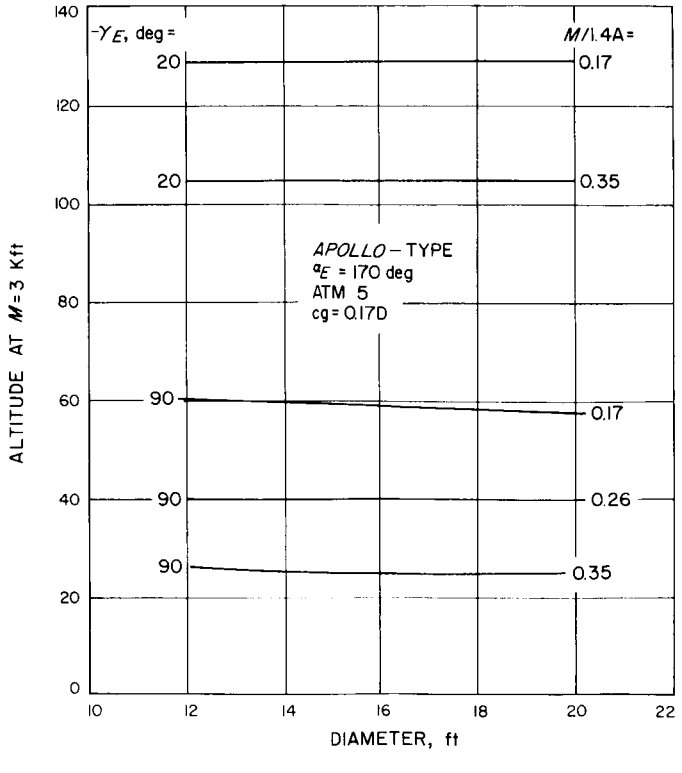

Fig. 6. Effect of capsule diameter on trisonic altitude

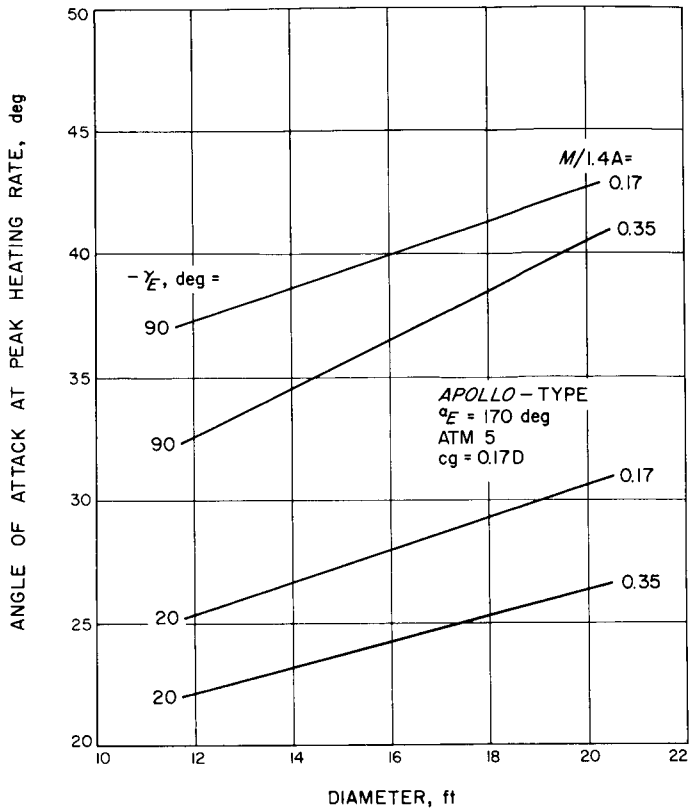

Fig. 7. Effect of capsule diameter on angle of attack at peak heating rate

Diameter has negligible effect on altitude for decelerator initiation.

Increase in diameter generally increases the angle-of-attack amplitude envelope somewhat and decreases the oscillation frequency. This is a moment of inertia effect.

All atmosphere models used assume a pressure at the surface of 14 mb. The atmosphere model 5 has the lowest density at the surface and thus the highest impact velocity to be expected if terminal velocity is approached. Atmosphere model 10, however, has the lowest pressure at all altitudes, which is the controlling factor for auxiliary decelerator deployment (terminal velocity not reached). Thus, as is shown in Fig. 5, Mach 3 occurs at a considerably lower altitude in atmosphere model 10 than in atmosphere model 5. The highest accelerations occur in atmosphere model 10. Generally speaking, peak acceleration is determined by the stratosphere density gradient parameter, scale height, and the values of this quantity (and of stratosphere temperature) are equal in models 5 and 10. However, steep entry trajectories penetrate the

higher troposphere of model 5 prior to peak acceleration, alleviating the peak acceleration loads, compared to the peak experienced in the stratosphere of model 10. The approximately 200-Earth-g peak acceleration in model 10 was the basis for maximum design load in the later design investigation of the blunt-cone lander.

IV. HEAT SHIELD DESIGN ESTIMATES

Estimates were made of the heat transfer to the stagnation point of an *Apollo*-shaped body and of the heat shield thicknesses required to sustain this heat for a number of different Mars entry conditions. Analysis methods at the stagnation point for both heating rates and heat shield thickness were quite good, but there is so little reliable or applicable data on the properties of the materials of interest that heat shield estimates can cover a wide range of thicknesses. Assumptions were made, based on these stagnation point analyses, which allowed prediction of the distribution of the heat shield around the entire body without the use of elaborate methods. This approach has a limited accuracy but was deemed sufficiently conservative for the purpose of this study.

A. Heat Transfer to the Stagnation Point of an Apollo-shaped Vehicle

1. Equations, Assumptions, and Limitations

The equations used to describe the convective and radiative heat pulses to the stagnation point of an *Apollo*-shaped body were derived with the assumption that the data and theory for Mars-type atmospheres can be fitted empirically to a density-to-a-power, velocity-to-a-power equation. The equations used were (Ref. 4):

$$\dot{q}_c = 2.91 \times 10^{-9} F \left(\frac{\rho}{R_N}\right)^{1/2} V^{3.19} \quad (\text{Btu/ft}^2\,\text{sec})$$

$$\dot{q}_r = \frac{R_N (10^5 \rho)^{1.35}}{F^2}\left[-13.9 + 0.692\left(\frac{V}{10^4}\right)^{7.53}\right] \quad (\text{Btu/ft}^2\,\text{sec})$$

These equations are reasonably accurate providing:

1. The gas in the shock layer is completely in equilibrium or the nonequilibrium portion is small in relation to the total shock thickness.
2. The gas in the shock layer is transparent to its own radiation and is isoenergetic.
3. There is no argon in the atmosphere.
4. There is catalytic recombination at the wall.
5. The shock layer is treated as an infinite slab rather than with curvature.

The last three assumptions probably do not affect the results significantly. The equilibrium-only assumption is quite good for the large bodies considered in this study, for the shock standoff distance is large. The transparency assumption most likely overestimates the radiant heating (perhaps by as much as a factor of 2), but is thought to be conservative for the purpose of these preliminary estimates.

The constant F in each of the equations is an adjustment factor to account for the fact that the fluid dynamic situation does not allow the *Apollo* shape to be treated as a sphere. Because the sonic line is on the elbow of the *Apollo* shape, the convective heating increases and the radiative heating decreases. The constant used was obtained from extensive test data from the Mercury and Gemini programs.

2. Calculated Heat Transfers

Convective and radiative heat transfer, stagnation enthalpy, and stagnation pressure were calculated for all of the trajectory runs mentioned in the earlier part of the over-all capsule study. Typical convective and radiative heat pulses for initial entry angles of -90, -45, and -20 deg are shown in Fig. 8. The relative shapes of the curves do not change much for other conditions. As shown in Table 2, the free-stream density at peak heating is very low, about 10^{-6} slugs/ft^2, and the velocity is still quite high. The peak stagnation pressure is also low and does not quite reach Earth atmospheric pressure even with ballistic coefficients as high as 0.35 slugs/ft^2. The total heat load (convective plus radiative) to the stagnation point of the body is low.

Variations in the integrated heat loads to the stagnation point of the *Apollo*-shaped body for the different trajectory input parameters are shown in Figs. 9, 10, and 11.

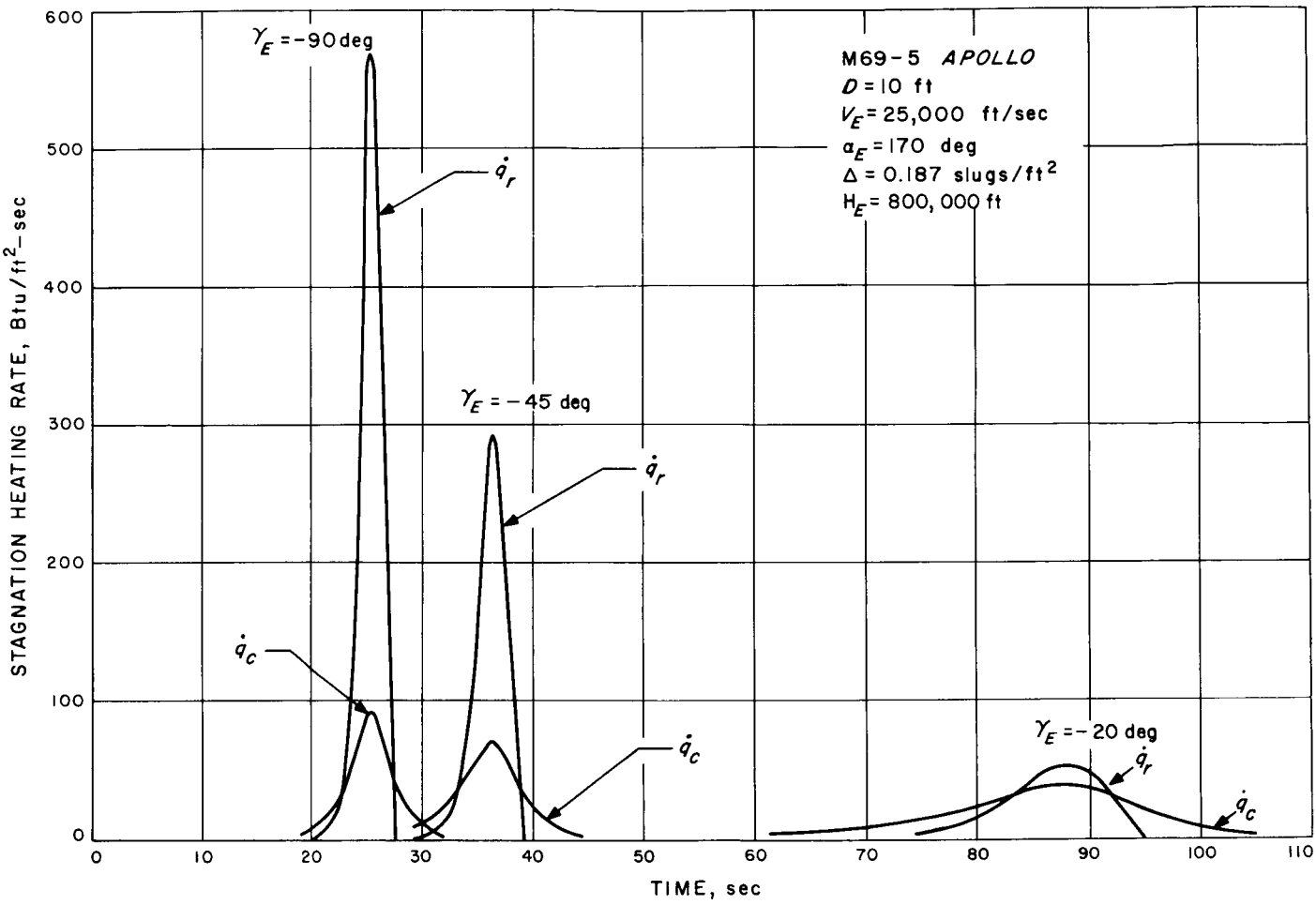

Fig. 8. Mars entry heat and pressure pulse for different entry angles

Table 2. Supplementary data for heat pulses shown in Fig. 8

	Initial entry angle,[a] γ_E, deg		
	−90	−45	−20
Density at peak heating, slugs/ft²	2.3×10^{-6}	1.8×10^{-6}	5.9×10^{-7}
Velocity at peak heating, ft/sec	22,500	21,600	21,000
Peak pressure, psi	9.51	6.78	2.43
Total integrated convective heating, Btu/ft²	510	550	830
Total integrated radiative heating, Btu/ft²	1390	980	570

[a] Initial entry altitude of 800,000 ft.

Figures 9 and 10 show the effect of ballistic coefficient, initial entry angle (γ_E), and initial angle of attack (α_E) on total heating in two different atmospheres, representing reasonable extremes in inverse scale height. As expected, total heating increased with both ballistic coefficient and initial entry angle. Higher initial angles of attack cause the vehicle to experience higher oscillating amplitudes, causing a lower effective area and effective drag coefficient for the *Apollo* shape and essentially raising the ballistic coefficient. Higher ballistic coefficients cause the vehicles to penetrate to a higher density at the same velocity, thus increasing heating. In general, the 90-deg case gave the highest total heating because of the high radiant heating predictions. The effect of initial entry velocity on total heating is shown in Fig. 11. Total heating drops off rapidly as the initial entry velocity drops from 25,000 to 21,000 ft/sec.

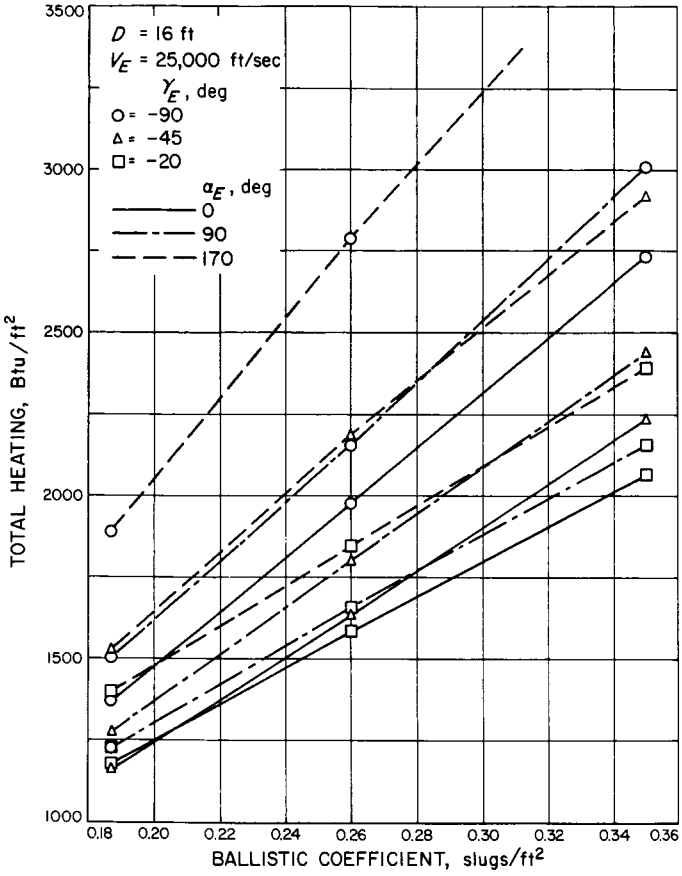

Fig. 9. Effect of ballistic coefficient on total heating at the stagnation point of an *Apollo*-shaped Mars capsule in atmosphere M69-5

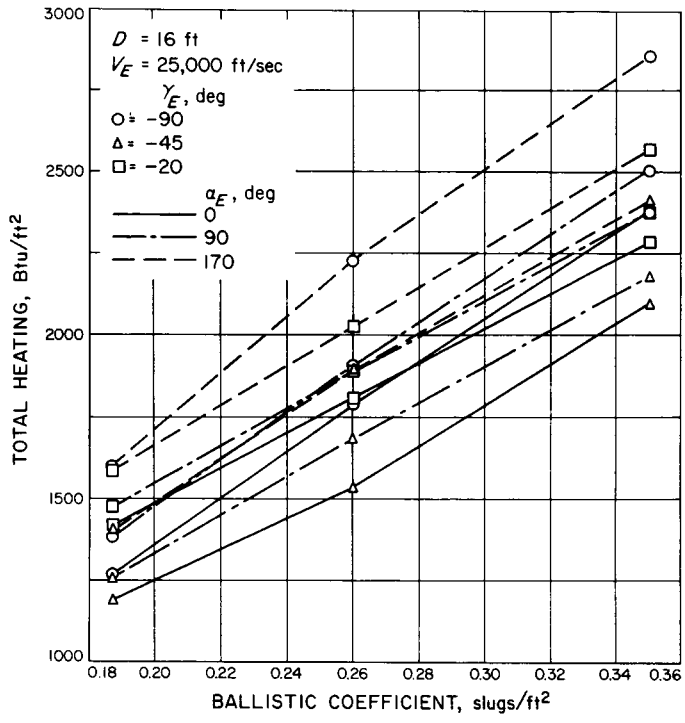

Fig. 10. Effect of ballistic coefficient on total heating at the stagnation point of an *Apollo*-shaped Mars capsule in atmosphere M69-6

B. Heat Shield Thickness Requirements at the Stagnation Point of an Apollo-Shaped Vehicle

1. Equations, Assumptions, and Limitations

The equations used in this analysis are essentially those of Swann and Pittman at Langley AFB (see Ref. 5). The specific terms and treatments used are discussed in more detail in Ref. 6. The main limitations on the technique are the assumptions that (1) all ablation or degradation processes take place at a plane surface rather than in depth, and (2) reliable data are available for all inputs required by the computer program.

For Mars entry, oxidation has been shown to be insignificant (Ref. 7). Therefore, Mars loss rates can be approximated either by Arhenius-type equations derived from thermogravimetric analysis (TGA) and plasma arc tests, or by backward solution of the boundary condition equation assuming a quadratic convective blocking term. Unfortunately, TGA data are usually wrong because of a failure to match TGA parameters with real ablation system parameters. Plasma arc tests are available in convective heating facilities but not in the convective–radiative facilities important to Martian entry. The quadratic blocking term method is also in error since it was derived for a convective-only system and provides a negative square root when radiative heating gets large (in comparison with the convective). In spite of this lack of modeling, adjustments can be made in the mass loss equations to force the prediction technique into a more conservative estimate of the actual ablation situation.

Nearly all the data used for inputs were incomplete in some way. For this reason, a limited error analysis was done using perturbation methods similar to those discussed in Ref. 6. This error analysis provided the boundaries on the heat shield weight estimates shown in a later figure. The major uncertainties used in this error analysis are shown in Table 3. Even the ablation uncertainties listed there could be seriously wrong if the actual ablation mechanism is different from that presently assumed, based on data which are not really directly applicable.

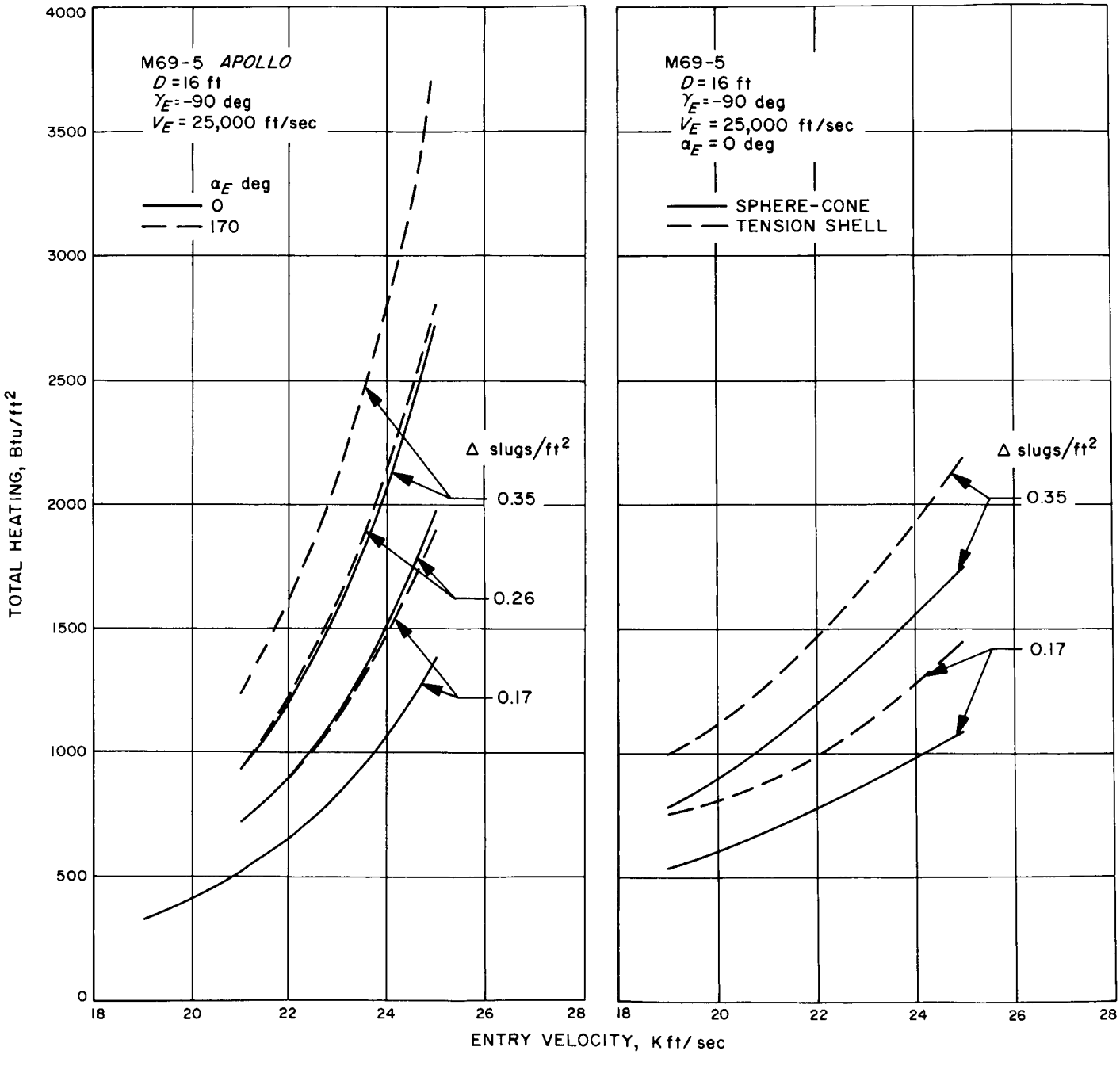

Fig. 11. Effect of entry velocity on total heating at the stagnation point of typical Mars entry capsule

Table 3. Estimated uncertainties in those parameters having the greatest effect on heat shield requirements

Parameters of greatest effect	Uncertainties, %
Thermal conductivity of char	+20/−50
Ablation rate at the outer surface	+50/−50
Ablation rate at the inner surface	+50/−50
Radiant heating	+50/−50
Convective heating	+5/−10

2. Materials

Low-density phenolic nylon was used as a nominal material. Selection of low-density phenolic nylon was based on the availability of input data for analysis, not on its over-all suitability as a Mars-entry heat-shield material. Although it is somewhat representative of a class of char-forming low-density ablation materials in an ablation and insulation sense, it is not necessarily compatible with the vacuum cold soak environment anticipated before entry heating. Nylon becomes brittle when it loses water in a vacuum, making it susceptible to cracking or shattering from micrometeorite impact or entry loading transients. Comparisons were also made using data representative of two Methylphenylsilicone elastomers (one with glass and asbestos filler, GE-1001PS, one with aluminum silicate filler, GE-1004AP) and of the *Apollo* material (AVCO 5026-39).

3. Stagnation-Point Heat Shield Calculations

Typical temperature histories for heat shield interfaces at high and low angle entry into Mars are shown in Figs. 12 and 13. The vehicle velocity history is also shown for reference. When the virgin material reaches a limiting degradation temperature it is not allowed to superheat, but is instead forced to change to a constant temperature situation. This technique is thought to give a compromise between mass loss rates derived from TGA or plasma arc tests, which are not directly applicable, and the estimated real situation. The change in mass loss rate is emphasized by the hump in the surface temperature at the transition point. A similar temperature limit

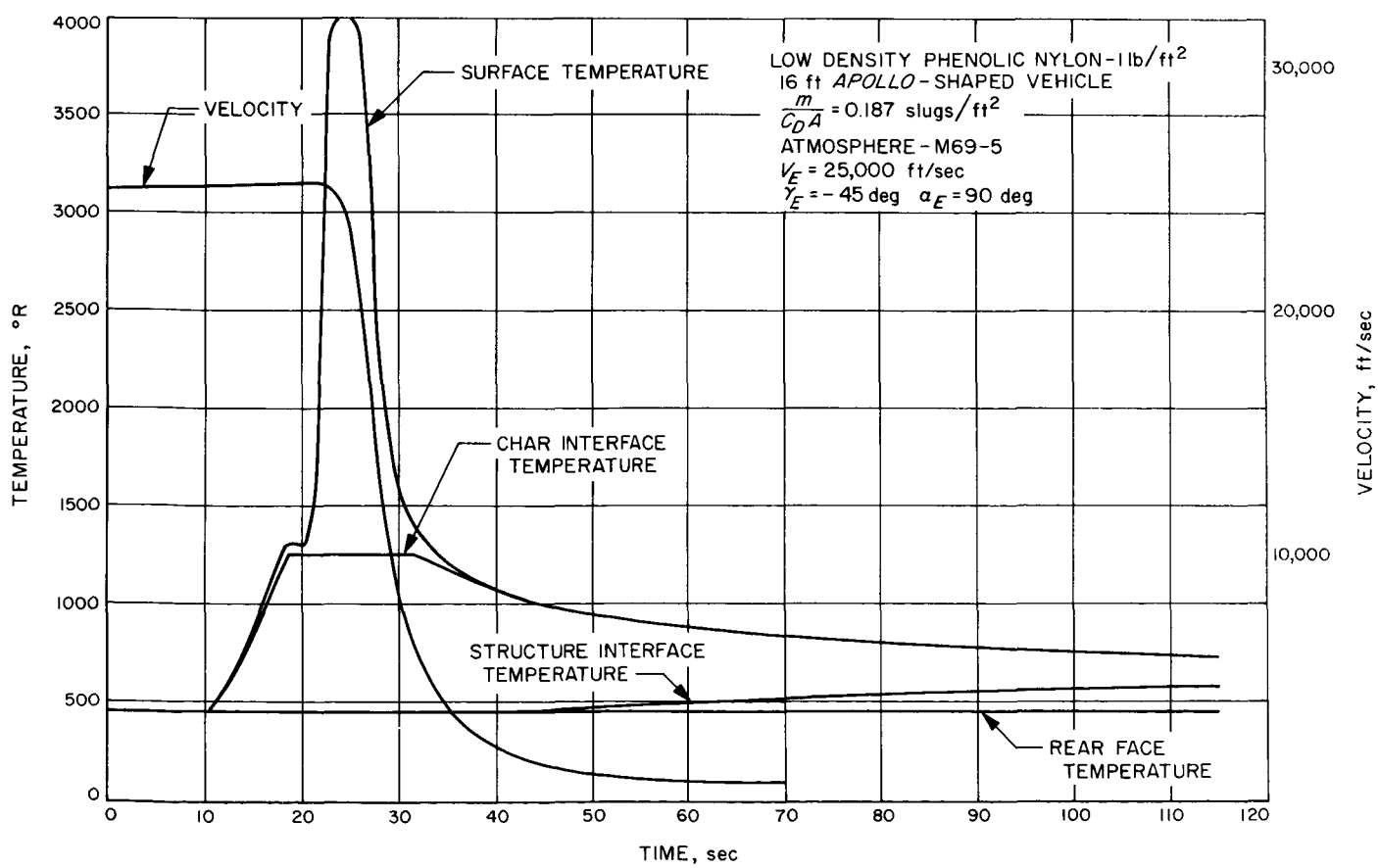

Fig. 12. Typical heat shield temperature history for high-angle Mars entry

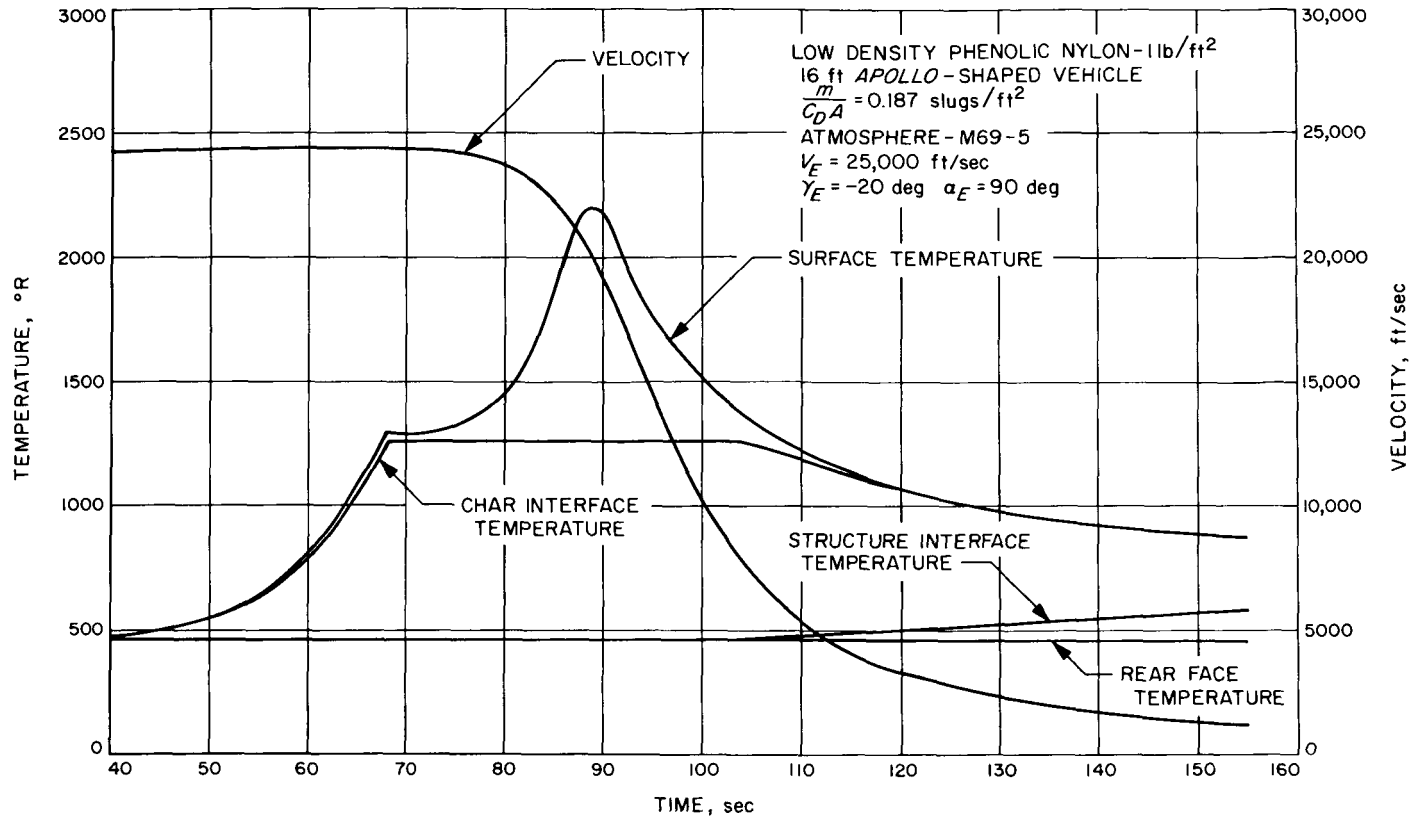

Fig. 13. Typical heat shield temperature history for low-angle Mars entry

is placed on the surface temperature since it is hard to believe that the graphite char will achieve 7000°R. It would (according to this computer program) if char mass loss rates are taken from data derived from plasma arc facilities (Ref. 8). These facilities were operated with somewhat lower level heating rates than those predicted in this study for the −90-deg entry case.

The effects of initial entry angle on the heat shield weight requirements using the inputs for several different materials are shown in Fig. 14. The weights shown there and in the next two figures are those required to hold the temperature rise at the structure–heat shield interface to 100 deg at the time of deployment of the Mach 3 parachute. The implications of other temperature rise limits at other times is shown in a later figure. In spite of the fact that the −90 deg case provides the greatest integrated heat flux, it is the −20 deg case, where the heat is provided over a long period of time, which actually requires the greatest weight of material to hold the structure temperature down. The shaded region encompasses the probable uncertainty in the nominal low-density phenolic nylon estimates (circles) based on the variations listed in Table 3. The silicone elastomer materials give a slightly higher nominal estimate which is probably real although not outside the bounds on the low-density phenolic nylon data. The higher upswing on the 90-deg entry data for the elastomer is due to a less efficient treatment of the radiant portion of the heat input. Boundaries on the elastomer data would be approximately the same magnitude about the nominal calculations as that shown for the low-density phenolic nylon. The phenolic microballoon–epoxy–glass fiber material appears to lower the heat shield requirement. This appearance is misleading, however, for only room temperature thermal conductivities were available for this study, and the same apparent approvement can be shown for the phenolic nylon material if only room temperature properties are used. Hence, the scatter band on the epoxy material would be much higher on the top and lower on the bottom than that estimated for the phenolic nylon.

The effects of ballistic coefficient on heat shield weight estimates are shown in Fig. 15. The curves are surprisingly flat in this region considering the variations in total heat fluxes shown in Fig. 9. This flatness is caused by the fact that insulation and not ablation is dominant.

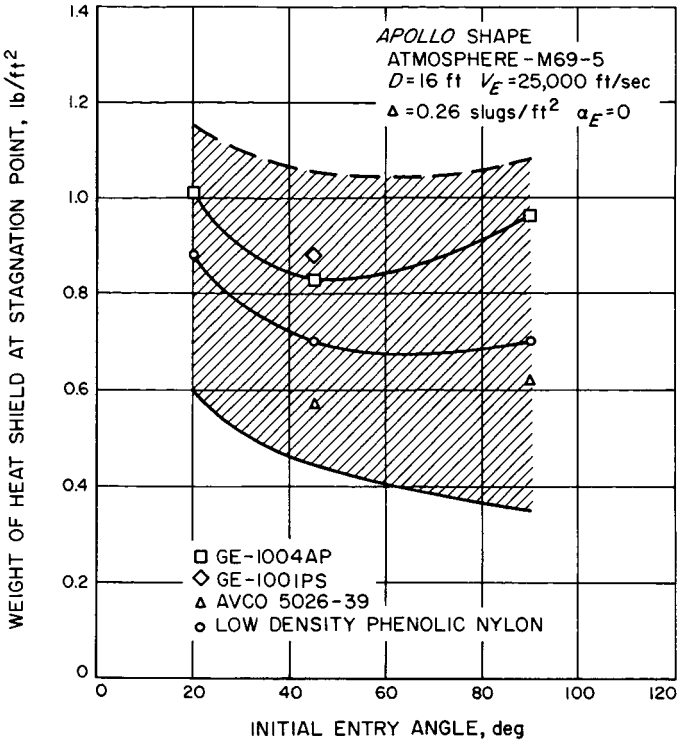

Fig. 14. Effect of initial entry angle on the estimated weight of various heat shield materials at the stagnation point

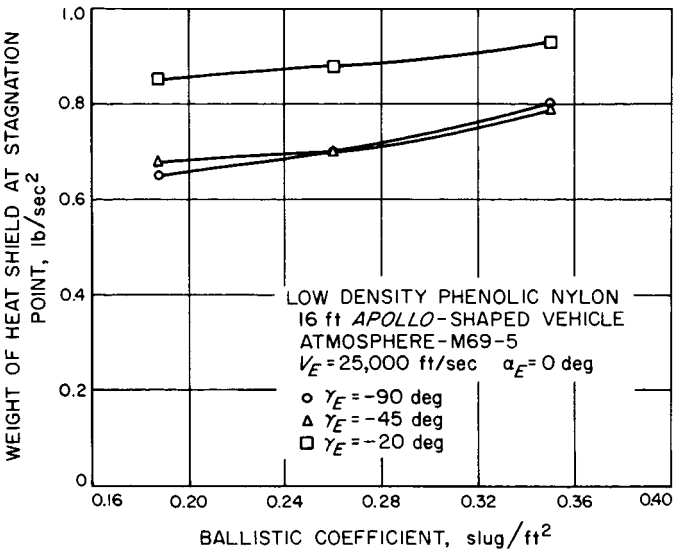

Fig. 15. Effect of ballistic coefficient on the estimate of heat shield weights at the stagnation point

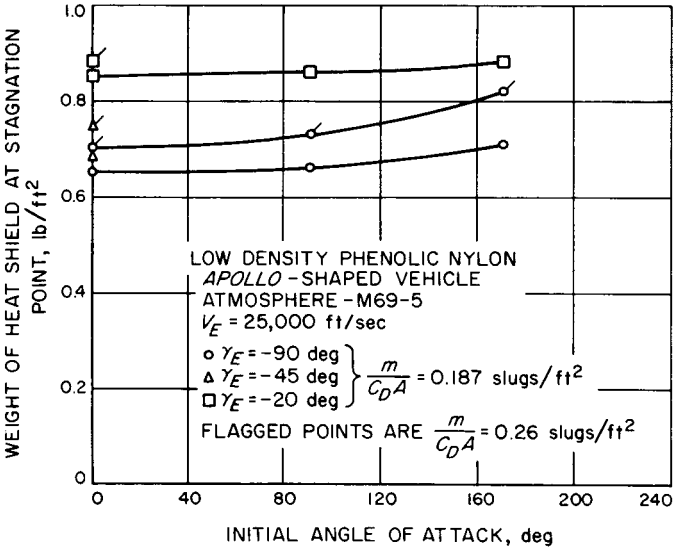

Fig. 16. Effect of initial angle of attack at entry on the estimate of heat shield weights at the stagnation point

Therefore, since the time of duration of the heat pulse is about the same for the same initial entry angle, then the insulation material requirement is essentially constant and the small differences can be attributed to differences in the material requirements to account for ablation.

Figure 16 shows the effect of initial angle of attack at entry on the heat shield weight requirements. The oscillating vehicle will have a lower effective drag coefficient, giving it a higher effective ballistic coefficient and, hence, causing greater heating for the same trajectory. The forebody heat shield penalties shown in this figure are not too bad, but the oscillations cause much more severe variations on the aft cone. In certain instances of the cases studied, the aft cone heat shield weights increased by as much as a factor of two because of the oscillations of backward entry. A 90-deg initial angle of attack damps sufficiently by the time it reaches peak heating that its effect on the aft cone is not particularly significant.

The effect of vehicle diameter is shown in Fig. 17. The maximum variation in heat shield requirements between diameters of 9 to 19 ft is only 10% because of tradeoffs in the convective and radiative heat inputs. Based on these calculations, the minimum weight per unit area appears to be at a vehicle diameter of about 14 ft.

Some gain appears to be possible by lowering the initial entry velocity. Dropping this velocity from 25,000 to 23,000 ft/sec reduces the heat shield requirement at the stagnation point between 10 and 15% (Fig. 18). Comparative curves for different structure–heat shield temperature rises and for different parachute deployment

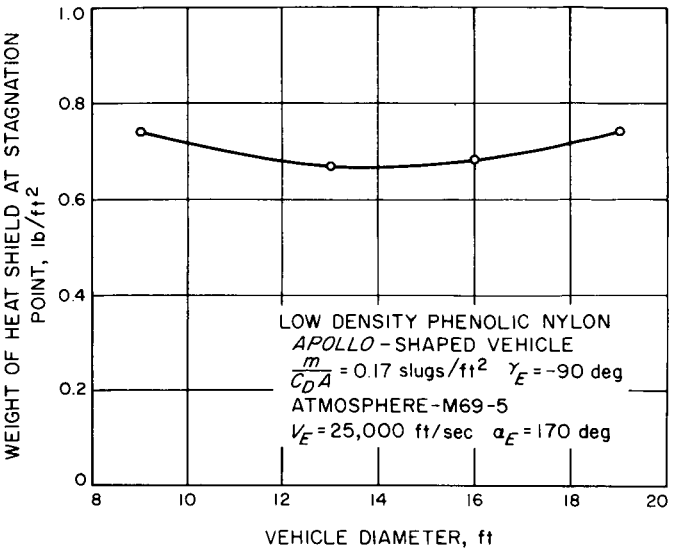

Fig. 17. Effect of vehicle diameter on the estimate of heat shield weights at the stagnation point

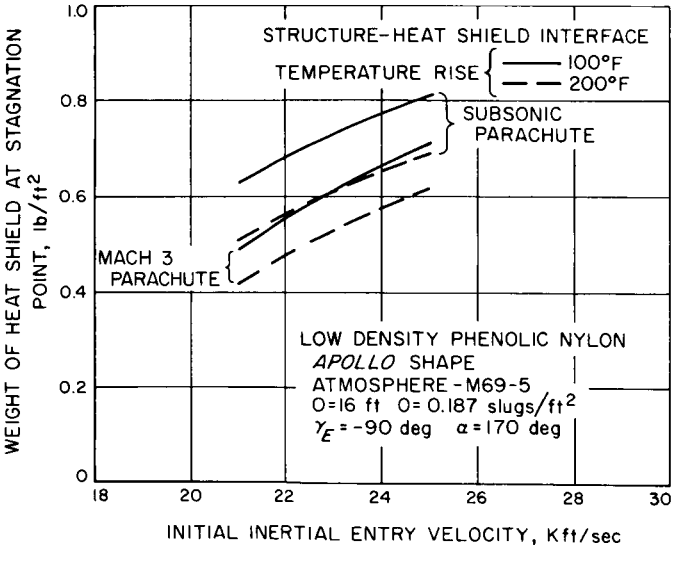

Fig. 18. Effect of initial entry velocity on the estimate of heat shield weights at the stagnation point

times are also shown. Changing the allowable temperature rise at the structure–heat shield interface from 100 to 200°F decreases the weight of heat shield required by about 15% for the Mach 3 parachute deployment and by about 20% for the subsonic parachute deployment. Similarly, changing from the Mach-3 deployment mode to a subsonic-deployment-only mode increases the weight requirement by 20% if a 100°F temperature rise is designated, and by 15% if a 200°F temperature rise is designated. A more complete analysis would trade off the allowable structure–heatshield interface temperature and the stagnation pressure-time relationship to minimize the combined structure–heat shield weight.

C. Heat Shield Weight Distribution Around Apollo-Shaped Vehicle

1. Assumptions and Limitations

Flight tests into Earth have indicated that ablation is essentially the same over the entire front surface of an *Apollo*-shaped (Mercury) entry vehicle for most low-entry-angle trajectories. Such results are probably caused by a combination of effects (oscillation, oxidation, etc.) which tend to equalize the total heating over the entire spherical portion of the forebody. Although Mars entry will be somewhat different, a certain amount of oscillation through peak heating is predicted for the *Apollo*-type shape. Hence, for the purpose of this report we will assume a constant weight per unit area over the entire spherical forebody.

Experimental measurements of the heating in the elbow regions have shown a significant increase in heating rate for many conditions. This, plus the increases indicated by the predicted oscillations, makes it necessary to use some factor to increase weight required around the elbow. A factor of 1.25 has been chosen for the purposes of this study. It increases the total heat shield weight of the vehicle by about 3%.

The aft cone weights are calculated assuming that the aft cone sees approximately 2½% of the convective heating (Ref. 9) and 3½% of the radiative heating (Ref. 10) at the stagnation point. Although these estimates are for non-ablating bodies, it is not felt that, in this situation, the ablation products contribute significantly to aft cone heating. Exact heating distributions along the cone are not well known, so these numbers have been assumed for the entire aft cone surface.

2. Total Heat Shield Weight Calculations

Average heat shield weights per unit area can be derived from the stagnation point calculations plus the assumptions just listed. Such weights are listed in Table 4 for a 16-ft body entering at 25,000 ft/sec at 0 angle of attack. Both phenolic nylon and silicone elastomer are listed for the forebody and the elbow regions, but only the silicone elastomer is listed for the aft cone, where RF transparency is necessary. For entry velocities less than 25,000 ft/sec, these listed numbers decrease by approximately 15% for each 2000-ft/sec decrease in

velocity. For a 90-deg initial angle of attack, the listed numbers increase by 5%; for 170-deg initial angle of attack they increase 15%. For the 170-deg initial angle of attack, the aft body weights should also be increased by some additional factor to account for oscillation at peak heating. This factor has not yet been determined for 45- or 90-deg initial entry angles. For a 20-deg entry angle, it does not appear to be significant. These per-unit-area numbers are about the same for 13-ft vehicles but increase about 10% for 9- or 19-ft vehicles. The forebody numbers given in Table 4 are acceptable for both

Table 4. Average heat shield weight estimate over the spherical forebody, the elbow, and the aft cone of an *Apollo*-shaped vehicle

(Assuming: 16-ft vehicle; 25,000 ft/sec entry velocity; 0 deg initial angle of attack; less than 100°F temperature rise at structure when stagnation pressure is greater than 0.1 atm, or less than 200°F rise at subsonic chute deployment)

Initial entry angle, deg	Ballistic coefficient, slugs/ft²	Average weights per unit area, lb/ft²				
		Phenolic nylon		Silicone elastomer		
		fore-body	elbow	aft cone	fore-body	elbow
−20	0.187	1.07	1.34	0.38	1.22	1.53
−45		0.98	1.23	0.34	1.13	1.41
−90		0.98	1.23	0.38	1.23	1.54
−20	0.26	1.10	1.38	0.41	1.23	1.54
−45		1.00	1.25	0.36	1.13	1.41
−90		1.03	1.29	0.41	1.29	1.61
−20	0.35	1.15	1.44	0.45	1.28	1.60
−45		1.10	1.38	0.40	1.23	1.54
−90		1.15	1.44	0.46	1.42	1.68

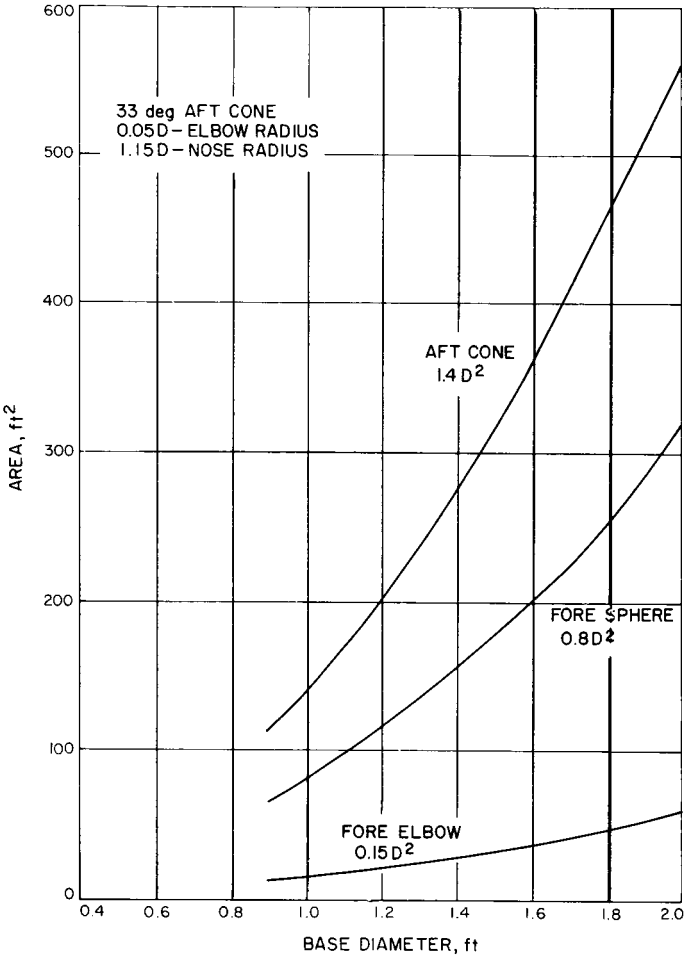

Fig. 19. Gross area relationships for *Apollo* shape

a 100-deg temperature rise at a Mach 3 parachute deployment and a 200-deg temperature rise at subsonic parachute deployment. There should be a 15% increase if a 100-deg temperature rise at subsonic deployment is desired and a 15% decrease if a 200-deg temperature rise at Mach 3 deployment is allowed. The aft cone numbers in Table 4 are chosen from stagnation pressure–time considerations and do not change with different allowable structural interface temperatures for the forebody. Now, using Table 4, the percentage increases and decreases just mentioned for other conditions, and the gross area relationships for an *Apollo*-shape shown in Fig. 19, the total weight of heat shield can be calculated for any body.

As an example, consider a worst-case entry for a typical entry body under study for Mars entry. Assume a low-angle (20 deg), backward entry at 25,000 ft/sec into the M69-5 atmosphere (see Table 1 and Ref. 3), a 16-ft vehicle with a ballistic coefficient of 0.24 slugs/ft², and a 200-deg allowable temperature rise at the structure–heat shield interface at subsonic parachute deployment. The data in Table 4 can be interpolated to give 1.09 for the phenolic nylon forebody, 1.37 for the phenolic nylon elbow, and 0.40 for the silicone elastomer aft cone. This is multiplied by 1.15 to account for backward entry and then multiplied by the areas read off Fig. 12 to give 250 lb for the fore sphere, 48 lb for the elbow, and 142 lb for the aft cone. This total heat shield weight of 440 lb is 20% of the total weight of the vehicle.

The severe entry case calculated above is shown in Fig. 20 for different vehicle diameters. Also shown are the results for a more nominal case of a low-angle (20 deg) zero-angle-of-attack entry at 23,000 ft/sec into the M69-5 atmosphere, a vehicle with a 0.24 slugs/ft² ballistic coefficient, and an allowable temperature rise at the structure–heat shield interface at Mach 3 parachute deployment of 200°F. The high heat shield fractions observed in the severe entry case can be lessened

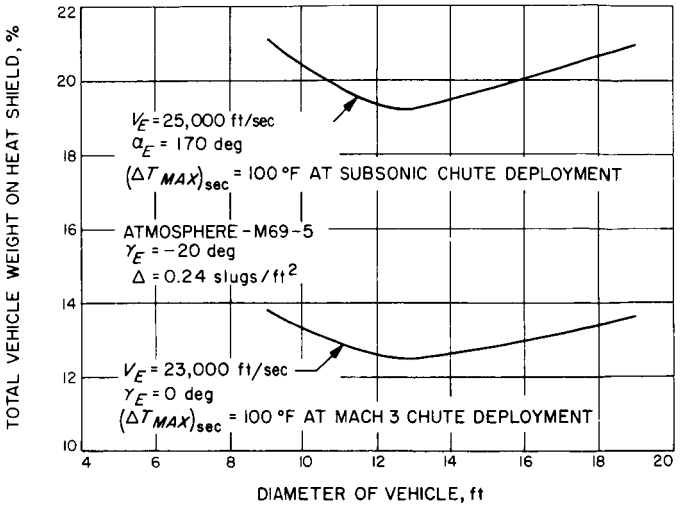

Fig. 20. Approximate effect of body size on heat shield weight requirements

through improved heat shield materials or possibly by improved understanding and definition of the heat shield materials now available. Arbitrary limiting structural-interface temperatures at different chute deployment times can be replaced with interface temperature–stagnation-pressure tradeoffs as better data on the equilibrium conditions during transit and on body size, shape, and orientation become available.

D. Conclusions and Recommendations

A method of obtaining heat shield weight estimates has been outlined. Because of a lack of reliable input data on the heat shield materials investigated and the assumptions used in this study to distribute the heat shield over the entire body, the method outlined is considered only approximate. Where a choice was necessary at any point in the development, the conservative choice was taken. Even so, the results form reasonably realistic upper limits for any set of trajectory parameters and may be used as such with some confidence during initial planning.

The only trajectory parameter unaccounted for is the large vehicle oscillations through peak heating with both high initial entry angles and backward entry. For this one condition and with lunar motion,[1] the aft cone heating will increase by a factor of 3 or 4 and with it the aft cone heat shield weight. Such a condition could double the heat shield weight and shift the vehicle center of gravity back into or toward the aft cone section. This condition is untenable and the design must preclude the occurrence of this capsule condition.

There are several tradeoffs which decrease the heat shield weight requirements. Lowering the entry velocity decreases the heat shield weight by about 15% for each 2000 ft/sec step down from the nominal of 25,000 ft/sec. Holding the initial entry angle of attack to less than 90 deg influences the forebody weight by about 10% and prevents the possibility of the untenable (on the aft body) lunar motion condition. Eliminating the requirement for rf transparency on the fore body also decreases the heat shield weight, for more efficient ablators and insulators may then be used. Probably the most important tradeoff is that concerning the allowable temperature rise at the structure–heat shield interface. This rise is a function of stagnation pressure and time and should be investigated in more detail in future studies. The improvements possible through tradeoffs of this type are shown in Fig. 20.

[1]Oscillation and spin coincide, and the same edge of the vehicle faces forward at all times.

V. ENTRY CAPSULE STRUCTURE

The aerodynamic shape of the entry body defines the external surface of the capsule structure. The structure must maintain its integrity when subjected to the loads imposed during entry. These loads result from the external pressure distribution and its inertial reaction.

Initial guidelines require that the capsule structure be rf transparent. Therefore, the bulk of the analysis has been done on a fiberglass shell of sandwich construction. An aluminum sandwich shell comparable to the fiberglass shell selected for the configuration study was analyzed to evaluate its structural weight.

Sandwich construction was selected for the shell structure for the following reasons:

1. The high radius of gyration of a sandwich structure results in an efficient structure for shells subjected to loadings resulting in compressive stresses.

2. The bending moments, such as those occurring at concentrated loads, are efficiently resisted by a sandwich structure.

3. The little-understood areas of flutter and acoustic loading should be less critical for sandwich structures than for ring-stiffened structures with the same effective stiffness.

4. Sandwich monocoque construction presents a clean inside surface to any portion of the capsule which is being separated.

5. In areas where a clean inside surface is not required, small objects may be mounted directly to a sandwich shell which might require local stiffening if a frame-skin structure were used.

The sandwich construction has the disadvantage of a relatively large weight allocation for connections (bond weight). Ring-stiffened sandwich construction pays the penalty of bond weight without receiving all the advantages which are obtained by applying the ring weight to monocoque sandwich construction.

Honeycomb cores have been assumed because they are readily available and provide the near continuous support required by the thin surface skins of the sandwich.

The structural study was made for an *Apollo*-type shape, as was stated in the guidelines (Section I). On the basis of a previous study, a payload attachment diameter of 0.45 times the maximum diameter was assumed. This diameter is somewhat smaller than the diameter which optimizes aeroshell weight and represents a compromise between a reasonable internal payload support configuration and reasonable shell weights and deflections.

The shell analysis was done, in a large part, using a linear axis-symmetric, thin-shell-analysis computer program. The shell was idealized as a thin shell whose middle surface conformed to the *Apollo* shape. Final design should modify the shell middle surface to account for the shell thickness. The radius of curvature at the knuckle transition from forward structure to aft cone is not large compared to the shell thickness, and an error is introduced in the thin shell solution. This error can be treated as an error in describing the middle surface since the force-displacement relationships can be closely matched by assuming the "middle" surface follows the resultant force trajectory for a thick shell with constant membrane strain.

The critical entry loading on the shell is due to the external pressure and its inertial reaction at maximum dynamic pressure. Based on preliminary analysis, boost loads have been assumed not critical. The axis-symmetric loading condition has been assumed more critical than the combined loading condition at maximum angle of attack. This assumption was made out of necessity, but has been checked for one *Apollo*-shaped capsule and found to be satisfactory. The pressure distribution is an analytic approximation of the wind tunnel data, and the amplitude is chosen such that the resultant has the required value to balance the inertial load obtained from the entry trajectory analysis.

No thermal stresses have been added to mechanical stresses, but the design philosophy definitely considers thermal loading. A monocoque shell rather than a doubly connected structure (i.e., shell and internal struts) is used largely to prevent high stresses due to differential expansion caused by thermal gradients.

The analysis of the aft cone for buckling was performed by finding the combination of external pressure and axial load that approximately matched the membrane stress resultants found in the bending analysis. A linear

interaction formula was used based on a paper[2] in Ref. 11. An equivalent cylinder buckling coefficient based on experiment was taken from the same paper (0.3 was used). The effect of nonuniform external pressure was treated as shown in a second paper[3] from Ref. 11.

The value used for the yield stress of fiberglass represents what is thought to be a lower bound on the mean yield strength in any direction of a surface made of at least three laminates properly oriented.

The dynamic characteristics of the capsule have not been the subject of detailed analysis. The case of a 16-ft *Apollo*-shaped capsule and sterilization canister attached along a ring with a diameter 0.45 times the capsule diameter has been looked at. The first lateral or "nodding" mode appears to have a frequency of 5 cps; the first longitudinal or "bobbing" mode appears to have a frequency of 14 cps. Both of these modes would result in extremely large loads at the capsule–bus interface if the capsule were to be subjected to a typical spacecraft sinusoidal vibration test. A capsule support configuration which includes provision for large damping may be required to keep these loads within acceptable limits. The frequencies for both these modes in the free entry configuration should be two to three times the boost configuration values, which places them well above the less than 3-cps aerodynamic oscillation frequencies calculated in the trajectory analysis.

The parametric study of the structural shell consisted of analyses of designs fabricated from fiberglass sandwich for 13 combinations of maximum accelerations: (a), effective loading L_E, capsule diameter D, and aft cone uniformly distributed superimposed weights w_{AD} (Table 5). Trial structural configurations were chosen and preliminary analyses performed until a configuration based on the analysis agreed with the configuration used within 10%. Since scaling of material gages for a particular design over such small variations is well understood even with crude scaling, further iterations are not required (see Table 5).

Scaling laws for structural weight as a function of the significant variables were developed based on these 13 designs. Simple scaling laws could not be developed to perfectly fit the 13 designs, so the scaling is best in the neighborhood of the design used as a base. For this

[2]Seide, P., "A Survey of Buckling Theory and Experiment for Circular Conical Shells of Constant Thickness."

[3]Bijlaard, P. P., "Buckling of Conical Shells Under External Pressure."

Table 5. Summary of design cases

D, ft	a, g	L_E, lb/ft²	w_{AD}, lb/ft²	W_{FS}, lb	W_{AS}, lb
20	216	7.72	0.25	892	372
20	216	5.71	0.25	765	373
20	216	23.82	0.25	2050	403
20	54	23.82	0.25	1050	260
20	54	5.71	0.25	396	260
10	54	5.71	0.25	60	65
10	54	23.82	0.25	135	78
10	216	23.82	0.25	337	79
10	216	5.71	0.25	108	65
10	216	11.74	0.5	190	67
20	216	11.74	0.5	1170	419
20	54	11.74	0.5	622	290
20	216	11.74	0.125	1240	343

reason, the curves given in this report are based on a capsule with an effective loading L_E of 7.72 lb/ft² (corresponds to $M/1.25A_p = 0.2$ if $w_{FD} = 0.25$), a diameter D of 20 ft, a maximum acceleration a of 216 g, and an aft cone uniformly distributed superimposed weight w_{AD} of 0.25 lb/ft², which is in the neighborhood of prime interest.

The aft cone weight depends only on the diameter of the capsule D, the maximum acceleration a, and the uniformly distributed superimposed weight w_{AD}.

If not limited by material minimum gage or yield stress,

$$W_{AS} \propto (w_{AD} + 0.16)^{0.24} a^{0.26} D^{2.64}$$

where 0.16 represents the constant bond unit weight.

The forward structure weight depends on the diameter of the capsule D, the maximum acceleration a, and the effective loading L_E which is defined as total capsule weight less front heat shield weight (including knuckle, i.e., forebody–afterbody transition section), all divided by the projected area of the capsule, and to a small extent on the uniformly distributed weight on the aft cone w_{AD}.

$$W_{FS} \propto D^{2.71} L_E^{0.70} a^{0.48} (w_{AD}) + 0.16)^{-0.07}$$

Notice that the forward structure weight is reduced by the ring load at the forward structure–aft cone interface (reduction indicated by the negative exponent of $w_{AD} + 0.16$, which results in a lowering of the ring load at the residual weight for the same effective loading L_E. It is just this effect that causes the forward structure weight to be dependent on the total capsule weight less front heat shield weight instead of total weight less 0.83 of the front heat shield, where 0.83 is the ratio of

projected area to developed area of the front surface including knuckle. This means that so long as the heat shield material is ablated uniformly over the surface, the effective loading is independent of the amount ablated by the time of maximum loading.

The analyses were based on the following assumptions:

1. *Apollo* shape
2. Fiberglass sandwich structure
3. Continuous shell
4. The critical buckling stress and "isotropic" yield stress of the material (20,000 psi) were not to be exceeded for 1.25 times limit load. An exception is that the combined bending and membrane stress at the payload attachment is not to exceed yield stress for 1.0 times limit load. This assumption allows the use of a constant value of E in buckling calculations.
5. All stresses were calculated on material thickness 13% below nominal gage and all weights and induced loads were calculated on material thickness 13% above nominal gage to allow for tolerances.
6. A 10% allowance was made for splices and construction joints. No weight allowance has been made for separation joints. Such weight must be accounted for in the residual weight.
7. An allowance of 0.16 lb/ft for bond on both surfaces was made. This figure may be high for low-temperature bonds.
8. The payload is supported by the front cap as a ring load having a diameter 0.45 that of the capsule.
9. The minimum gage used for the aft cone surface sheets is 0.006 at the base and 0.004 at the tip, which represents an extension of the current state-of-the-art.
10. Asymmetric loading is less critical than axisymmetric (which is believed to be valid for the *Apollo* shape). Analytical capability for solving the asymmetric loading problem is being acquired.
11. Room-temperature properties are applicable.

Residual weight W_R is defined as the total capsule weight less front and aft distributed weights and structure weights. Figures 21 through 29 plot W_R vs capsule

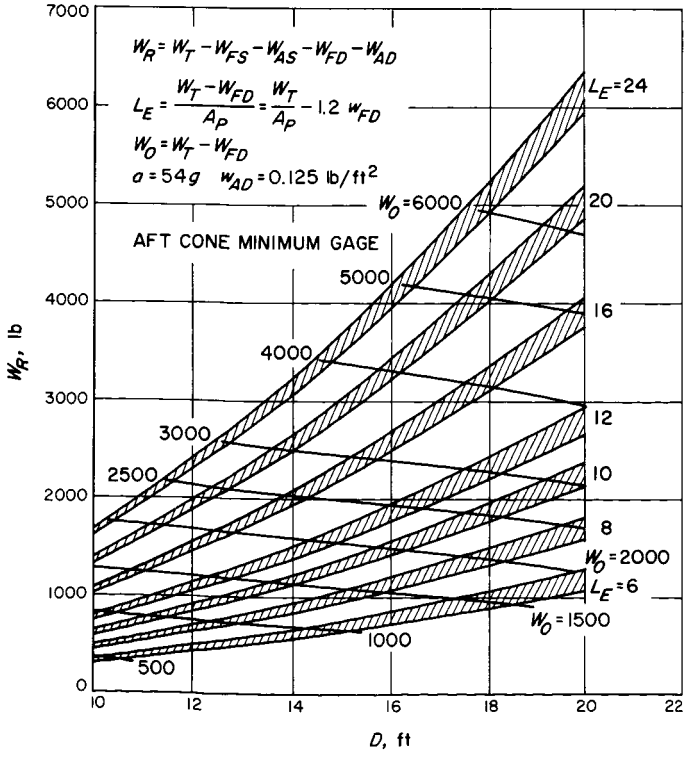

Fig. 21. Design chart for residual weight (1)

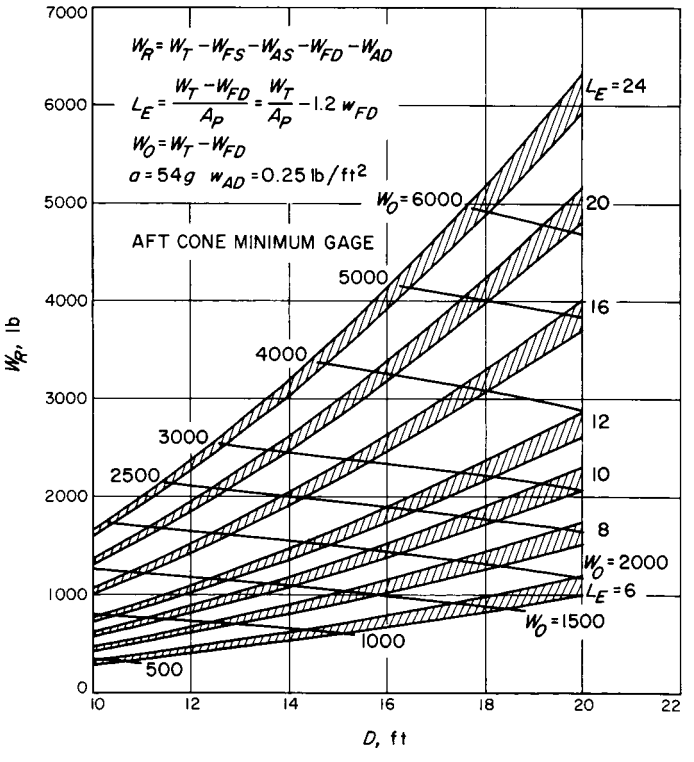

Fig. 22. Design chart for residual weight (2)

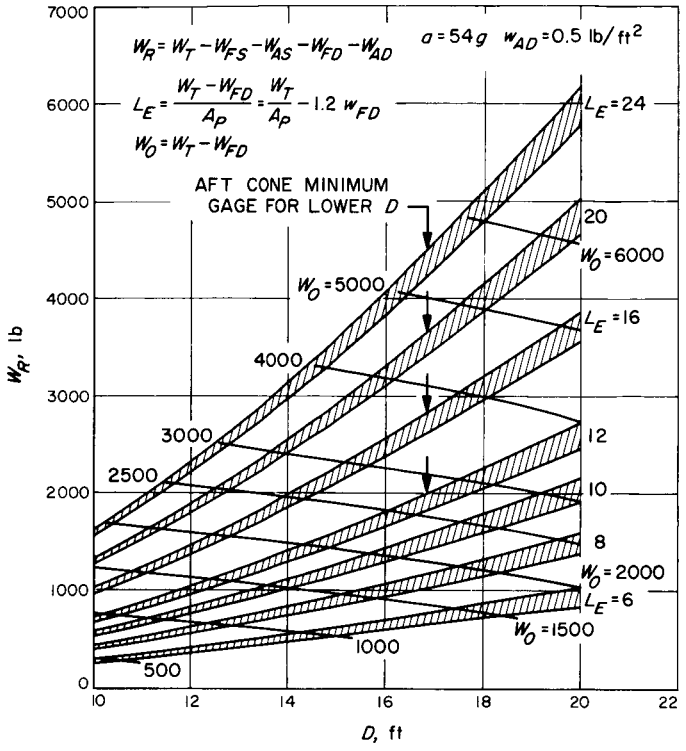

Fig. 23. Design chart for residual weight (3)

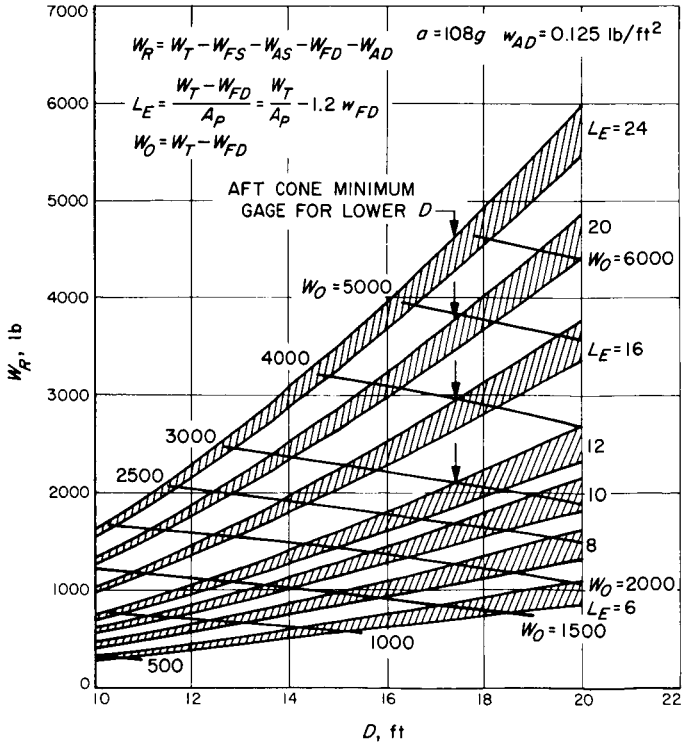

Fig. 24. Design chart for residual weight (4)

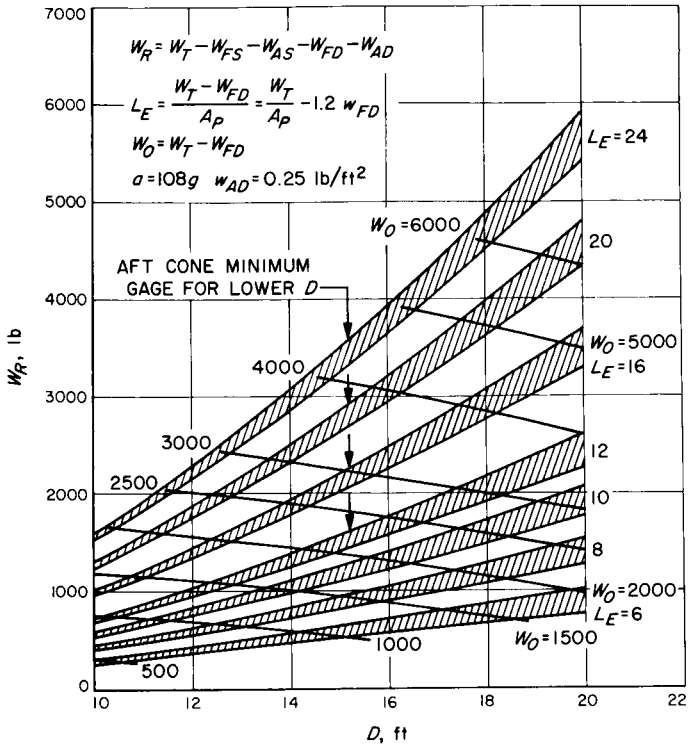

Fig. 25. Design chart for residual weight (5)

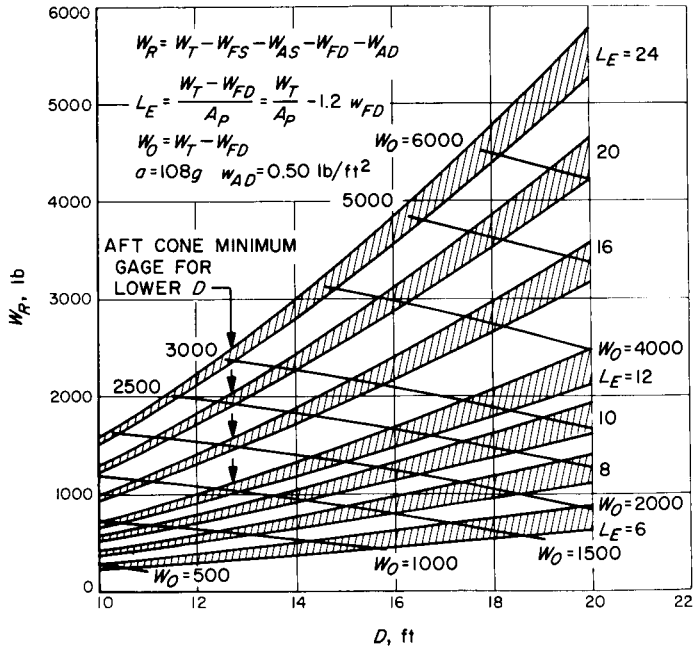

Fig. 26. Design chart for residual weight (6)

diameter D. (Figure 30 is a conversion chart for obtaining L_E.) The plots show a band with limits obtained by applying a plus and minus 15% factor to the total structural weight calculated using the developed scaling laws.

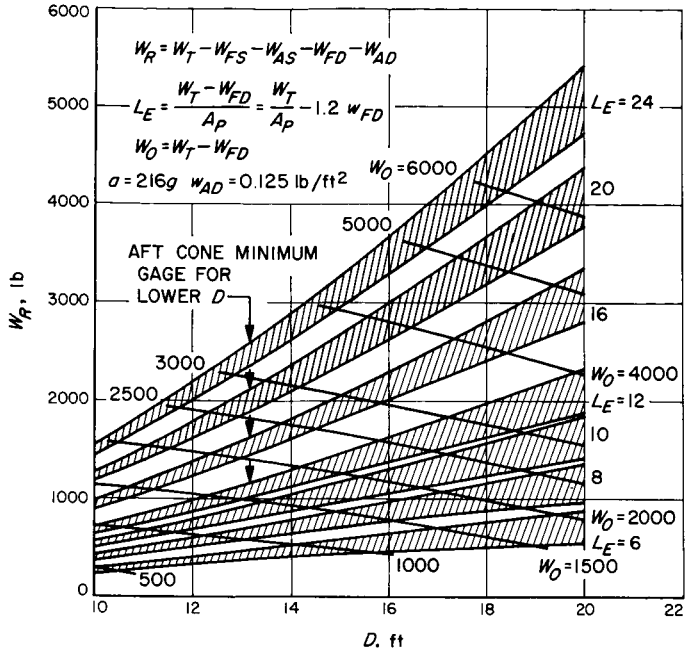

Fig. 27. Design chart for residual weight (7)

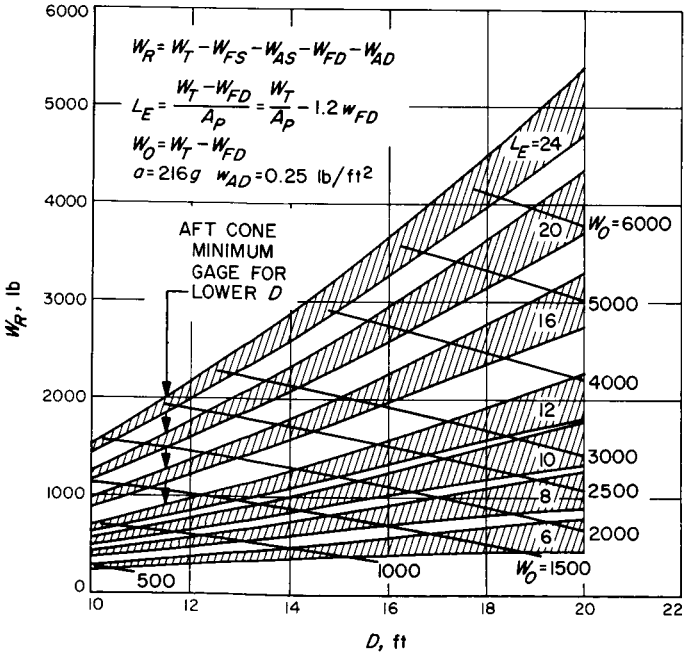

Fig. 28. Design chart for residual weight (8)

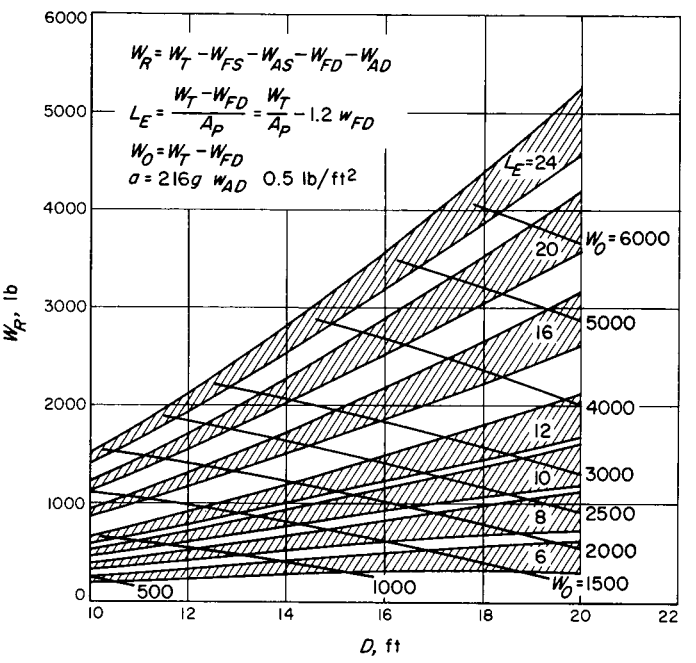

Fig. 29. Design chart for residual weight (9)

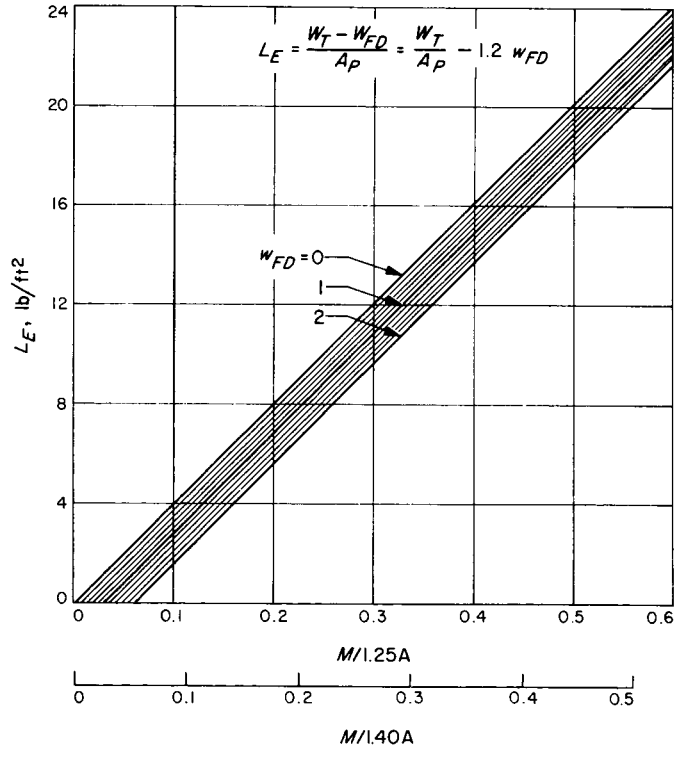

Fig. 30. Conversion chart

This band represents the uncertainty which is assumed in the results. Also plotted on these figures are lines of constant total weight less front heat shield weight W_0, which represents a nearly constant total weight. These lines are associated with the central points of the bands. For the same diameter and effective loading L_E, the other points in the band have the same W_0. As just discussed, the bandwidth shown on the graphs is not related to the tolerance allowance but is an indication of the uncertainty of the weight estimates. The lower

limits of the bands should be used unless the results of an extensive fabrication and static test program indicate that a change should be made. The actual construction of test capsules under the same tight tolerance specifications as for flight capsules, followed by a complete assay of the as-fabricated weights, from a statistically significant set of samples and a comparison of total capsule weight with the weight calculated from these samples, will allow evaluation of tolerance limits on weights and give a higher degree of confidence in the weight estimates. To make maximum use of such a test capsule it should be subjected to extensive structural testing prior to removal of the samples. The testing will increase the confidence in the structural adequacy of the shell. Even if it should be found necessary to modify the shell, the upper bound of shell weight might not increase because of the lower uncertainty of the weight estimate resulting from testing. It is the possibility of such an increase in structural weight that required the wide band in the first place.

The acceleration to be used in entering the curves should be the maximum instantaneous acceleration during entry. If the acceleration is obtained from a point mass trajectory using an effective drag coefficient to account for variations in angle of attack, the maximum instantaneous acceleration is approximately the peak acceleration times the ratio of 0-angle-of-attack drag coefficient to effective drag coefficient. The superimposed, uniformly distributed loads used should be those that are applied at the time of maximum loading. For nonuniform axis-symmetric loading, the actual distributed loading averaged over the surface under consideration may be used as a first approximation. As has been mentioned earlier, the structural weight is independent of total weight minus the uniformly distributed weight on the front surface.

Toward the end of the study it became desirable to see the effect of using an aluminum sandwich shell, and these results are presented in Table 6 for 10-ft-diameter, *Apollo*-shaped shells with 0.25 lb/ft² distributed weight on the aft cone. The weight changes basically reflect the change in tolerance allowances in changing from fiberglass to metal sandwich construction. It is adequate to apply the same percent reduction factors to the shell weights for a 16-ft-diameter capsule.

Table 6. Weight savings effected by use of aluminum sandwich instead of fiberglass sandwich for capsule shell construction

L_R, lb/ft²	a, earth g	Total shell weight, lb		Percent reduction
		Fiberglass	Aluminum	
5.71	54	144	126	12
5.71	216	210	178	15
23.82	54	245	208	15
23.82	216	479	364	24

Based on the parametric study of the effect of structural weight on residual weight and on the overall spacecraft booster configuration, a specific design was chosen. Cross-plots of the study results for a 1,540-lb capsule are presented in Figs. 31 and 32. The gross properties of the capsule are chosen for the configuration study as follows:

Diameter, 16.0 ft

Maximum acceleration, 216 g

Weight, 1,540 lb

Heat shield, 330 lb (at 1.0 lb/ft² on fore cap and 0.25 lb/ft² on aft cone)

Maximum structure, 735 lb

Residual weight, 475 lb

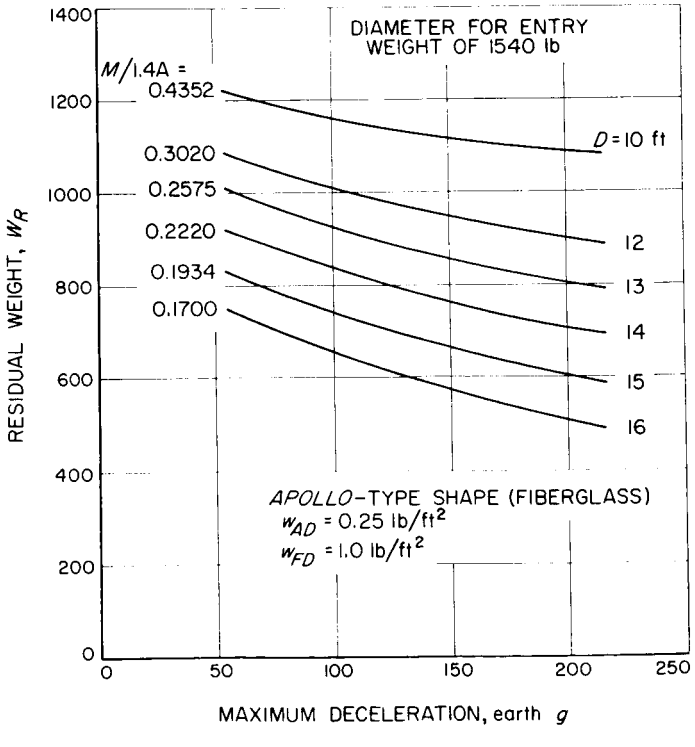

Fig. 31. Effect of maximum deceleration on residual weight for capsule entry weight of 1540 lb

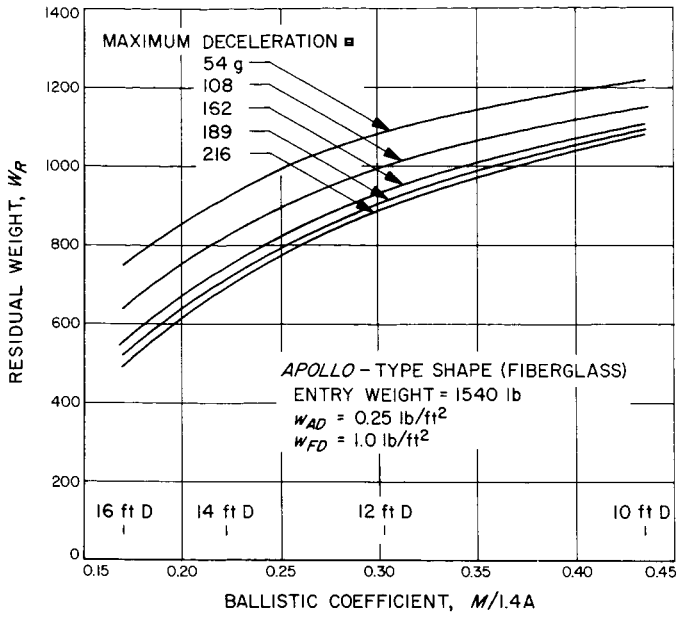

Fig. 32. Effect of ballistic coefficient on residual weight for capsule entry weight of 1540 lb

Figure 33 shows the controlling dimensions of this capsule.

For attachment of the residual weight at diameters other than 0.45 times the capsule diameter D, a qualitative statement can be made. The structural weight is minimum if the residual weight is supported at a diameter near $0.6D$, but there are no drastic differences for support diameters between $0.45D$ and $0.75D$. For diameters outside these limits, the weight shows a marked increase, and for small diameters the deflection increases radically. The effect is most pronounced for high M/C_DA capsules. If the residual weight is distributed at more than one closely spaced ring, the stresses away from the concentrated loads are similar to those resulting from a single ring load applied within the geometry limits of the multiple rings.

Axis-symmetric concentrated loads on the aft cone can be treated approximately as being distributed uniformly on the aft cone. The first-stage parachute and antenna, which are mounted in the apex of the aft cone, can be

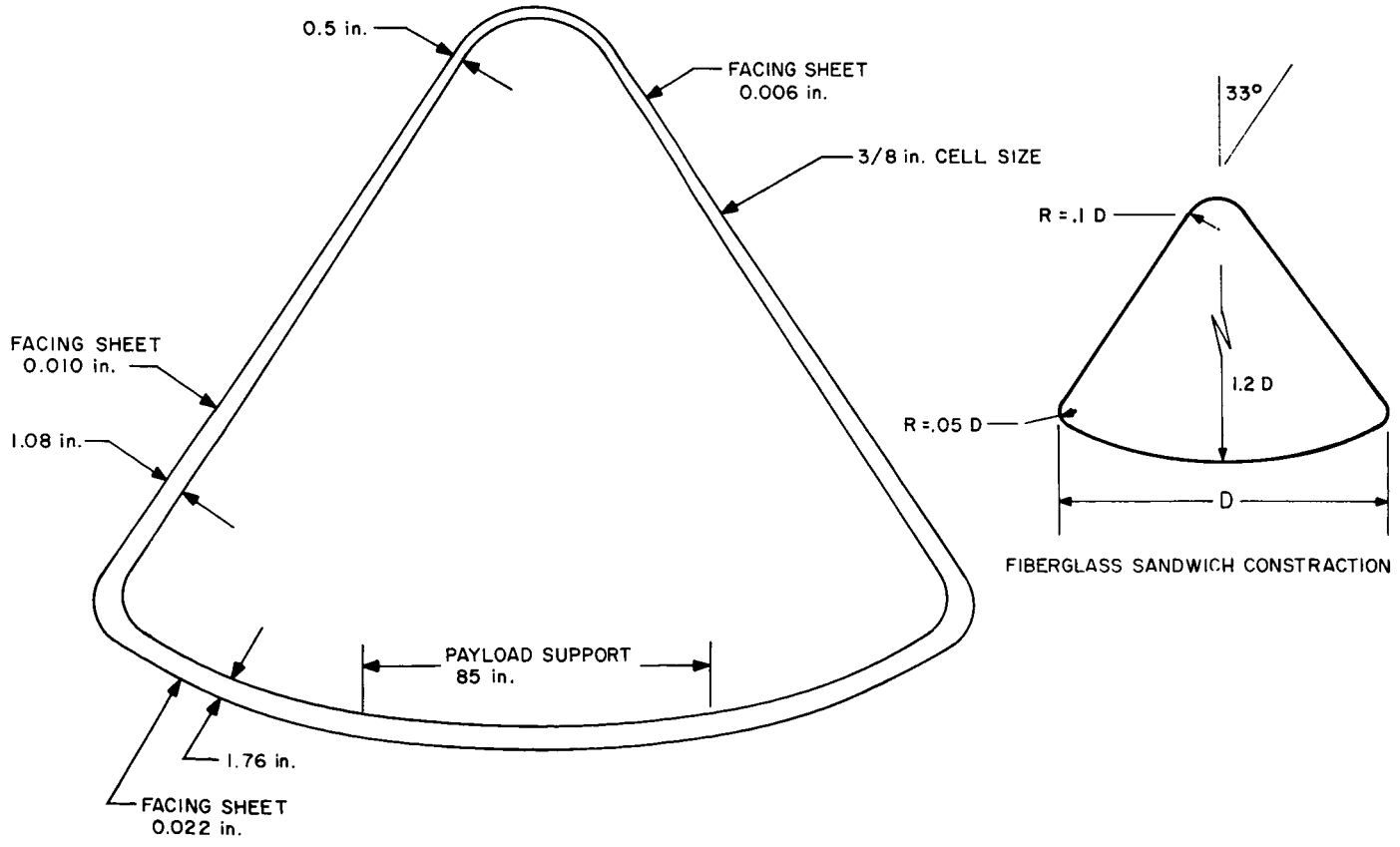

Fig. 33. 16-ft-diameter *Apollo*-type capsule structural dimensions capable of 200 g entry deceleration

treated in this manner. The 16 ft, 1,540-lb capsule with a 0.25-lb distributed load on the aft cone and a 144-lb concentrated load at the aft end can be treated as if it had a distributed load of $0.25 + 144/1.38\,(16)^2 = 0.66$ lb/ft^2, which would increase the aft cone structural weight by a factor of $(0.66 + 0.16/0.25 + 0.16)^{0.24} = 1.18$. The distributed weight is higher than that from which the scaling laws were developed, but is of the same order.

NOMENCLATURE[a]
(Section V)

a maximum instantaneous acceleration, Earth g

A_p projected area of capsule $\left(\frac{\pi}{4} D^2\right)$, sq ft

D capsule diameter, ft

L_E effective loading, lb/ft^2,

$$= \frac{W_T - W_{FD}}{A_p} = \frac{W_T}{A_p} - 1.2 w_{FD}$$

M mass of capsule $\left(\frac{W_T}{32.2}\right)$, slugs

w_{AD} constant unit weight superimposed on aft structure such as heat shield, lb/ft^2

W_{AD} distributed weight superimposed on aft structure, lb

W_{AS} weight of aft structure, lb

W_E total weight of capsule at entry = W_T + weight of material ablated up to time of maximum acceleration, lb

w_{FD} constant unit weight superimposed on forward structure such as heat shield, lb/ft^2

W_{FD} uniformly distributed weight superimposed on forward structure ($0.95 D^2 w_{FD}$), lb

W_{FS} weight of forward structure, lb

W_R residual weight equals total weight (at maximum loading) less structural weight of and distributed weights on shell, lb
$(W_T - W_{AS} - W_{FS} - W_{AD} - W_{FD})$

W_T total weight of capsule, lb

W_0 $W_T - W_{FD} = \left(\frac{\pi}{4} D^2 L_E\right)$, lb

Example:

Given: $M/1.25\,A_p = 0.2$; $D = 15$ ft; $w_{AD} = 0.25$; $a = 216$; $w_{FD} = 1.0$; weight of heat shield material ablated by time of maximum loading = 100 lb.

Find: L_E, W_R, W_T, W_E

$L_E = 0.2 \times 32.2 \times 1.25 - 1.2\,(1.0) = 6.85$ lb/ft^2 or use Fig. 30 from Fig. 28, using linear interpolation for $L_E = 6.85$,

$$W_{R\ minimum} = 1.15/2.0 \times 400 + 85/2.0 \times 650 = 506 \text{ lb.}$$

$$W_T = (6.85 + 1.2)\frac{\pi}{4} D^2 = 2530 \text{ lb.}$$

$$W_E = W_T + 100 = 2630 \text{ lb.}$$

[a] All weights except W_R are at time of maximum loading.

VI. CAPSULE TEMPERATURE CONTROL DURING EARTH–MARS TRANSFER

A. Configuration

A study was made of the problems of providing thermal control to a 16-ft-diameter *Apollo*-type capsule enclosed in a sterilization canister and mounted on a Sun-oriented spacecraft as in Fig. 34. Equipment inside the capsule requiring control and providing the source of internal heat included the survival payload, the descent payload, communications and support electronics, and the terminal decelerator. A deflection rocket was mounted on the capsule roll axis. The effects of using an RTG for power were not considered.

B. Temperature Ranges

It was assumed that the electronics systems could operate in a temperature range of 0 to 150°F and that they could withstand −50°F provided they were not turned on in this condition. The lower temperature limit of the deflection motor was estimated to be +20°F. Since the external ablation material undergoes a phase transition at low temperatures, a limit of −50°F was assumed. The lower temperature limit of parachute material was estimated to be 0°F. There appeared to be no lower temperature limit for the balsa wood in the survival payload.

C. Spacecraft–Capsule Cruise

1. Solar Independent Approach

During this mode the capsule is attached to the spacecraft. The configuration which received most attention in the study is shown in Fig. 34, in which the capsule is completely shaded by the spacecraft except during maneuvers. Because of the very low internal heat generated by the electronics equipment within the capsule and because of its large external surface area which radiates to black space, the primary temperature control problem is that of maintaining sufficiently high temperatures in the capsule.

It is important to observe that reduction of the surface area of the capsule/canister will reduce the amount of internal capsule heat needed to maintain the required capsule temperature. The design approach was to provide a high degree of insulation around the entire capsule and to dissipate several hundred watts of electrical power from the spacecraft into the capsule.

Any mechanical penetrations of the insulation should preferably be near the roll-axis and between the spacecraft and capsule to keep the electrical heating requirements to a minimum.

An alternative source of heat for the canister is radioisotopes. They would compromise, to some degree, the interplanetary particle and field experiments. However, they could be attached to the sterilization canister and jettisoned prior to initiation of measurement of planetary radiation.

The capsule temperature-control design will depend heavily on knowledge of the thermal properties of the material used for the insulation. The experimental determination of the effectiveness of the insulation will be difficult because the exterior temperature of the insulation will approach that of liquid-nitrogen-cooled shrouds in test chambers. A small-scale thermal model and/or lower chamber shroud temperatures for testing were considered as possible ways of making this determination.

Since the insulation characteristics should be maximized, the approach was to insulate the outside surface of the canister and to retain the canister until just prior to separation of the capsule from the spacecraft. This eliminates the necessity for sterilizing the insulation and keeping the canister intact for this period and is consistent with utilizing the canister for cosmic dust protection. The very low heat-transfer rates within the insulated capsule will provide an essentially uniform temperature in the capsule.

The rf-opaque characteristics of the high-efficiency insulation material will interface with the communications subsystem requirements for an rf-transparent capsule. This may not be a severe problem if the communications requirement is not imposed until after canister and insulation separation.

2. Sun-Dependent Approach

Another spacecraft/capsule configuration considered was one in which the capsule was illuminated by the Sun. This design could be accomplished in at least three possible ways. First, the sunlight could be allowed to pass through holes in the spacecraft. Second, a reflector could be placed at the edge of the annular spacecraft solar panel. Third, the capsule could be located on the sunward side of the spacecraft. Each of these alternatives

appears to greatly increase spacecraft/capsule interface problems over that of providing electrical heat to the capsule. In addition, the decrease in solar intensity could mean a temperature drop of the capsule in transit to Mars of as much as 125°F; the actual temperature change depends on the ratio of the solar to internal heat input.

D. Capsule Free-Flight

The temperature control of the capsule will be Sun-dependent during the period after the capsule is separated from the spacecraft and before entry into the planetary atmosphere. The intensity of the sunlight does not change significantly during the last few weeks of flight, so the average capsule temperature can be regulated by proper selection of capsule surface properties. The sunlit area will probably require a surface (such as a Tabor coating) with a ratio of solar absorptance to infrared emittance in excess of unity.

The critical local temperature is that of the ablator on the shaded portion of the capsule. If the aero-shell of the capsule is fabricated of fiberglass honeycomb, there will tend to be large temperature gradients through the low-conductivity shell wall. A very low emittance on the shaded surface will be required to maintain the ablator there at a sufficiently high temperature. This in turn implies that slow, random tumbling of the capsule probably cannot be allowed, and Sun orientation of the capsule appears to be a requirement.

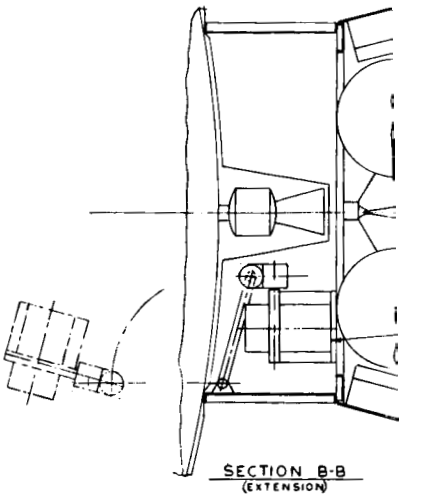

SECTION B-B
(EXTENSION)

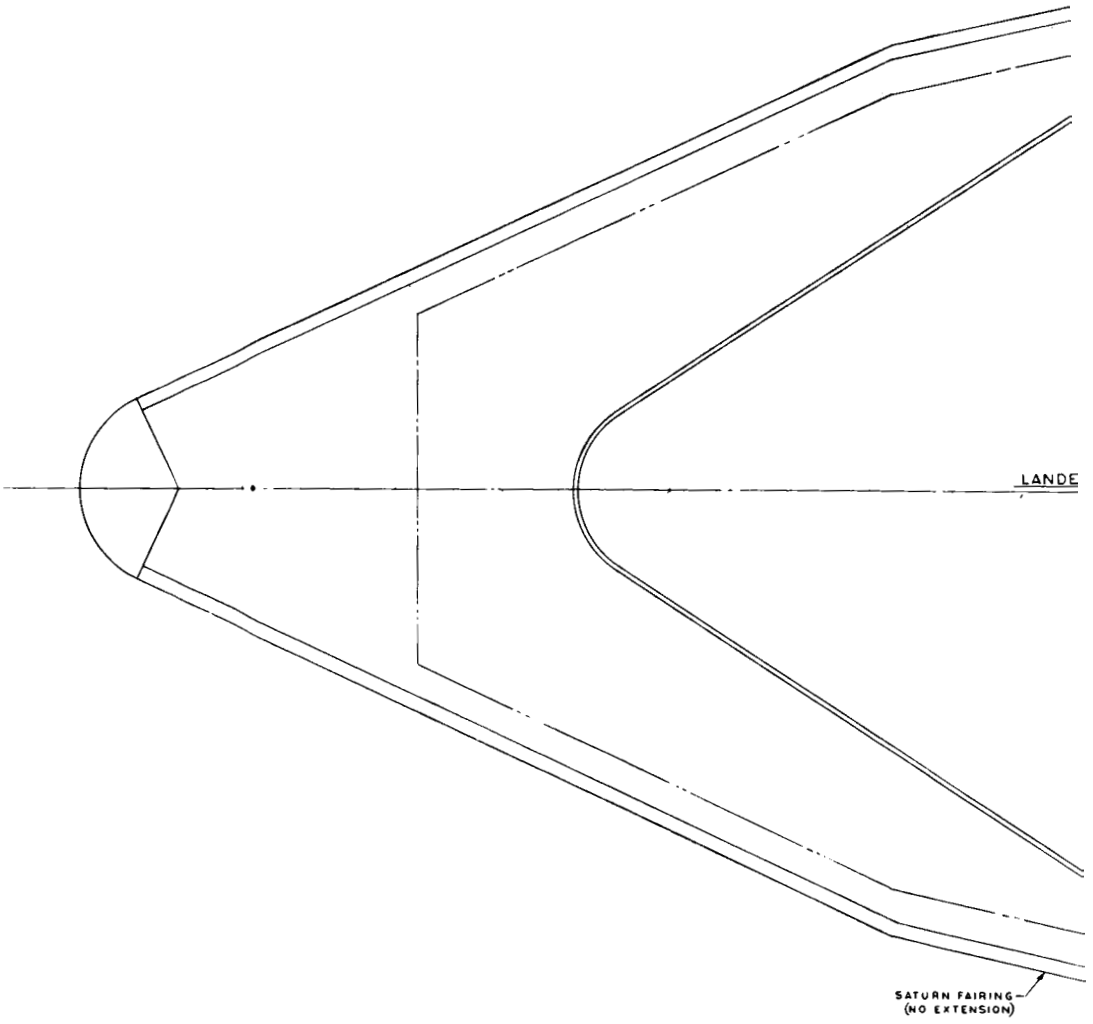

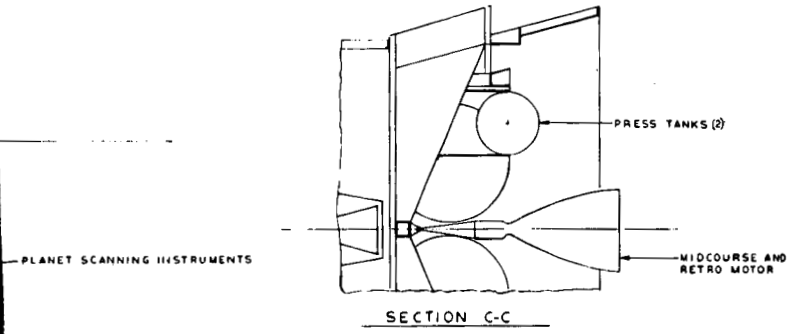

SECTION C-C

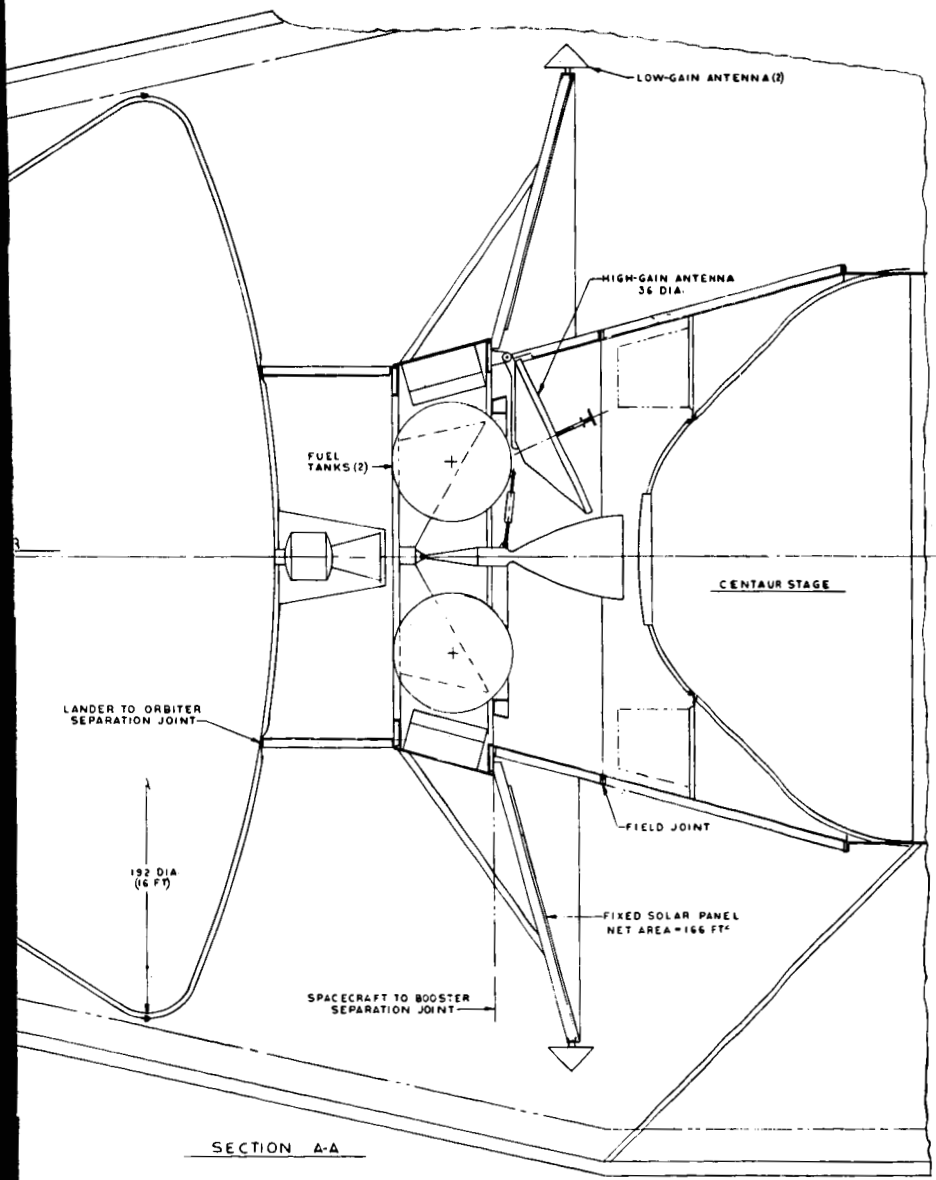

SECTION A-A

27 (2)

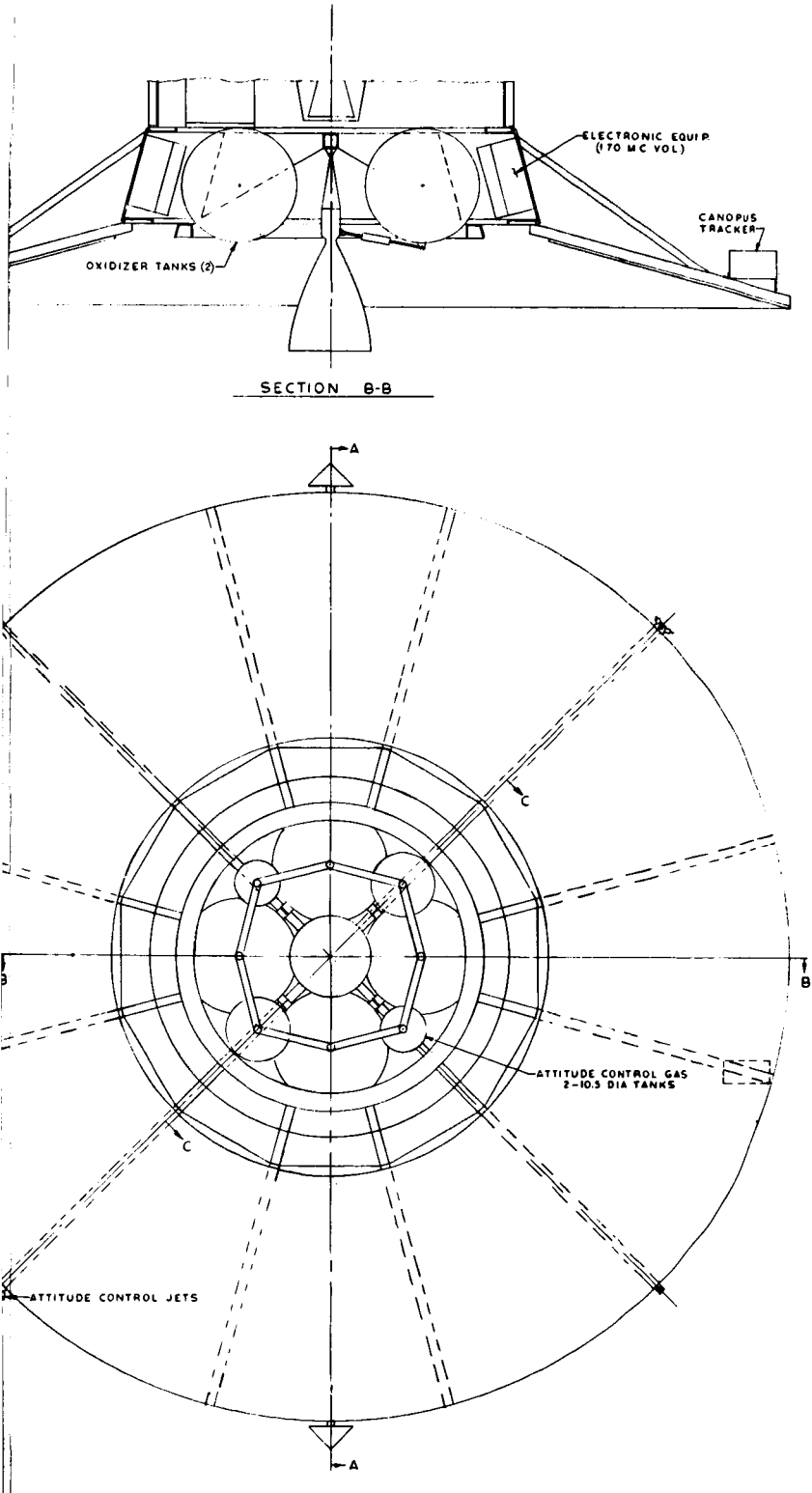

Fig. 34. A possible capsule–spacecraft launch configuration

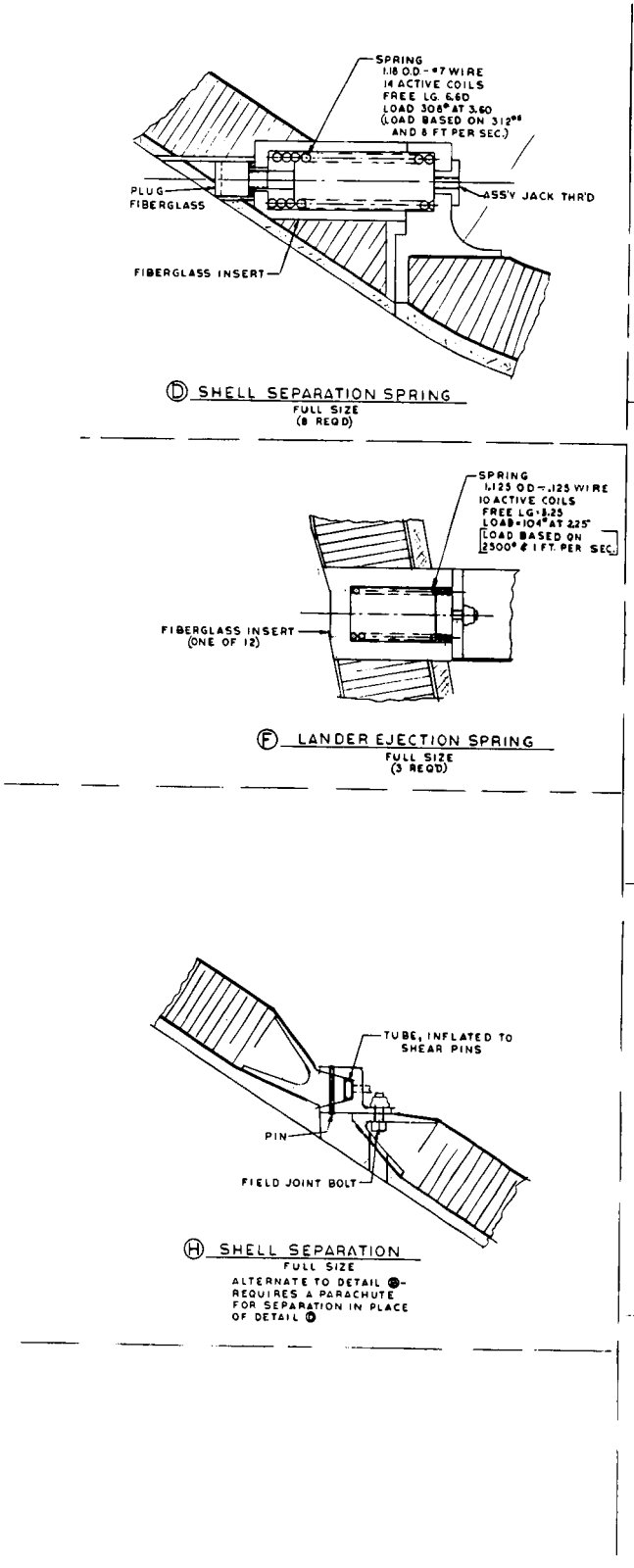

Fig. 35. Capsule configuration, ballistic mode

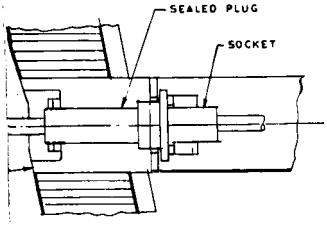

ELECTRICAL TRANSFER
BUS TO LANDER
FULL SIZE
(2 REQ'D)

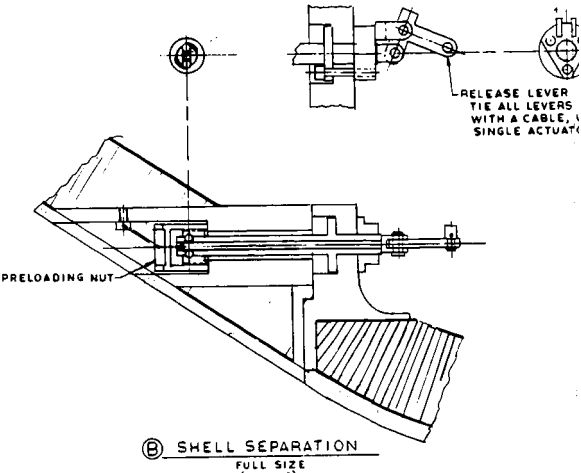

Ⓑ SHELL SEPARATION
FULL SIZE
(4 REQ'D)

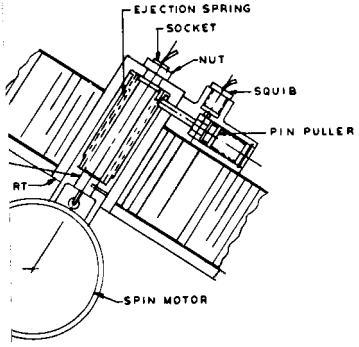

TOR MOUNTING AND
ECTION MECH.
FULL SIZE
TYP. 4 PLACES

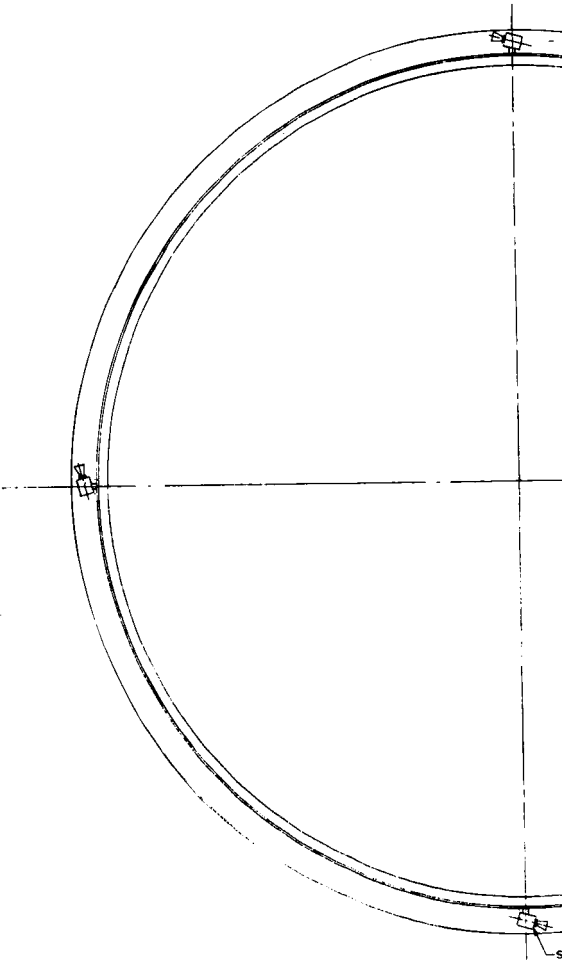

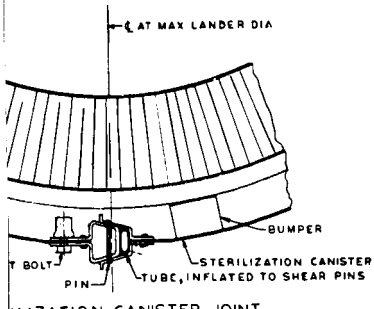

ILIZATION CANISTER JOINT
FULL SIZE

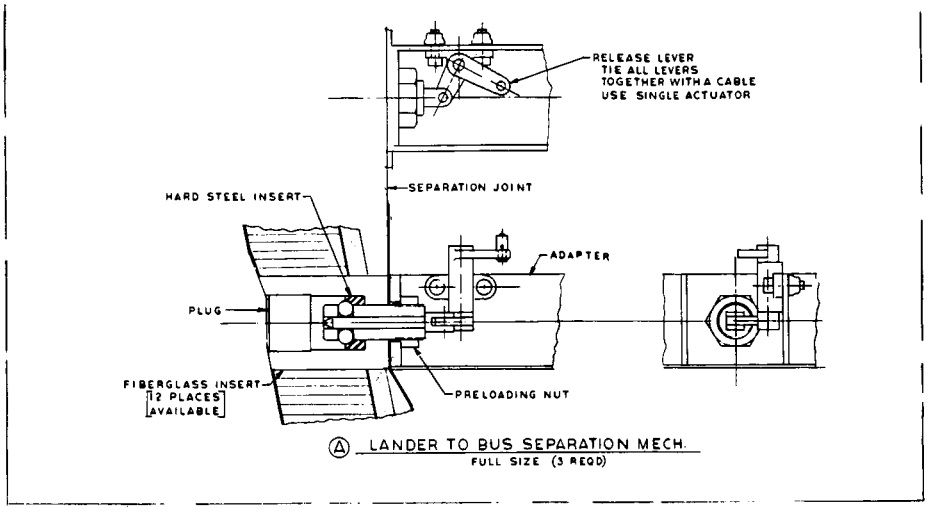

Ⓐ LANDER TO BUS SEPARATION MECH.
FULL SIZE (3 REQD)

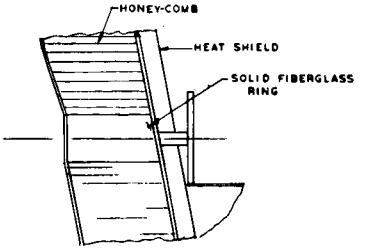

FULL SIZE SECTION

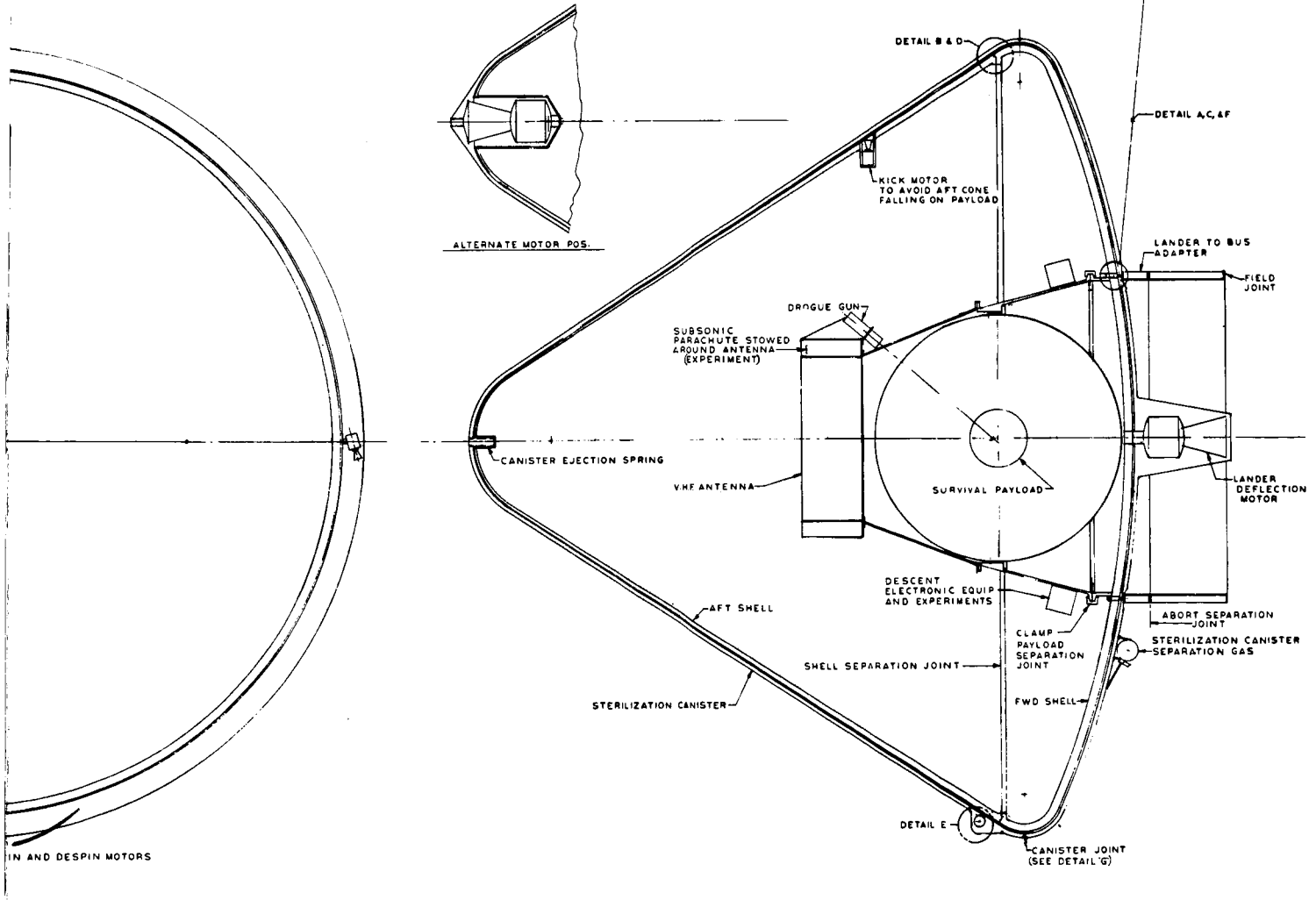

ALTERNATE MOTOR POS.

IN AND DESPIN MOTORS

28-8

(3)

VII. CAPSULE CONFIGURATION

Several guideline assumptions were listed in Section I. These, obviously, shaped the configuration to be studied, and changes in these guidelines would result in different conclusions.

Most of the discussion on capsule configuration is applicable to both the ballistic and parachute modes of descent. Specific reference will be made when the discussion relates to only one of the modes. Figure 35 shows a configuration to accomplish the ballistic mode (with a parachute experiment); Fig. 36 shows a configuration to accomplish the parachute mode.

A. Capsule Size: Envelope Constraint

An objective that a single *Apollo*-type shell be designed capable of both a ballistic and parachute mode of descent affected the capsule size. The structural weight parametric study shows that the ballistic mode payload optimizes at something less than 16 ft. However, the payload for the parachute mode increases with diameter. Therefore, the largest possible diameter is desirable to optimize for this objective.

The existing *Saturn IB* shroud envelope together with the requirement that the capsule be supported on the spacecraft during launch fixes the maximum diameter. Allowing for a reasonable spacecraft height, a 3-in. canister joint clearance, and a 3-in. dynamic clearance between the sterilization canister and the shroud envelope restricts the capsule diameter to 16 ft.

A possible spacecraft/capsule configuration is shown in Fig. 34. There is an advantage in the parachute mode if the shroud were to be lengthened about 10 ft in the cylindrical section. The constraint would then be the shroud envelope base diameter of 240 in. Even then, however, the capsule diameter maximizes at 19 ft when allowance is made for the canister and dynamic clearances.

Capsule configurations using the shroud envelope constraints and the structural sizing requirements of the previous sections are shown in Figs. 35 and 36. Figure 35 presents a possible solution to integrating the subsystem requirements for a ballistic mode descent with a subsonic parachute experiment. Figure 36 shows the first-stage supersonic as well as the second-stage parachute terminal-descent subsystems and other associated equipment added. The parachutes are relied upon to reduce the payload impact velocity. Many comments pertain to both capsule configurations and will be presented in relationship to the ballistic capsule because configuration problems are identical whether a subsonic parachute is used as a terminal decelerator or carried as an experiment. The configuration problems related to incorporating the first-stage parachute descent system will then be discussed.

B. Capsule–Spacecraft Interface

To satisfy the sterilization requirements, the capsule is attached to the top of the spacecraft by an adapter which is part of the capsule system. The adapter contains a field joint, which attaches it to the spacecraft, and a capsule separation joint, which is inside the sterilization canister. A second separation joint, outside the canister, is provided to serve as a failure mode device should the canister cover or the capsule fail to separate normally. This would permit the capsule phase of the mission to be aborted while still accomplishing the orbit phase without penalizing the orbit injection propulsion weight.

The interface between the capsule and the adapter consists of a continuous compression surface with several discrete bosses which are used for mechanical hold-down and separation of the capsule, separation spring housings, and electrical disconnect junctions for the spacecraft-to-capsule umbilicals. Figure 35 presents schemes for mechanizing these devices. Pyrotechnics will most likely be used to disengage these devices at separation.

A structural load path for launch loads is provided in the flexible shell by the stiffness provided by the payload support structure which attaches at the same ring. This structure will distribute the concentrated loads developed at the discrete tie-down points. Axial compression is transferred through the continuous ring-adapter faying surface.

C. Sterilization Canister

The sterilization canister is a shell which cocoons the capsule prior to heat sterilization and remains intact until just before capsule separation. It is supported by the capsule shell during launch. However, the canister shell is to serve as a micrometeoroid barrier during the transfer to Mars, which may require shell thicknesses structurally capable of withstanding launch loads without capsule support. Several difficult problems are associated with

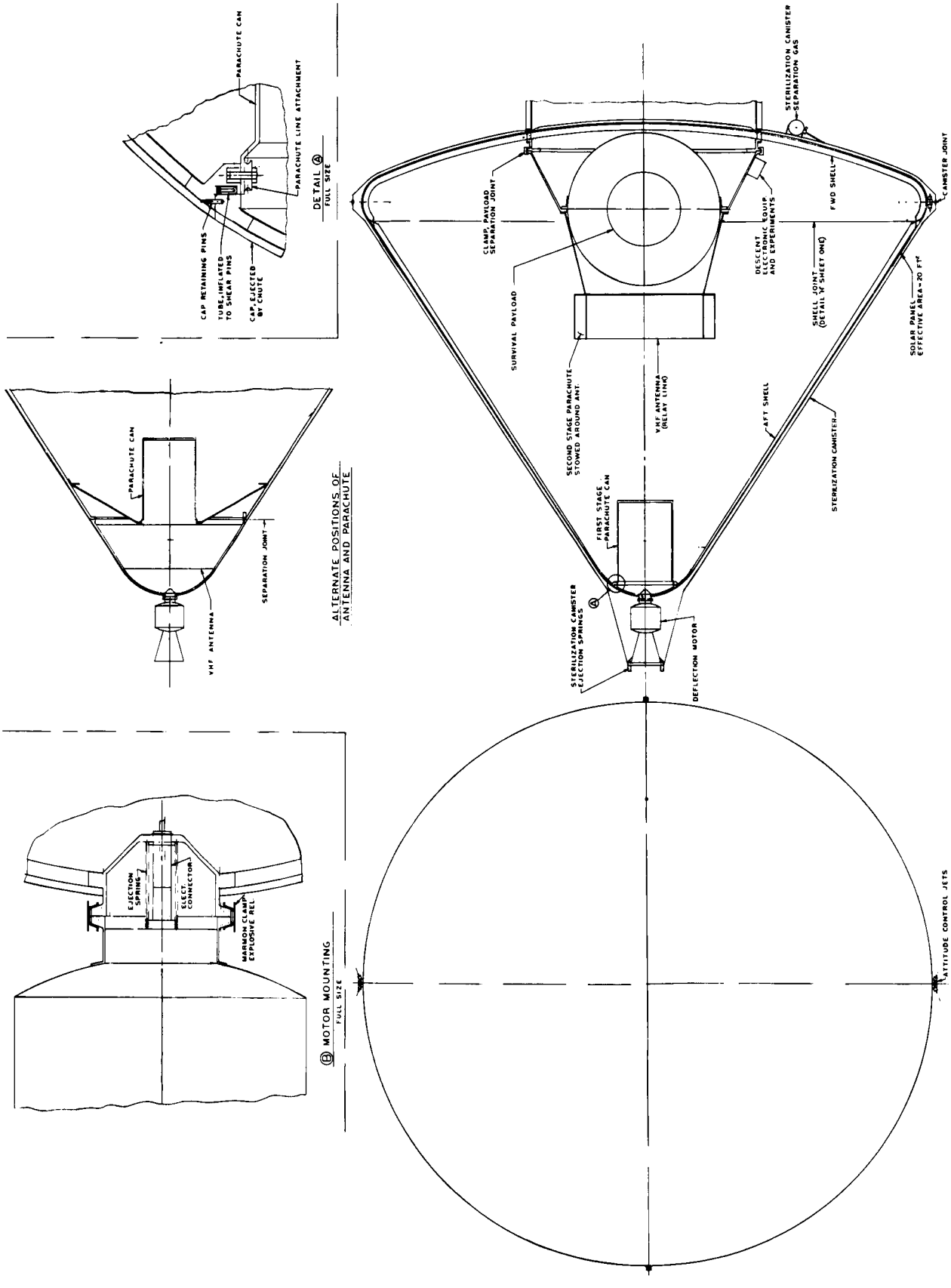

Fig. 36. Capsule configuration, two-stage parachute descent mode

the canister. Biological constraints require that it be sealed. However, a mechanical joint is required at its maximum diameter to permit capsule installation. This joint can be sealed at assembly by bonding the surfaces and curing during the sterilization cycle, but disassembly may be difficult. Welding on final assembly does not appear feasible. Additionally, the canister (and capsule) must be allowed to equalize internal and external pressures during and after heat sterilization and during launch. A biological filter in a porting device is required.

The conical section of the canister must be jettisoned prior to capsule release. This requirement necessitates a separation joint at the maximum diameter and a spring device to impart a proper velocity increment to the cone. A shaped charge appears (at first look) to be usable for this application. However, because of the many severe disadvantages of such a device, a mechanical separation joint was investigated. A joint such as that shown in view G of Fig. 35 could effect separation. The joint is pinned at intervals to maintain structural integrity, and these pins are sheared by pressurizing a flexible tube which is oval at installation. The joint is self-contained and can be made mechanically reliable if it can be made an adequate biological barrier. The biological barrier requirement plagues all mechanical joints investigated.

D. Structural Shell

The structural configuration optimized for the 16-ft-diameter capsule and sized to withstand the ballistic (90 deg) entry loadings is shown in Fig. 33. Fiberglass sandwich construction is used in both the forebody and the aft cone. Structural dimensions were obtained using the heat shield weight as the only external distributed inertial loading on the structure.

The ballistic coefficient $M/1.4A = 0.17$ for the Mars design atmosphere is so low that structural weight becomes a large percentage of the entry weight. Thus, very-light-gage surface sheets are required. The structural sizes, with the tight tolerances and mechanical properties which must accompany them, represent an extension for the current fabrication practices.

An assembly joint is required in the capsule shell to facilitate installation. Any joint in the light fiberglass shell will be many times heavier than the continuous shell Thus, this joint diameter should be minimized. The shell, however, is to be designed for both ballistic and parachute descent, and the latter mode requires that a portion of the aft cone be jettisoned, necessitating a separation joint. These two requirements are incorporated into one joint design at a diameter just under the maximum, as shown in Fig. 35.

E. Guidance and Control and Pre-Entry Power

Two methods have been considered for guidance of the capsule during the deflection thrusting and the rest of the pre-entry flight: (1) spin stabilization and (2) active attitude control. In the former mode, spin rockets of high thrust and short burn time spin up the capsule immediately after separation from the spacecraft. The capsule is left spinning until just before entry, when it is de-spun so that the entry aerodynamics stability is not jeopardized. Batteries supply power through the entry phase in this mode and are destroyed upon impact.

A cold gas system could provide capsule attitude control using Sun orientation during the pre-entry phase, thus allowing a solar array to be used for power. The deflection maneuver is accomplished by releasing the capsule in the correct attitude with gyro lock. After the maneuver, the capsule is put on acive attitude control using the Sun as a reference and controlling roll rate, which eliminates the need for a second reference.

F. Communications: Pre-Entry and Entry

A VHF relay communications link is used during the pre-entry and entry phase of the capsule flight. The electronics required for this subsystem are packaged on the payload support structure. The transmission frequency requires a large antenna; a 40-in.-diameter cylinder 15 in. long is used for the envelope in this study. The capsule shell is rf-transparent because of the communications requirement, and the antenna is located to transmit through the aft cone. The antenna and its support structure must withstand entry loads of upwards of 200 g, but it is designed to break up at impact in a manner to ensure that it does not imbed itself in the "upper" surface of the payload impact attenuator.

Communications problems unique to the parachute descent mode will be discussed in a later section.

G. Deflection Rocket

The capsule deflection mode of operations is assumed in this configuration study. The envelope for the probable maximum size for the deflection rocket is shown in Fig. 35. Two possible locations for this rocket are shown.

In all cases, the burned-out rocket is jettisoned immediately after its burn. Several considerations enter into the selection of the location for the rocket. The sketches below help visualize some of these considerations. All three cases assume that the capsule is in the shade of the Sun-oriented spacecraft up to the time of capsule separation.

Figure 37a shows the capsule with the deflection rocket on the front shield. Release of the capsule is made with minimum spacecraft maneuvers. However, the front heat shield is nominally in the Sun and the capsule angle of attack at Mars entry is unfavorable. The relay communications link is complicated because the antenna location must permit radiation through the front shield.

The other possibility for the rocket in this location was not considered. It requires the capsule to have its own guidance and control for making turns after release from the spacecraft, which remains in its cruise mode.

Placement of the rocket on the aft cone, as shown in Fig. 37bc, improves the entry angle of attack and nominally places the capsule aft cone in the Sun. This orientation reduces the temperature control and antenna location problems. However, in the Fig. 37b orientation a large capsule attitude change is required to point the rocket thrust correctly. This requirement would force the capsule to have its own guidance and control subsystem. Figure 37c shows the option in which the spacecraft performs the attitude turns prior to capsule release. In this case, either the capsule or the bus must be deflected laterally in order to ensure that the capsule does not collide with the bus. Guidance errors, consistent with accuracy requirements on the capsule deflection maneuver, are not adequate to prevent impact. The relay link communications direction is initially forward of the capsule and changes rapidly during the flyby. The range is so short that no insurmountable communication problem is anticipated.

H. Payload Integration

The landed payload is distinguished from the descent payload in that the latter does not have to survive landing impact. Any measurement taken by the descent science is relayed to the spacecraft and is also stored in the lander payload for direct-link playback to Earth. An umbilical to the data storage of the landed payload is required. This should cause no different problems from the ground checkout umbilical, unless the payload is separated from the forebody during the parachute experiment. This operation would require a disconnect mechanism.

The landed scientific payload is packaged as a sphere and is enclosed with an omnidirectional impact attenuator. The payload configuration is discussed in a later section. Capsule–payload interactions considerations for the ballistic capsule mode will be discussed here. As with the other subsystems, the effects of adding a parachute terminal descent are discussed separately.

The spherical payload system is mounted to the forebody structure by a ring support. As previously stated, this structure serves to distribute launch loads to the shell as well as to support the payload sphere. The preentry engineering and science electronics are also packaged around this support so that the loads may be adequately distributed to the fiberglass shell. An assembly or field joint exists at the capsule shell surface and another at the payload surface. No payload separation joints are required since the total capsule vehicle impacts as a unit.

The reliability of the landed payload through impact survival and the establishment of direct communication is hard to define because of several factors. The aft cone shell and the VHF antenna will be destroyed upon impact. Jettison of the impact attenuator from the payload sphere does not seem too feasible because it will be difficult to show that the aft cone shell will completely clear the sphere. It is imperative, however, that no metal be imbedded into the impact attenuator in a location which will degrade the S-band antenna pattern.

There has been much thought given to a design definition of the Mars surface. One used for this study is presented in Ref. 2. Briefly, it varies from combinations of hard surfaces and inclinations of up to 30 deg with 4-in.-diameter rocks to soft, yielding material deposited over a hard, unyielding surface. Perhaps the biggest hazard presented to the lander during impact attenuation is the equipment packaged around it which will, for any appreciable oscillatory angle at impact, be the "surface" upon which impact takes place. The degrading effect on the antenna pattern of either a rock or a piece of equipment imbedded in the attenuation material leads to the conclusion that the impact attenuation material must be jettisoned after impact. Thus there can be incompatibilities in the requirements for the ballistic mode of descent. Though there are several additional operations

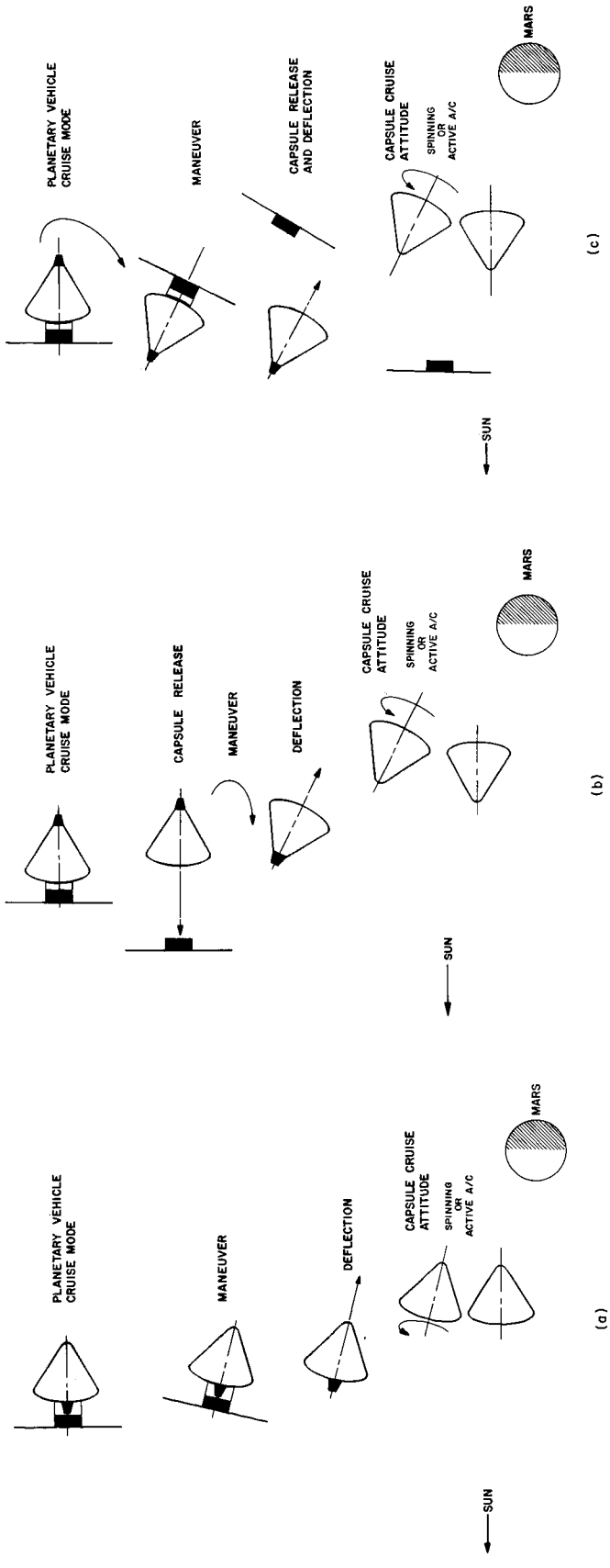

Fig. 37. Some geometric implications of the capsule configuration

to successfully parachute deployment, it appears desirable, if not mandatory, to have the payload clear of the entry capsule at impact.

I. Parachute Descent Mode

Several changes to the total capsule system are required when the parachute subsystems, either supersonic or subsonic, or both, are added. These changes will be discussed by starting with the effects on the capsule shell and progressing through to the payload. The configuration of Fig. 36 shows both a supersonic and subsonic chute, though a subsonic chute alone can be used, as shown in Fig. 35.

The reliable deployment of a supersonic parachute requires that it be mounted on the centerline of the vehicle. This is best accomplished by placing the chute canister in the apex of the aft cone. Placing this weight that far aft, moves the center of gravity aft of the location used in the trajectory studies for rearward entry effects. It is most probable that the rearward entry condition could not be tolerated with the supersonic chute configurations studied.

The requirements placed on the stowed location of the subsonic parachute are less stringent than for the supersonic chute. The packaging configuration, which is subject to much development testing, is perhaps more important in achieving reliable deployment. The configuration shown on Fig. 36 represents a system which requires further study to determine its acceptability. The chute is packaged around the VHF relay link antenna, and its shroud lines attach to the payload. Inflation of the chute pulls the landed payload sphere and the descent science from the forebody structure. The landed payload sphere is released from the descent science support structure immediately prior to impact, thus removing the sphere from the expendable equipment which could jeopardize post-impact landed operations if left intact with the landed sphere. Consideration must be given to the spherical payload rolling around on the slopes of the Martian surface. Initiation of capsule landed operations such as jettisoning of the attenuator material must account for this possibility.

The parachute mode of descent adds complexity to the capsule shell design and required sequencing and operations. If the parachute is carried only as an experiment, all of the complications are retained, but the velocity advantage cannot be utilized in the impact attenuator design. Several joints are required for the separations which must occur, and sensors are needed to initiate deployment and release of the parachutes.

Two possible arrangements for locating the supersonic chute are shown in Fig. 36. The deflection rocket is jettisoned after its use, as previously indicated, so that its empty weight is not carried into Mars entry. Should adequate VHF antenna coverage be obtained with only one antenna, the parachute can be located in the apex of the aft cone. A joint is required to release the cover to permit mortar deployment of the parachute. If a second VHF antenna is required, an alternate configuration is shown in Fig. 36 in which the cover and the second antenna are jettisoned to permit parachute deployment. Of course, disconnecting the coax line complicates this operation.

There is an assembly joint required at a diameter which is determined by payload installation requirements. To accommodate the subsonic parachute mode, as previousy mentioned, a separation joint is built into this assembly joint. Some of the considerations applicable to the canister joint design also apply to this joint. A shaped charge which would rupture the continuous shell would be a lightweight approach to the joint design. However, the design would require the insertion of a solid section at the joint because the shaped charge is not generally applicable to cutting a fiberglass sandwich structure—especially one with a thickness of over 1 in. Although the shaped charge approach did not appear favorable, this approach should receive further investigation.

As shown in View H of Fig. 35, the solution to the separation joint design adopted for this study is a completely contained joint, similar to the canister mechanical joint. A thin-walled tube is deformed at installation, and separation is effected by shearing of pins through inflation of the tube. Desirable characteristics of the design are the lack of debris which might damage the capsule payload and the apparent reliability of the joint.

Once the separation joint is activated, the aft cone can be removed by using the first-stage parachute to pull it off. Should only a second-stage parachute be used, springs or a rocket must be used to effect separation. Either approach requires that the cone be deflected so that it won't overtake and collide with the payload after deployment of the second-stage parachute. Another problem common to both approaches (but more serious for the spring separation) is caused by the oscillations of the capsule. Relative displacements of the aft cone and the

forebody-payload during the separation period are not well understood. A potentially serious impact condition exists if the cone collides with the antenna or payload. It seems reasonable to expect separation displacements such that the antenna must be designed to withstand the impact or else protective guiderails must be added to the separation system.

The subsonic parachute can be pulled out by the aft cone during its separation. This operation requires a pyrotechnic device to separate the parachute from the aft cone tether. An alternate approach would be to deploy a drogue chute by a mortar and use it to deploy the large subsonic chute. In either case, another pyrotechnic device is required to cut the reefing lines to initiate parachute inflation.

Both the descent payload and the landed payload are to be separated from the forebody by the subsonic (second-stage) parachute. A marmon clamp type of joint has been selected for this application, and it is located just aft of the forebody shell. It would be more advantageous to locate this joint at the sphere equator if the descent payload can be packaged on the antenna support structure without forcing the cg out of its permissible tolerance.

A final joint is required to separate the spherical landed payload from the expendable descent science and the subsonic parachute. The landed payload must be unencumbered to allow removal of the attenuation material and reliable exposure of the payload science and direct-link communications antenna. A sensor is required to initiate this separation just prior to impact.

Required operations and their effect on landed payload configurations are discussed in a following section.

VIII. IMPACT VELOCITY FOR MAXIMUM PARACHUTE-LANDED PAYLOAD

Landed payload may be maximized by trading impact attenuator weight against parachute weight, since the weights of these two terminal deceleration aids have contrary functional dependence on descent velocity at impact. Parachute weight varies approximately inversely with the square of the descent velocity at impact, while impact attenuator weight varies approximately directly with the impact velocity. Assuming a terminal velocity condition and a 14-mb surface pressure, atmosphere model 5 has the lowest density at the surface, and hence will produce the highest impact velocity (largest attenuator weight) for a given parachute size and weight and, conversely, the largest parachute weight and size for a given impact velocity. The impact velocity used to design the attenuator (assumed to be balsa wood) was considered to be the vector sum of the parachute descent velocity and a 100 ft/sec, 30-deg-downslope wind.

The calculation procedure employed was:

1. Assume:
   a. Terminal descent system weight at parachute deployment (entry weight minus aeroshell weight).
   b. One of a series of descent velocities.
   c. A 2-ft-diameter spherical payload.
   d. A thick balsa wood shell entirely surrounding payload as impact attenuator.
2. Calculation:
   a. Calculate parachute weight based on descent velocity and weight 1a.

b. Subtract weight 2a plus jettisoned 125-lb entry subsystem from weight 1a giving (payload + attenuator) weight.

c. Calculate impact velocity.

d. Calculate attenuator weight using method of Ref. 1 (page 9-4), based on impact weight (2b) and impact velocity (2c).

e. Add a 5-in. thickness of balsa wood for protection against small-object penetration (4-in.-diameter rock) plus a thin surface cover of fiberglass.

f. Weights 2b − 2d − 2e = landed payload weight.

g. Minimal iteration is needed to make the sum of elemental weights equal total descent weight 1a.

The results of repeating this procedure for several assumed descent velocities were plotted as curves of landed payload vs descent velocity, which have the form shown in Fig. 38. It was found that the landed payload reached a rather flat maximum in the descent velocity range from 100 to 150 ft/sec. The value of this maximum varies nearly linearly with terminal descent system weight 1a. The optimum velocity range will probably shift somewhat for assumed atmosphere models other than 5, and for impact attenuation materials other thar balsa wood, etc.

Calculation of attenuator weight, Step 2d, assumes that weight other than attenuator weight is all in the payload, whereas Step 2e removes some of the assumed payload weight and applies it on exterior as a rock buffer. Thus, the payload density (an important factor in attenuator weight calculation) has been assumed both too high and too low, and iteration is required to converge on a consistent distribution of the weights.

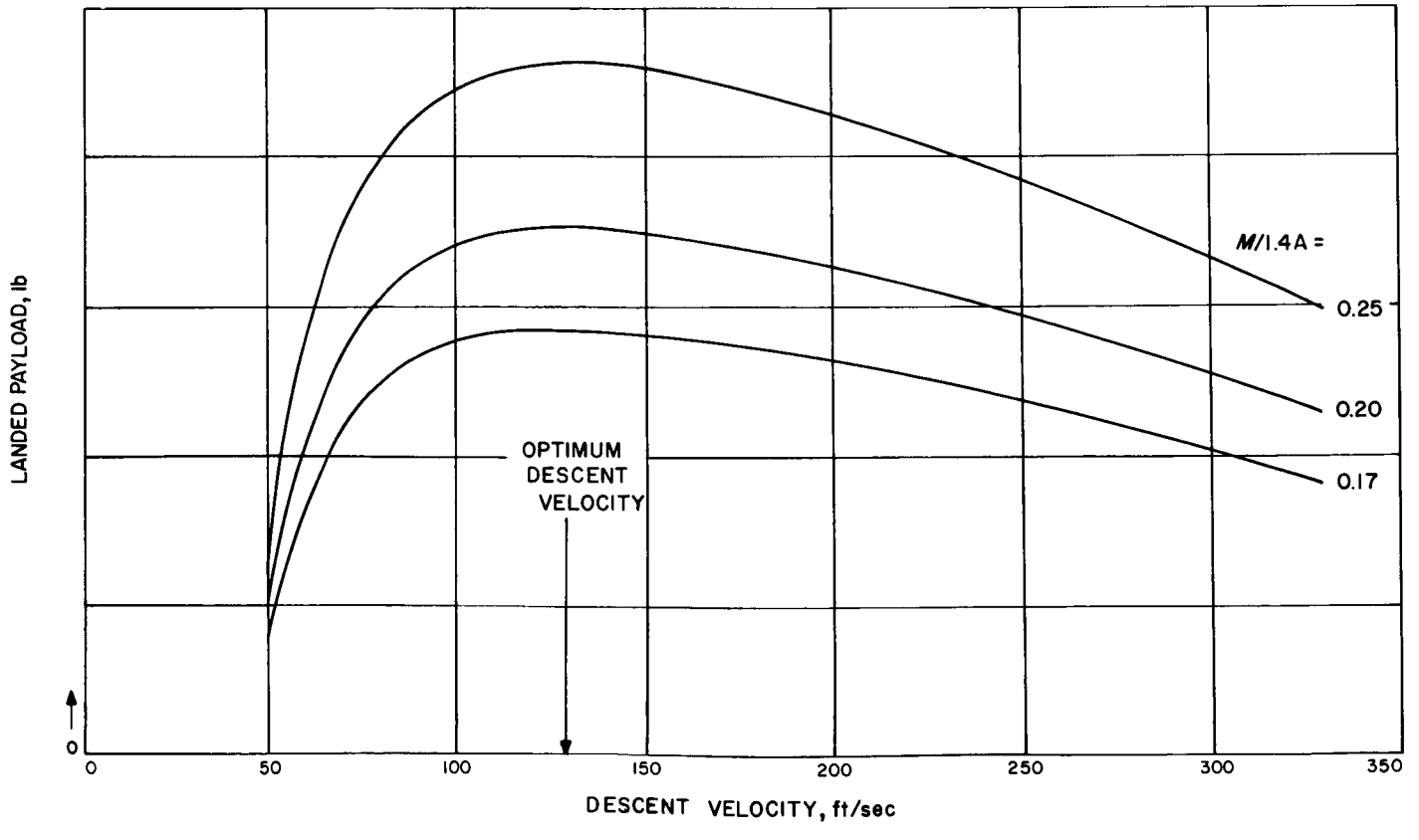

Fig. 38. Landed payload vs descent velocity

IX. IMPACT ATTENUATOR DESIGN

The impact attenuator under consideration consists of a spherical payload contained within a thick spherical shell of balsa wood. The spherical balsa shell will be constructed of segments of balsa in sufficient number so that the approximate grain direction throughout the balsa sphere is radial (Fig. 39). Radial grain is desirable because of the omnidirectional impact requirements placed on the attenuator and the higher crushing strength parallel to the grain.

A proven theory has not been established for the crushing of a spherical impact attenuator; therefore, it is necessary to assume a crushing law which is consistent with experimental indications. One theory assumes that the crushing strength of balsa wood varies as the cosine of the angle of inclination to the grain, thereby assigning density dependent values of σ as the crushing strength parallel to the grain, and 0 as the crushing strength perpendicular to the grain. Experiments have shown that the perpendicular crushing strength varies from approximately 8 to 18% of the crushing strength parallel to the grain, depending upon the density of the balsa.

A second theory, which has been developed by the Aeronutronic Division of Philco (Ref. 12), is similar to the above-mentioned theory but extends the analysis to include the effect of the cross-grain crushing strength. The following analysis uses a technique which is a slight modification of that developed by Aeronutronic. The modification involves only the variable of integration; however, a small amount of algebraic manipulation will show that the resulting energy and force expressions are identical to those obtained in the Aeronutronic analysis.

The Mars surface model which is specified in Ref. 2 indicates a number of different possible impact surface configurations. At this time only two of the possibilities will be considered. They are: (1) a smooth, flat, rigid impact surface, and (2) a flat, rigid impact surface with a 10-cm (4-in.) diameter rock present.

The analysis presented is designed to determine the required dimensions of the balsa attenuator for a given impact velocity, payload weight, and payload radius for impact on a flat surface with or without a 4-in.-diameter rock present. The technique allows a quick calculation using an iterative procedure. Three or four short iterations will bring the calculated radius to within 0.1 in. of the desired number.

A. Analysis

Consider an incremental element (Fig. 40) of balsa at the interface of the limiter sphere and the flat, rigid impact surface to be subjected to crushing both perpendicular to and parallel to the grain. Summing forces in the vertical direction yield the equation

$$dF_v = 2\pi r^2 \sigma (\sin\theta \cos\theta + 2\alpha \sin^2\theta \tan\theta)\, d\theta \qquad (1)$$

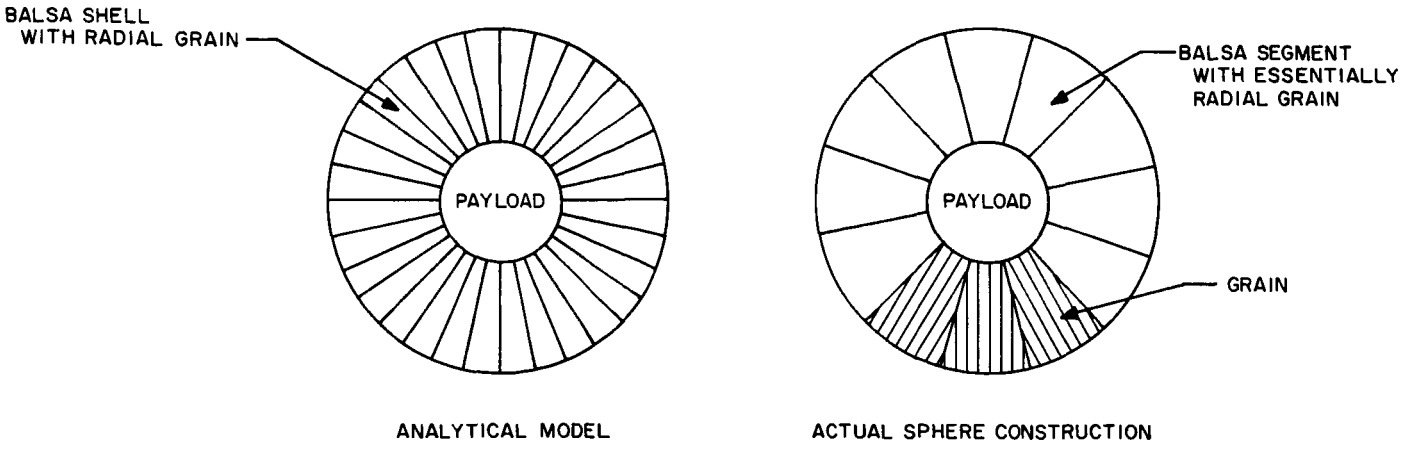

Fig. 39. Balsa impact attenuator

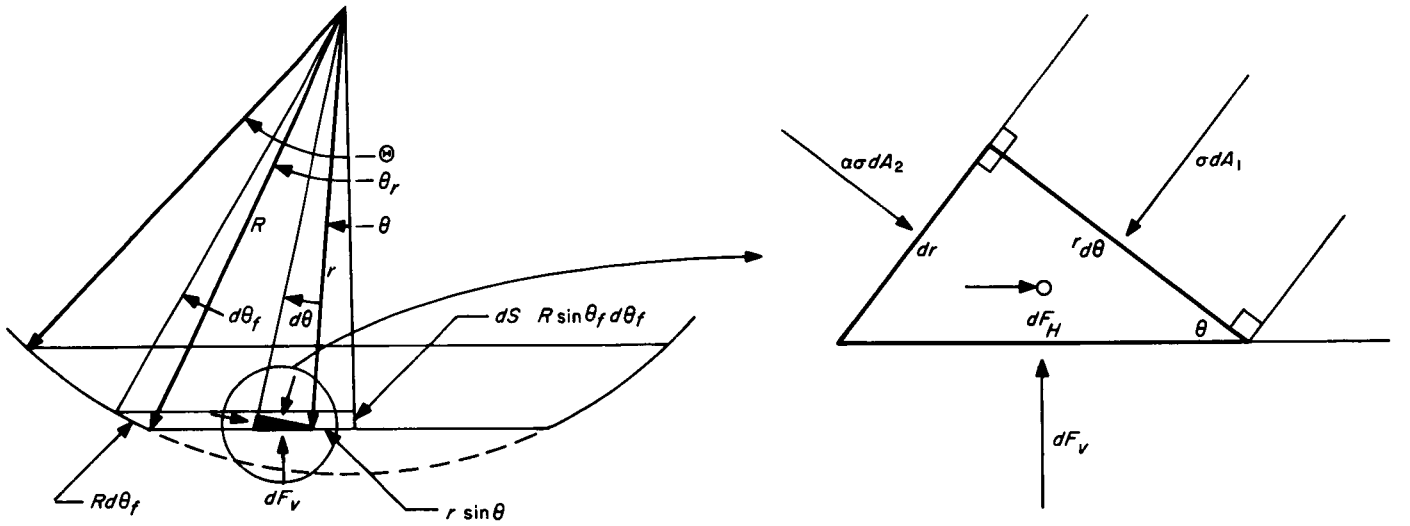

Fig. 40. Typical balsa incremental element at lander-impact surface interface

Noting that $r = R(\cos\theta_f/\cos\theta)$ and substituting in Eq. (1), we get

$$dF_v = 2\pi R^2\sigma\cos^2\theta_f(\tan\theta + \alpha\tan^3\theta)\,d\theta \qquad (2)$$

Integrating from 0 to θ_f,

$$F_v = \pi R^2\sigma\,[\alpha\sin^2\theta_f + 2(\alpha - 1)\cos^2\theta_f\ln\cos\theta_f] \qquad (3)$$

This force enables us to determine the acceleration of the limiter at this point in crushing. The acceleration is

$$a = \frac{F_v}{m}$$

Dividing both sides by g, we get

$$\frac{a}{g} = \frac{F_v}{mg} = \frac{F_v}{W} = n$$

The above equation assumes that change in mass during the crushing is small and may be neglected.

The energy dissipated in crushing is given by

$$E = \int F_v\,dS$$

but,

$$dS = R\sin\theta_f\,d\theta_f$$

Then,

$$E = \int_0^{\Theta} F_v R\sin\theta_f\,d\theta_f \qquad (4)$$

Substituting Eq. (3) in Eq. (4),

$$E = \pi R^3\sigma\int_0^{\Theta}[\alpha\sin^3\theta_f + 2(\alpha - 1)\sin\theta_f\cos^2\theta_f\ln(\cos\theta_f)]\,d\theta_f \qquad (5)$$

Integrating from 0 to Θ we get

$$E = \frac{2}{9}\pi R^3\sigma\left[(1 + 2\alpha) - \frac{9}{2}\alpha\cos\Theta + \left(\frac{5}{2}\alpha - 1\right)\cos^3\Theta + 3(1 - \alpha)\cos^3\Theta\ln\cos\Theta\right]$$

It is useful at this point to divide the force by $\pi R^2\sigma$ and the energy by $\pi R^3\sigma$, which yields dimensionless forms of the energy $\bar{E}$ and the force $\bar{F}$. These dimensionless quantities can be plotted against Θ to provide simple design curves utilized in the calculation of requirements for specific payload and velocity conditions (Figs. 41, 42). As shown in Fig. 43, the crushing stroke is given by the equation

$$S = R(1 - \cos\Theta) \qquad (6)$$

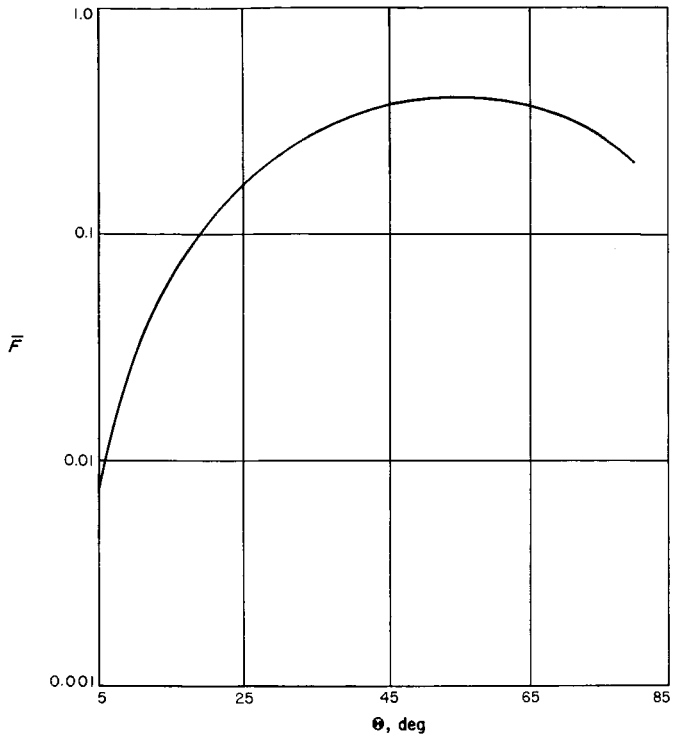

Fig. 41. Nondimensional force vs final angle

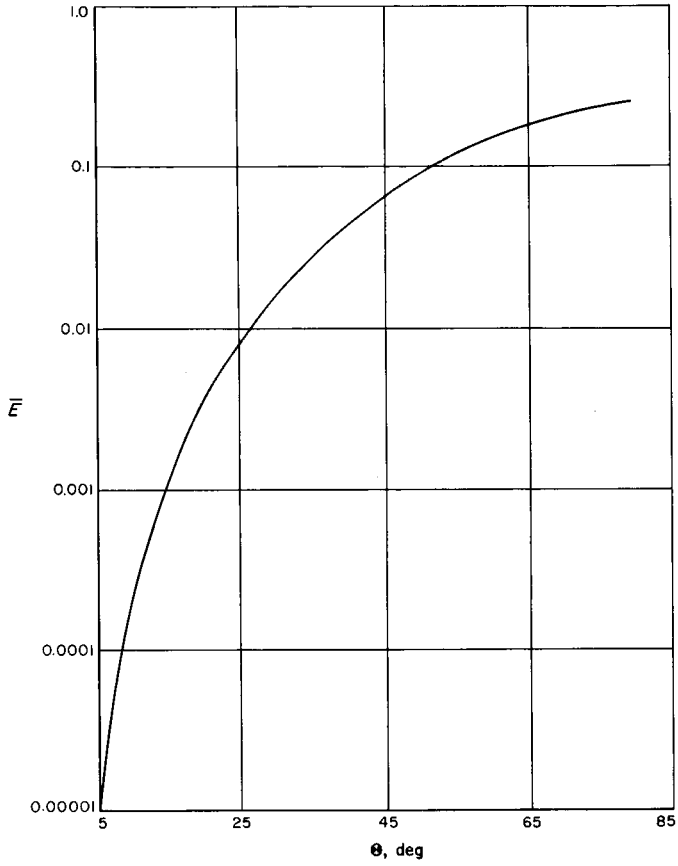

Fig. 42. Nondimensional energy vs final angle

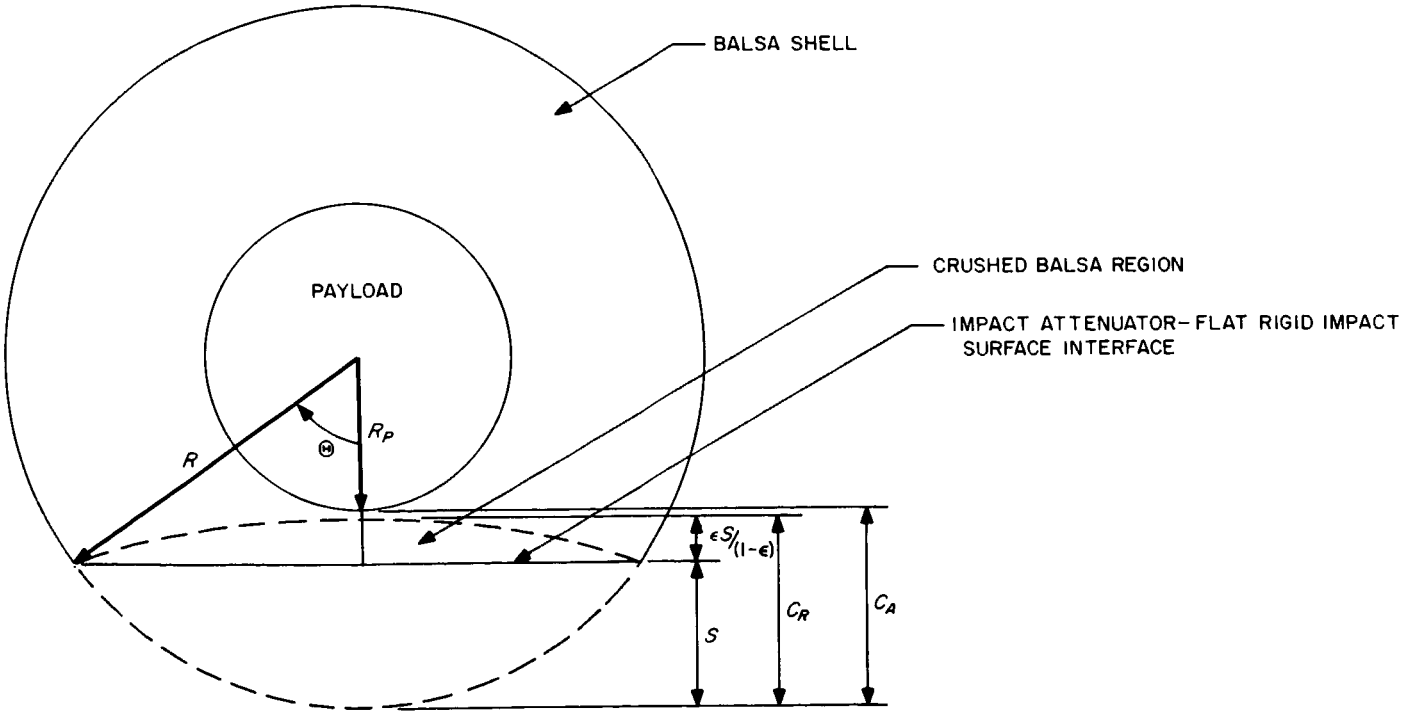

Fig. 43. Configuration at cessation of crushing

The required clearance is given by

$$C_R = \frac{S}{1-\varepsilon} = (1.25)\,S \quad \text{without rock present} \tag{7}$$

or

$$C_R = \frac{S+D}{1-\varepsilon} = (1.25)\,(S+D) \quad \text{with rock (diameter} = D)$$

The available clearance is

$$C_A = R - R_P \tag{8}$$

Impact experiments performed on balsa spheres by Aeronutronic have shown that unless the surface of the sphere is constrained by some type of cover, the sphere tends to break up during impact. The need for such a cover can also be demonstrated analytically.

Summing the forces on the incremental element in the horizontal direction yields the equation

$$dF_H = 2\pi r^2\sigma\,(1-\alpha)\sin^2\theta\,d\theta \tag{9}$$

Substituting $r = R\,(\cos\theta_f/\cos\theta)$ in Eq. (9) gives

$$dF_H = 2\pi R^2\sigma\,(1-\alpha)\cos^2\theta_f\,(\tan^2\theta)\,d\theta$$

integrating from 0 to θ_f yields

$$F_H = 2\pi R^2\sigma\,(1-\alpha)\,(\sin\theta_f\cos\theta_f - \theta_f\cos^2\theta_f) \tag{10}$$

The equations derived in this section can now be used in the iterative procedure to determine the lander dimensions and weights.

B. Iterative Procedure

If a specified payload is given (i.e., weight, radius, and impact velocity), the following procedure will determine the outer radius of the balsa to within 0.1 in. Three or four iterations will usually result in the stated accuracy.

1. Estimate the total radius.
2. Determine the weight and mass of the lander from the given payload geometry and the estimated total radius.
3. With the velocity and mass known, the kinetic energy may be determined from the equation: $KE = \frac{1}{2}mV^2$.
4. Determine the required nondimensional energy absorption capability by dividing the kinetic energy by the factor: $\pi R^3\sigma$.
5. Pick the appropriate angle Θ from the plot of the nondimensional energy vs Θ.
6. The stroke is determined by the equation: $S = R\,(1-\cos\Theta)$.
7. The required clearance C_R is given by the equation: $C_R = (1.25)\,S$ without rock; $C_R = (1.25)\,(S+D)$ with rock.
8. The available clearance C_A is equal to the difference between the payload radius and the total radius.
9. If the required clearance is greater than the available clearance, then increase the estimated total radius by the difference between the required and available clearances and repeat the procedure. If the required clearance is less than the available clearance, decrease the estimate by the difference and repeat the procedure.

   If $C_R - C_A \lessgtr 0$

   then $R' = R \mp |C_R - C_A|$

   R' = new estimate for radius.
10. After completing the iterations, enter the nondimensional force vs angle chart. With the known angle Θ, find the appropriate value of $\overline{F}$.

Table 7. Results of attenuator design for model in Fig. 44 and payloads in Fig. 45 (ρ_B = 7 lb/ft²; α = 0.1115; σ = 1013 psi)

Shape	Rock	V, ft/sec	R_p, in.	R, in.	Weight, lb	KE, ft-lb	Θ	S, in.	C_R, in.	n, g
Lenticular	No	150	25	29	198.76	69,497	27°3′	3.169	3.961	2512
Lenticular	Yes	150	25	34.5	303.92	106,269	26°18′	3.571	9.464	2218
Lenticular	Yes	200	25	36.5	359.97	223,223	30°48′	5.148	11.435	2692
Spherical	No	150	12	17.9	228.01	79,725	42°15′	4.65	5.813	1535
Spherical	Yes	150	12	23.1	339.84	118,834	37°54′	4.872	11.09	1520
Spherical	Yes	200	12	26.0	428.93	266,000	43°24′	7.109	13.887	1617

11. The g level is given by the equation:

$$n = \frac{\overline{F} \cdot \pi R^2 \sigma}{W}$$

Most covers can be accounted for by simply including the weight as part of the payload; however, if the thickness and weight of the cover becomes large, this may not hold because of the effect of the added weight on the payload density. It is also possible that the mechanism of crushing may be affected.

The above procedure is adaptable with simple modifications to other design procedures (i.e., determination of required parameters for a given total landed weight, payload radius, and impact velocity).

Section X considers several different payload configurations adaptable to the balsa attenuator approach. A landed payload weight of 160 lb is considered here and some results for this payload are given in Table 7. The balsa characteristics were taken from Ref. 12.

One case which is of particular interest is double-impact. Impact on a 30-deg slope with a 4-in rock resting on it is considered first. The second impact is assumed to occur on a 60-deg slope. The attenuator is assumed to carry the rock with it after the first impact. The second hit occurs on the same attenuator surface position as the first. Each impact is assumed to eliminate the component of velocity normal to the impacted surface. The results of this example show that it is only necessary to consider the impact on a flat surface which is perpendicular to the velocity vector with the 4-in. rock present. The payload velocity components considered here are 130 ft/sec directed along the local vertical and 100 ft/sec parallel to a 30-deg ground slope. This latter velocity results from the assumption that the payload picks up the wind velocity while still attached to the terminal decelerator (see Fig. 44).

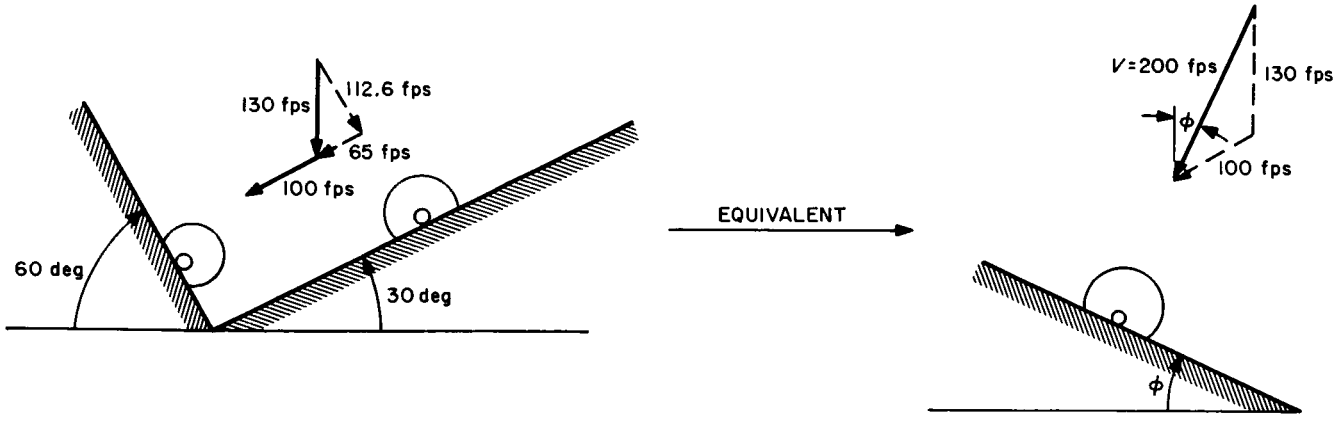

Fig. 44. Surface model and equivalent impact surface model

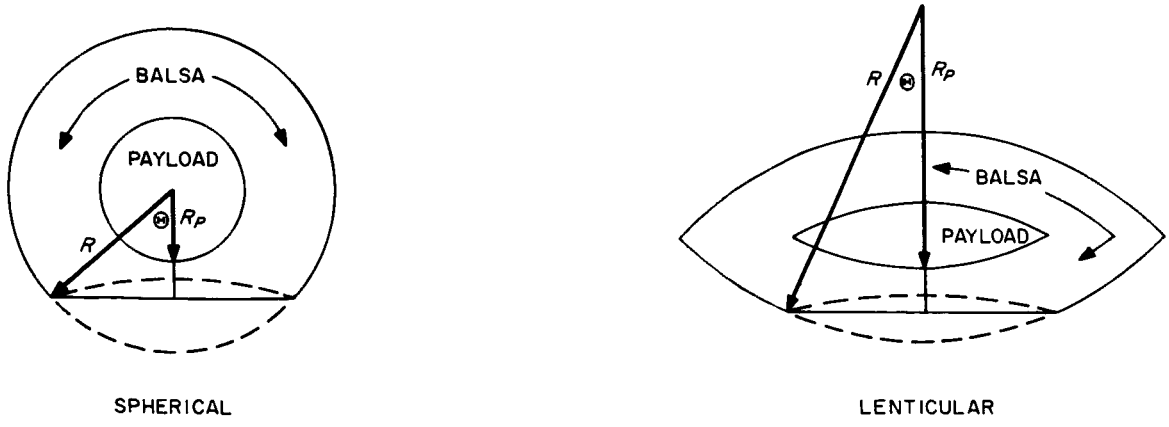

Fig. 45. Shapes for example calculations

C. Limiting Velocity Condition at Which No Useful Payload Exists

The maximum velocity which will admit the landing of a point payload (no weight, radius = 0), can be determined as a function of the balsa wood density by equating the energy dissipated to the kinetic energy of the lander (Fig. 46).

$$E = KE$$

$$\overline{E} \cdot \pi R^3 \sigma = 1/2 m V^2$$

For a spherical shape, we get:

$$\frac{\left(\frac{3g\sigma\overline{E}}{2V^2}\right) - \rho_B}{\rho_P - \rho_B} = \left(\frac{R_P}{R}\right)^3$$

For a point payload $R_p = 0$. Therefore

$$\overline{E} = \frac{2V^2\rho_B}{3g\sigma}$$

From Eq. (5) we see that

$$\frac{2V^2\rho_B}{3g\sigma} = \frac{2}{9}\left[(1+2\alpha) - \frac{9}{2}\alpha\cos\Theta + \left(\frac{5}{2}\alpha - 1\right)\cos^3\Theta + 3(1-\alpha)\cos^3\Theta\ln(\cos\Theta)\right] \quad (11)$$

From the geometry of a sphere, we can see that for impact on a flat surface (no rock), the equation for the limiting angle Θ is:

$$\Theta = \cos^{-1}\left\{\frac{4R_P + R}{5R}\right\}$$

For a point payload, $R_p = 0$ and $\Theta = \cos^1(0.2) \cong 78°28'$. Substituting this value into Eq. (11) and rearranging yields:

$$V^2 = \frac{g\sigma}{3\rho_B}[0.95737 + \alpha(1.1586)]$$

Reference 11 indicates that

$$\frac{\sigma}{\rho_B} = \frac{\eta}{1-\varepsilon} = (1.25)\eta$$

and that the equation for η based on an extensive test program is

$$\eta = 15{,}600 + 360\rho_B$$

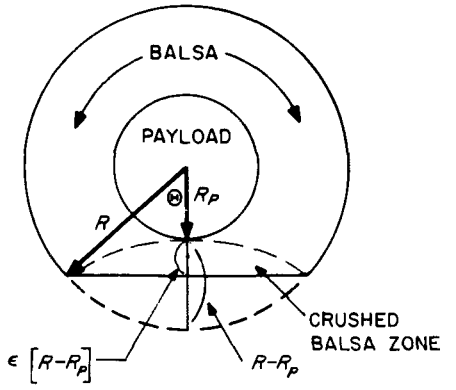

Fig. 46. Assumed lander configuration at cessation of crushing

We now have

$$V^2 = \frac{(1.25)g\eta}{3}[0.95737 + \alpha(1.1586)] \quad (12)$$

This equation results in the following critical velocity curve (Fig. 47) for balsa wood densities ranging from 5 lb/ft² to 12.5 lb/ft³. Velocities below those indicated on the curve for a specified balsa wood density will yield real payloads.

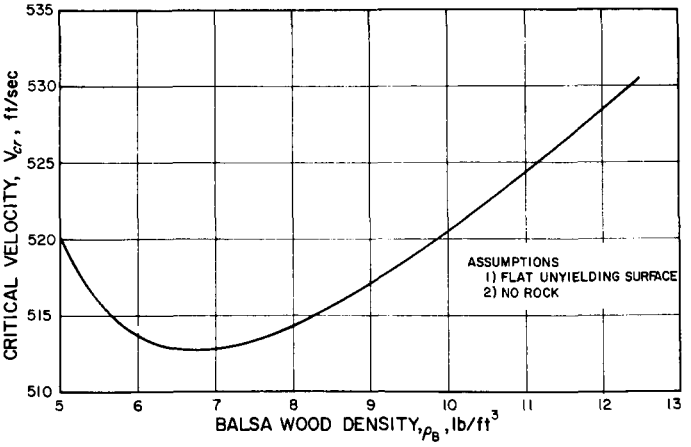

Fig. 47. Critical velocity at which real payloads can no longer be achieved

D. Determination of Payload Weight Fraction as a Function of Velocity

For velocities below those indicated on the critical velocity curve (Fig. 47), there is a simplified technique given in Fig. 48 for determining what portion of a given landed weight can be payload and how much weight

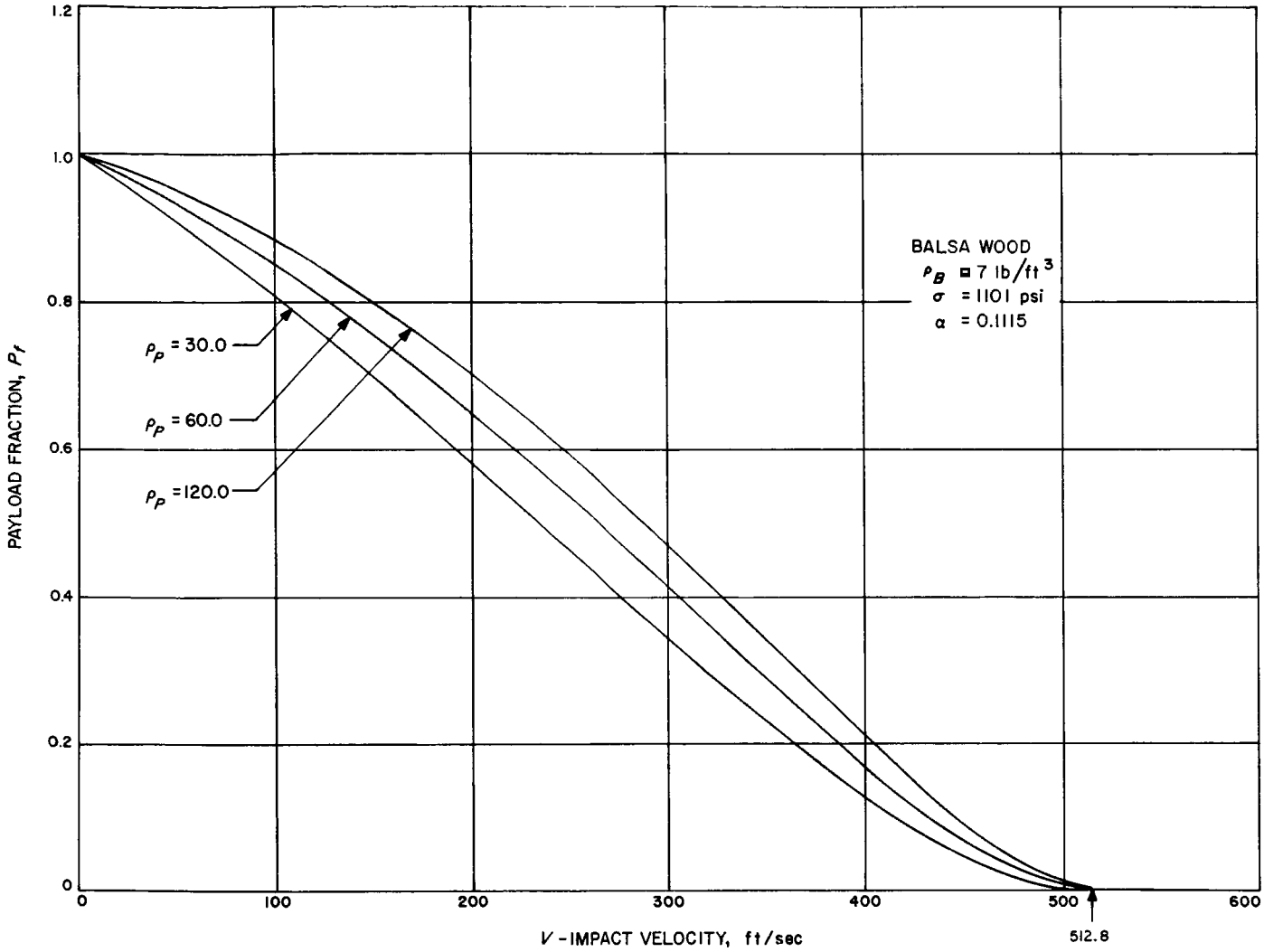

Fig. 48. Payload weight fraction vs impact velocity

must be balsa wood. As in the determination of the critical velocity, we must assume a rigid, flat impact surface with no rock.

The payload fraction is defined as the weight of the payload divided by the total weight of the lander.

$$P_f = \frac{W_P}{W_t}$$

Writing this in terms of the payload radius and total lander radius yields:

$$P_f = \frac{\rho_P}{(\rho_P - \rho_B) + \left(\frac{R}{R_P}\right)^3 \rho_B}$$

Rearranging, we get:

$$\left(\frac{R_P}{R}\right)^3 = \frac{\rho_B P_f}{\rho_P - (\rho_P - \rho_B) P_f}$$

Equating the energy dissipated to the kinetic energy of the lander gives

$$E = KE$$

or

$$\bar{E} \cdot \pi R^3 \sigma = \frac{1}{2} m V^2 = \frac{1}{2}\left(\frac{4}{3}\pi R^3\right)\left[\left(\frac{R_P}{R}\right)^3 (\rho_P - \rho_B) + \rho_B\right]\frac{V^2}{g}$$

Rearranging yields:

$$\bar{E} = \frac{2V^2}{3g\sigma}\left[\left(\frac{R_P}{R}\right)^3 (\rho_P - \rho_B) + \rho_B\right]$$

Rewriting the radius ratio as a function of the payload fraction gives:

$$\bar{E} = \frac{2V^2}{3g\sigma}\left[\frac{\rho_P\rho_B}{\rho_P - (\rho_P - \rho_B)P_f}\right]$$

Recalling that

$$\bar{E} = \frac{2}{9}\left[(1 + 2\alpha) - \frac{9}{2}\alpha\cos\Theta - \left(\frac{5}{2}\alpha - 1\right)\cos^3\Theta + 3(1 - \alpha)\cos^3\Theta\ln\cos\Theta\right]$$

and that

$$\cos\Theta = \frac{4R_P + R}{5R} = \frac{4}{5}\left(\frac{R_P}{R}\right) + \frac{1}{5}$$

Rewriting the cos Θ as a function of the payload fraction

$$\cos\Theta = \frac{4}{5}\left[\frac{\rho_B P_f}{\rho_P - (\rho_P - \rho_B)P_f}\right]^{1/3} + \frac{1}{5}$$

Substituting for cos Θ in the equation for $\bar{E}$ yields the following velocity–payload fraction relationship for given densities of payload and balsa wood

$$V = \left\{\frac{g\sigma[\rho_P - (\rho_P - \rho_B)P_f]}{3\rho_P\rho_B}\right\}\left((1 + 2\alpha) - \frac{9}{2}\alpha \times \left\{\frac{4}{5}\left[\frac{\rho_B P_f}{\rho_P - (\rho_P - \rho_B)P_f}\right]^{1/3} + \frac{1}{5}\right\} + \left(\frac{5}{2}\alpha - 1\right)\left\{\frac{4}{5}\left[\frac{\rho_P P_f}{\rho_P - (\rho_P - \rho_B)P_f}\right]^{1/3} + \frac{1}{5}\right\}^3 + 3(1 - \alpha)\left\{\frac{4}{5}\left[\frac{\rho_P P_f}{\rho_P - (\rho_P - \rho_B)P_f}\right]^{1/3} + \frac{1}{5}\right\}^3 \times \ln\left\{\frac{4}{5}\left[\frac{\rho_B P_f}{\rho_P - (\rho_P - \rho_B)P_f}\right]^{1/3} + \frac{1}{5}\right\}\right)$$

This equation results in the following velocity–payload fraction curve which provides a quick determination of weight proportions for a given landed weight and a given impact velocity on a rigid, flat impact surface with no rock.

E. Attenuator Weights for Specific Landing Modes Studied

A ballistic landing mode is considered in Section XII in which the weight breakdown is summarized. The ballistic mode results in a vertical velocity of 505 ft/sec and a 30-deg downslope velocity of 100 ft/sec or a resultant velocity of approximately 561 ft/sec. It can be seen from the critical velocity curve that for the given range of balsa wood densities no real payload exists.

Two-stage parachute landing modes are also considered in this section. These modes yield a vertical velocity of 130 ft/sec and a 30-deg downslope velocity of 100 ft/sec. The tabulation gives the weight available for the landed payload system.

Table 8 gives several examples of the required parameters for specified landed weights with and without a rock present. The results are also presented for the case of zero downslope velocity.

Table 8. Examples of required parameters for specified landed weights with and without a rock present (Cover weight = 21 lb; payload radius = 12 in; ρ_B = 7 lb/ft^3; α = 0.1115; σ = 1101 psi)

Weight, lb	Velocity, ft/sec	Presence of 4-in. rock	W_P, lb	W_B, lb	R, in.	Deceleration n, g
363	200	Yes	106.21	235.79	25.0	2031
363	200	No	211.47	130.53	21.12	1696
363	130	Yes	183.16	158.84	22.3	1341
363	130	No	270.53	71.47	18.11	1097
403	200	Yes	133.25	248.75	25.4	1922
403	200	No	240.32	141.68	21.6	1598
403	130	Yes	215.47	166.53	22.6	1271
403	130	No	303.88	78.12	18.5	1049
559	200	Yes	240.71	297.29	26.8	1778
559	200	No	358.17	179.83	23.1	1321
559	130	Yes	347.12	190.88	23.5	1070
559	130	No	441.5	96.5	19.5	918

NOMENCLATURE
(Section IX)

a acceleration

C_A clearance available

C_R clearance required to prevent crushed balsa region from penetrating into or damaging payload

E energy dissipated during mechanical crushing

$\bar{E}$ nondimensional energy dissipation

$\bar{F}$ nondimensional vertical force

F_H horizontal force

F_v vertical force

m total mass of lander

n maximum acceleration of lander during crushing, Earth g

r distance from center of sphere to any point on interface between attenuator and impact surface

R total radius of attenuator

R_p radius of payload

S crushing stroke

V impact velocity

W_B weight of balsa wood

W_P weight of payload

W_T total weight of landed payload system

α ratio of crushing strength perpendicular to the grain

ε ratio of crushed length to uncrushed length = 0.2

η specific energy of balsa wood

θ half-cone angle at any point on attenuator–impact surface interface

θ_f total half-cone angle defining attenuator–impact surface interface

Θ total half-cone angle defining attenuator–impact surface interface at cessation of crushing

ρ_B balsa wood weight density

ρ_P payload weight density

σ crushing strength of balsa wood parallel to the grain

X. LANDED PAYLOAD–THERMAL CONTROL ON THE MARTIAN SURFACE

The thermal control of a survival capsule on the surface of Mars is complicated by the wide range of conditions that might be encountered: surface atmospheric temperature of 360 to 540°R, atmospheric velocity at the surface of 0 to 300 ft/sec, surface properties ranging from black to reflective, and a sky which may be clear, cloudy, or dusty with corresponding unknown sky temperatures.

Generally, the surface and air temperatures are below the desired operating levels of the electronics and batteries flown presently, especially when averaged over the Martian day. The solar radiation illuminating the capsule will heat its surface into or above the operating tolerance, dependent upon surface properties, wind, and solar intensity.

The temperature histories of two spherical capsules, one black and the other polished aluminum, on the Martian surface were studied to determine the influence of the parameters of the Mars model (Table 9). The extremes of temperatures for certain cases are listed in Table 10.

The uncertainty in the atmospheric temperature and velocity has a profound effect on the temperature history of the capsule on the surface. If a 300-ft/sec wind is blowing, the capsule will reach steady-state temperatures within either the 12-hr day or the night periods, regardless of surface finish. For a still atmosphere, the capsule temperatures do not reach equilibrium at night, since the heat losses are primarily radiation, with the polished capsule responding slower.

The black capsule reaches steady state with ease in the 12-hr day or night during a 300-ft/sec wind. In still air, the black capsule reaches equilibrium during the daylight hours, but at sunrise it is still 20°R away from night equilibrium temperatures. The effect of the Mars wind is shown by a comparison of the black capsule temperatures under still and windy conditions. With the atmosphere temperature a constant 540°R, stilling the breeze raises the day maximum temperature 40°R and lowers the night minimum 100°R, since the atmosphere provides less heating and cooling. If the night temperature is reduced to 360°R, the night minimum temperature drops 160°R for the windy case and 90°R for the still atmosphere case.

The main effect of polishing the capsule surface is to reduce the temperature excursion extremes since radiation and solar irradiation heat fluxes are reduced. Under 300-ft/sec wind conditions, the temperature excursion is reduced by 20 to 50°R, while in still air the comparison is more striking with reductions of 100 to 130°R. The capsule temperatures in the wind reach steady state within the day and night periods but are still transient at sunrise and sunset if there is no wind.

The preferred capsule surface treatment is probably a grey with low absorptance and emittance to give the proper temperature level with small excursions. The capsule interior would be thermally isolated from the shell to reduce the influence of the surface temperature excursions. Isolation of the interior from the shell is in conflict with the requirements of high-g impact survival. Structural members with insulation properties, radiation shielding, and polished interior surfaces are probably required. The retention of the impact-absorbing material might be desirable for its insulating capability, which could reduce the insulating constraint on the structure.

Table 9. Mars model

Atmosphere	14-mb pressure 360- to 540-deg temperature 0 or 300 fps wind 0°R sky temperature
Solar radiation S	230 or 138 Btu/hr ft^2
Mars surface	0.9 or 0.3 solar absorptance 607 or 460°R day temperature (S = 230) 535 or 405°R day temperature (S = 138) 459°R night temperature when atmosphere equals 540°R 300°R night temperature when atmosphere equals 360°R
Sphere model	2-ft diameter 100 lb C_p = 0.2 Btu/lb °R Isothermal α = 0.9, ε = 0.9 black α = 0.2, ε = 0.005 polished Raised off the surface

Table 10. Maximum and minimum temperatures seen by a capsule on Mars (Power duty cycle: 37 watts for 2 hr; 3 watts for 22 hr; 300-ft/sec wind)

Atmosphere temperature, °R		S, Btu/hr ft^2	Mars surface	Wind, ft/sec	Survival sphere	Maximum day temperature, °R	Minimum night temperature, °R	ΔT, °R
Day	Night							
540	540	230	Black	300	Black	570	510	60
540	540	230	Black	0	Black	610	410	200
540	540	230	Black	300	Polished	550	540	10
540	540	230	Black	0	Polished	650	550	100
540	540	230	Black	300	Black	570	350	220
540	360	230	Black	0	Black	610	320	290
540	360	230	Black	300	Polished	550	360	190
540	360	230	Black	0	Polished	600	440	160
540	540	230	White	300	Black	570	510	60
540	540	230	White	300	Polished	555	540	15
540	540	138	Black	300	Black	555	510	15
540	540	138	Black	300	Polished	550	540	10

XI. LANDED PAYLOAD OPERATIONS AND CONFIGURATION

The primary objective of this part of the study was to determine the electromechanical post-landing operations necessary on the surface of Mars to accomplish a possible engineering and scientific mission. Since these operations are inseparable from impact considerations and lander configuration, the determination of post-landing requirements will be developed by study of several general configurations consistent with mission objectives. The various configurations fall into one of two classifications:

1. Short-life landers with 10 to 50 lb of scientific instruments. These configurations are applicable to both ballistic and terminal decelerator landing modes and assume omnidirectional landing capability with varying degrees of reorientation after impact.
2. Long-term landers with 50 to 125 lb of scientific instruments. No configurations were developed to specific mission requirements, but a number of considerations will be discussed.

A. Short-Life Landers: 10 to 50 lb of Scientific Payload

This classification of payload is considered most likely for the first Mars missions and is considered generally applicable for high-velocity impact conditions and decelerated impacts where the landing conditions are unknown. Proposed payloads are generally of a spherical shape at the center of a spherical impact limiter of crushable material (i.e., balsa wood). Development knowledge along this line is more advanced because of work done on the *Ranger* lunar landing system and a number of development studies. In addition to developing different ways of adapting the spherical payload in a spherical impact limiter to possible mission objectives, a configuration adopting lenticular payload to an impact limiter is considered. For all short-life landers, a nondeployable power source (i.e., batteries) was assumed.

The mission objective for this payload study was to provide direct-link communication capability with Earth and to support up to 50 lb of science instrumentation. Subsystem weights as estimated for configuration development are presented in Table 11.

1. Approach A: Minimum Mission Approach

This configuration was developed primarily as a basis for evaluation of other approaches. It is the most passive of the configurations that were considered. As shown in Fig. 49, the approach consists of a spherical payload with 6 antennas. Each antenna would have one degree of freedom (± 45 deg) to provide communication from whatever orientation the payload landed. Atmospheric exposure would be provided by manifolded flexible tubes through the impact limiter at regular intervals to assure that several such tubes would have access to the atmosphere. It is not proposed that this configuration be considered for more elaborate missions than represented by Science Increment No. 1 (ref. Table 11).

In summary, the required electromechanical operations associated with this configuration are:

1. Retraction of electrical umbilical prior to landing.
2. Selection of antenna. This would be provided by ground command actuation of a stepping mechanism to select the antenna location best suited for the payload orientation. This is the only configuration studied that required a ground command capability.
3. Selection of one of several sections of sampling tubes to assure sample is taken from "up" direction. This would be done by g-switch sensing.

Special problems inherent in this configuration are:

1. Difficulty of developing a gimballed antenna for high-velocity impact.
2. Difficulty of developing an envelope for high-velocity-impact packaging due to multiple antennas.
3. Severe limitation of mission capability.
4. Requirement for ground command capability.

2. Approach B: "Floated" Payload

This is an approach developed for the *Ranger* Block II lunar seismometer mission and studied extensively for application to a lunar and Mars facsimile TV mission (Ref. 11). The description contained here and shown in Fig. 50 is a possible adaptation to more general mission requirements. Basically the concept consists of a sphere within a sphere. The inner sphere, containing the payload, is suspended with respect to the outer sphere by a flotation fluid and, therefore, orients to the local vertical after impact. The inner sphere is "caged" to the outer sphere by the umbilical electrical connection until lander

Table 11. Estimated subsystem weights and electrical packaging volume for short-life Mars lander (impact limiter not included)

Subsystem nomenclature	Approach A		Approach B		Approach C		Approach D		Approach E	
	Wt., lb	Vol., in.^{3}	Wt., lb	Vol., in.^{3}	Wt., lb	Vol., in.^{3}	Wt., lb	Vol., in.^{3}	Wt., lb	Vol., in.^{3}
1. Power supply (battery)	15	160	15	160	15	160	15	160	15	160
2. Power conditioning	3.3	66	3.3	66	3.3	66	3.3	66	3.3	66
3. Radio subsystem	9.0	180	9.0	180	9.0	180	9.0	180	9.0	180
4. Antenna and selector	3.5	—	0.5	—	2.3	—	0.5	—	1.0	—
5. Command	1.5	30	1.5	30	1.5	30	1.5	30	1.5	30
6. Capsule timer and sequencer	1.3	30	1.3	30	1.3	30	1.3	30	1.3	30
7. Integrated data system and storage	8.0	160	8.0	160	8.0	160	8.0	160	8.0	160
8. Extension and/or orientation mechanization	3.0	—	14.0	—	23.0	—	18.0	—	28.0	—
9. Structure and cabling	25.0	—	25.0	—	25.0	—	35.0	—	25.0	—
10. Temperature control	6.0	—	6.0	—	8.0	—	6.0	—	6.0	—
11. Impact limiter removal	—	—	—	—	3.0	—	—	—	3.0	—
Sub-total	75.6		83.6		99.4		97.6		101.1	
12. Science increment No. 1	8.0	277	8.0	277	13.0	346	10.0	346	10.0	346
a. Gas chromatograph	*		*		*		*		*	
b. Water vapor detect					*		*		*	
c. Atmospheric pressure	*		*		*		*		*	
d. Atmospheric temperature					*		*		*	
Sub-total	83.6		91.6		112.4		107.6		111.1	
13. Science increment No. 2	—	—	30.0	242	8.0	173	10.0	138	10.0	138
a. Impact limiter removal and stabilization			*							
b. Ultraviolet flux			*		*		*		*	
c. Soil gas analysis					*		*		*	
d. Water vapor detect			*							
e. Atmospheric temperature			*							
Sub-total			121.6		120.4		117.6		121.1	
14. Science increment No. 3	—	—	—	—	30.0	693	20.0	693	20.0	693
a. Soil sampling					*		*		*	
b. Organic gas					*		*		*	
c. C-N-O-H-S ratios					*		*		*	
d. "Growth"					*		*		*	
Sub-total					150.4		137.6		141.1	

*Experiment and required added engineering subsystems included in weight estimates.

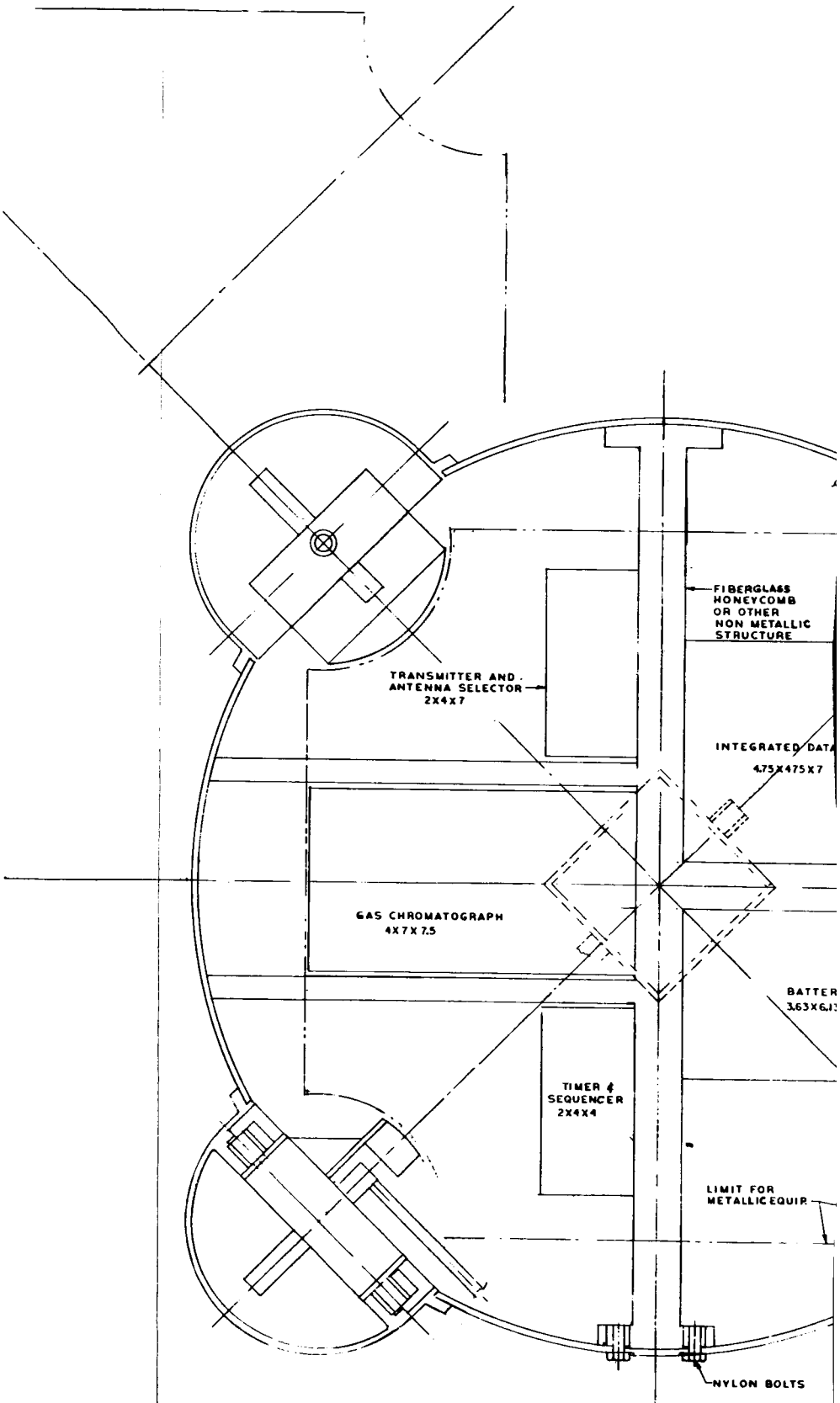
FIBERGLASS
HONEYCOMB
OR OTHER
NON METALLIC
STRUCTURE
TRANSMITTER AND
ANTENNA SELECTOR
2X4X7
INTEGRATED DATA
4.75X475X7
GAS CHROMATOGRAPH
4X7X7.5
BATTER
3.63X6.1
TIMER &
SEQUENCER
2X4X4
LIMIT FOR
METALLIC EQUIP
NYLON BOLTS

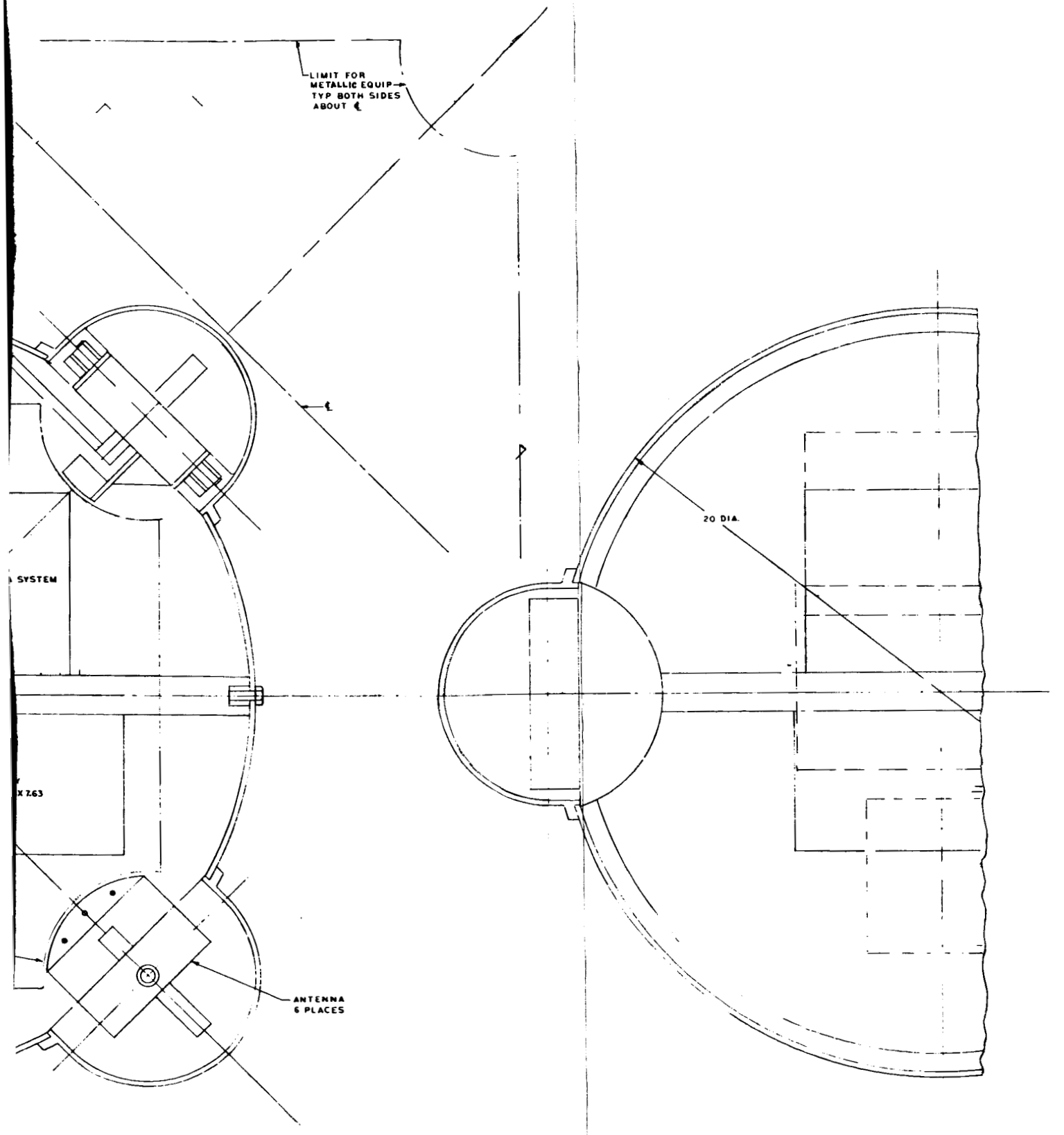

Fig. 49. Minimum mission lander configuration

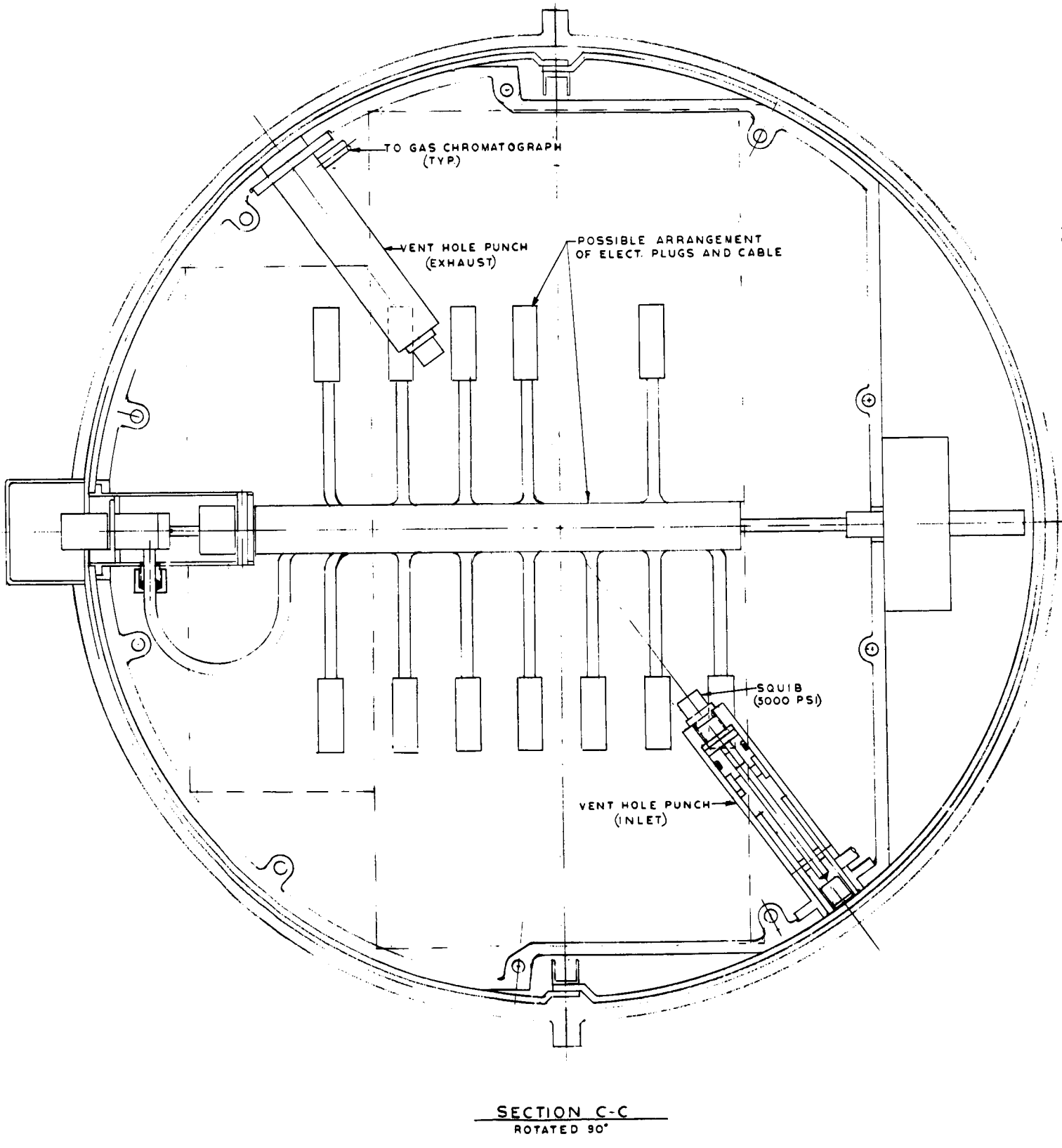

Fig. 50. "Floated" lander configuration

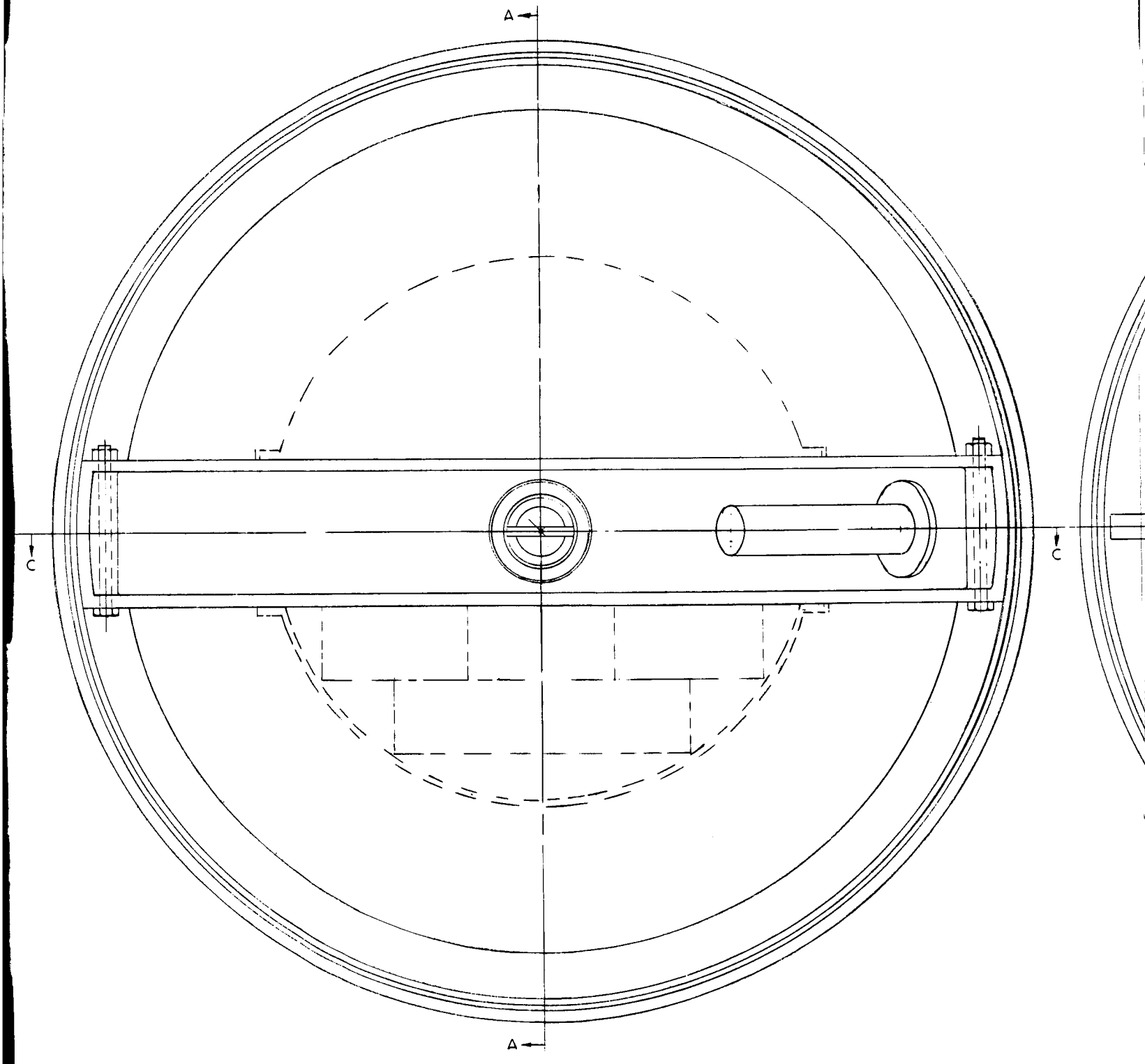

SECTION B-B

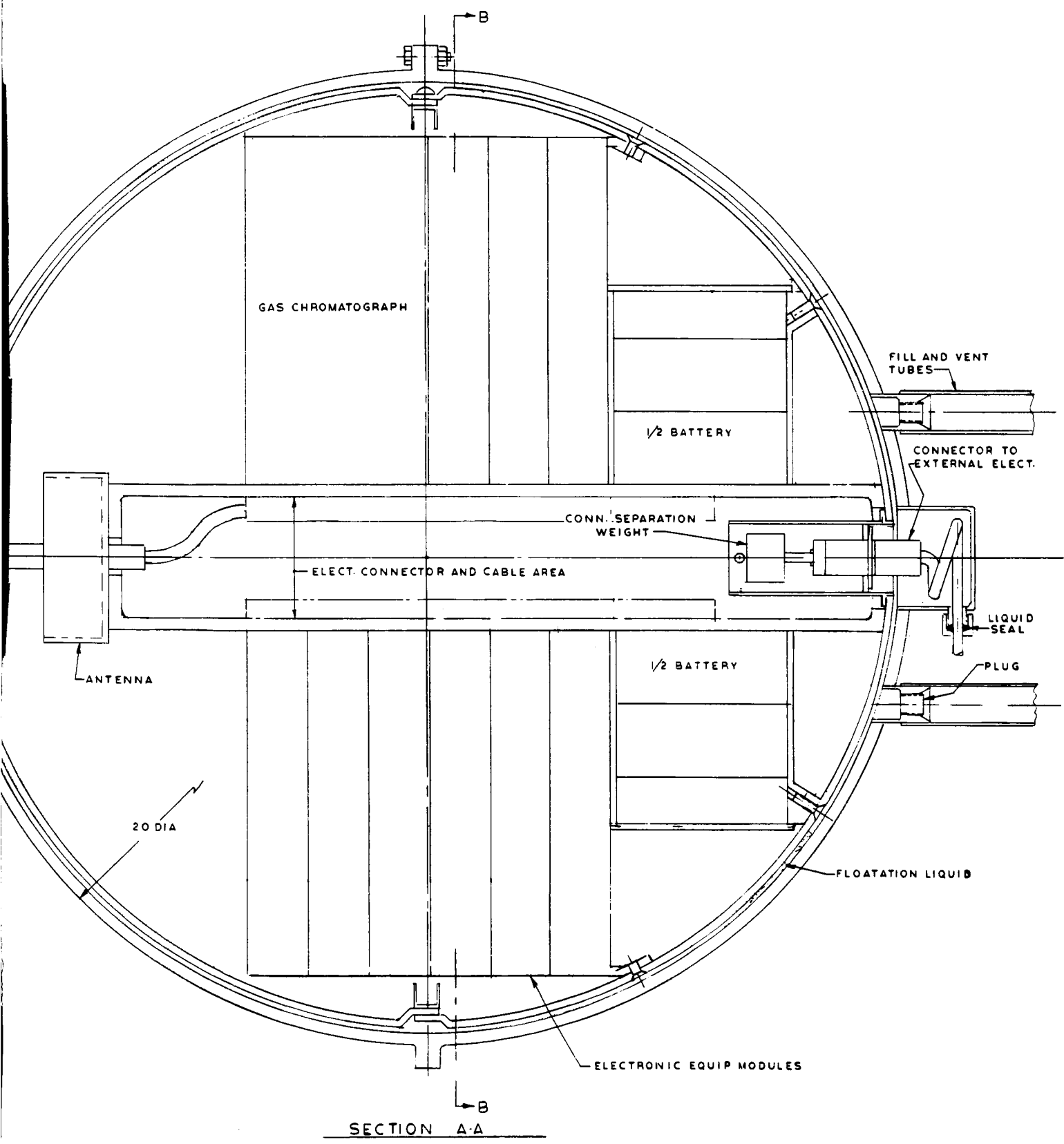
B
GAS CHROMATOGRAPH
1/2 BATTERY
FILL AND VENT TUBES
CONNECTOR TO EXTERNAL ELECT.
CONN. SEPARATION WEIGHT
ELECT. CONNECTOR AND CABLE AREA
LIQUID SEAL
ANTENNA
1/2 BATTERY
PLUG
20 DIA
FLOATATION LIQUID
ELECTRONIC EQUIP MODULES
B

SECTION A-A

separation from the entry body. Recaging and impact limiter penetration (porting) after erection to the local vertical are accomplished by deployment of the atmospheric sampler and exhaust tubes shown in Fig. 50 (for gas chromatograph). The exhaust tube deployment could also provide draining of the flotation fluid if required. For the science instrumentation anticipated for Science Increment No. 1 (Table 11), this would be the extent of active operations necessary to establish communications by activating the transponder and other electronic subsystems from the lander sequencer and timer. The engineering subsystems and science electronics are packaged into standard modules and attached to the central structure and harness support as shown in Fig. 50.

The next experiments (Science Increment No. 2, Table 11) recommended for consideration require direct access to the Mars environment. Such experiments would be ultraviolet flux, wind measurement, water vapor detection and temperature measurement. These experiments require more complex deployment mechanisms and result in weight increases for extension mechanisms and to maintain stability. It is assumed that impact limiter removal is necessary to provide the required access.

The last listed experiments (Science Increment No. 3) require sampling of the Mars surface. A preliminary judgment is that this configuration is not adaptable to experiments more complex than those indicated in Table 11 for Science Increments Nos. 1 and 2. The requirement for science deployment from an internal sphere (initially fluid-tight) becomes a severe penalty for the more complex sampling devices.

In summary, the required electromechanical operations for a floated sphere are:

1. Retracting electrical umbilical (uncaging) prior to landing.
2. Removing impact limiter (for scientific experimentation other than atmospheric analysis).
3. Deploying stabilizers to maintain position during sensor deployment.
4. Caging and draining of flotation fluid after landing. This operation also provides inlet and exhaust for atmospheric analysis.
5. Deploying sensor probe if required (UV, wind instrumentation).

Specific areas representing special development problems are:

1. Requirement for an electrical connection from the outside to the floated payload prior to separation from the spacecraft.
2. Need for stability during caging operation so that payload orientation is maintained. A toroidal gas bag, as elaborated later, might be a reasonable method of obtaining a satisfactory stable orientation.
3. Taking a noncontaminated atmospheric sample from a floated sphere encased in an impact limiter. This problem becomes more severe as the impact limiter thickness increases.
4. Impact limiter removal and sensor deployment if required.

3. Approach C: Extendable-Leg Configuration

This is an approach which has been investigated for a lunar TV mission (Ref. 13). Figure 51 shows an adaptation of this principle to the Mars landed payload. Conceptually, the payload is a sphere with four extendable legs forming the axes of a tetrahedron. After impact, the impact limiter must be removed, allowing the legs to extend. The payload will rest on a plane established by three legs with the fourth leg 90 deg to the support plane. Each leg has a combination foot/antenna/sensor head. For sensing and communication, the instrument pad 90 deg to the Mars surface would be selected by a g switch or other sensing device. Because of direct exposure of the sensor dome to the Mars atmosphere, it would be possible to perform experiments presently considered for Science Increments Nos. 1 and 2. Depending on the mechanization, it is also possible to perform soil sampling experiments by activating one of the sensor domes in contact with the Mars surface. Complete duplication of antennas and atmospheric analysis instrumentation is required at four locations, with soil sampling instrumentation required at two locations. Although the configuration shows the sensor domes as protrusions from the surface of the spherical payload, the actual instrument and subsystem requirements may allow the domes to be recessed into the payload. This latter approach will permit the payload to conform to a spherical surface, and, thereby, provide a better impact limiter interface.

An interesting variation of this approach is a mechanization that provides selective orientation, thus eliminating duplication of antennas and science instrumentation associated with four possible orientations. This would

simplify the foot design since much of the science instrumentation could be body-mounted. The method proposed to obtain the selective orientation is the location of small thrusters on the support legs and pointed away from the antenna leg. The thruster on the leg in the "up" position would be activated, rotating the payload about the two support legs such that the antenna would be vertical to the support plane. The area of greatest uncertainty is the configuration of foot design which best meets the various orientation requirements under unknown conditions.

In summary, the required electromechanical operations associated with this configuration are:

1. Retraction of electrical umbilical prior to landing.
2. Impact limiter removal.
3. Leg/sensor dome extension.
4. Antenna/sensor selection (if required).
5. Thruster activation (if required).

Configuration-peculiar problems are:

1. Impact limiter removal.
2. Deployment of electrical and rf cable during leg extension.
3. Relatively long leg extension (30 in. or more for 20-in.-diameter sphere configuration shown) to provide support plane because of the geometry of leg location.
4. Foot geometry compatible with sensor and antenna requirements capable of lifting spacecraft during leg extension (approximately 8-in.-diameter bearing surface required).
5. Unless antenna gimballing is provided, the antenna will orient perpendicular to local terrain rather than local vertical.

4. Approach D: Semi-Selective Orientation Configuration (Lenticular Shape)

This approach is developed for contrast with the family of spherical payloads previously defined. The payload is elliptical in cross section. With such a shape, the final orientation of the payload will be resting along the major axis of the ellipse. A combination of ground slope and tilting due to surface obstacles up to 30 deg from the local vertical could be tolerated. As shown in Fig. 52, the basic electronic subsystems and batteries are integrated around a hexagon- or octagon-shaped internal structure similar to the *Ranger* and *Mariner C* concept. In the center cavity would be a two-degree-of-freedom gimballed platform mounting the antenna and scientific sensors requiring atmospheric exposure and orientation. After impact, the center cavity cover in the "up" position would be deployed, exposing the gimballed platform. This platform would be uncaged and oriented to local vertical and recaged. The antenna (plus any scientific instruments requiring Mars surface access) would be deployed, completing the electromechanical operations necessary to perform the mission. This configuration probably is not efficient for the 10- to 20-lb science instrumentation missions but has considerable growth potential.

The gimbal platform could be replaced by a sufficient duplication of science and antenna to provide an either-side-up capability to gross local terrain orientation.

In summary, the electromechanical operations required for a lenticular-shaped lander as described are:

1. Retraction of electrical umbilical prior to landing.
2. Deployment of center cavity cover by g switch sensing.
3. Uncaging of center platform for local vertical orientation and recaging.
4. Deployment of antenna and science sensors requiring ground access, etc.

Configuration-peculiar problems are:

1. The external geometry causes impact deceleration levels to be appreciably higher than for a spherical impact limiter. If crushable materials are used, this configuration would probably be applicable only for decelerated impact (parachute descent). If pneumatic impact limiters (a torus is a good shape for this particular payload) are feasible for Mars impact conditions, higher impact velocities without a severe penalty might be accepted.
2. Since only part of the payload orients after impact, there are limitations of acquiring local vertical without physical contact with the unoriented part of the payload. Since stops would be provided for one degree of freedom, this risk would be lessened, with

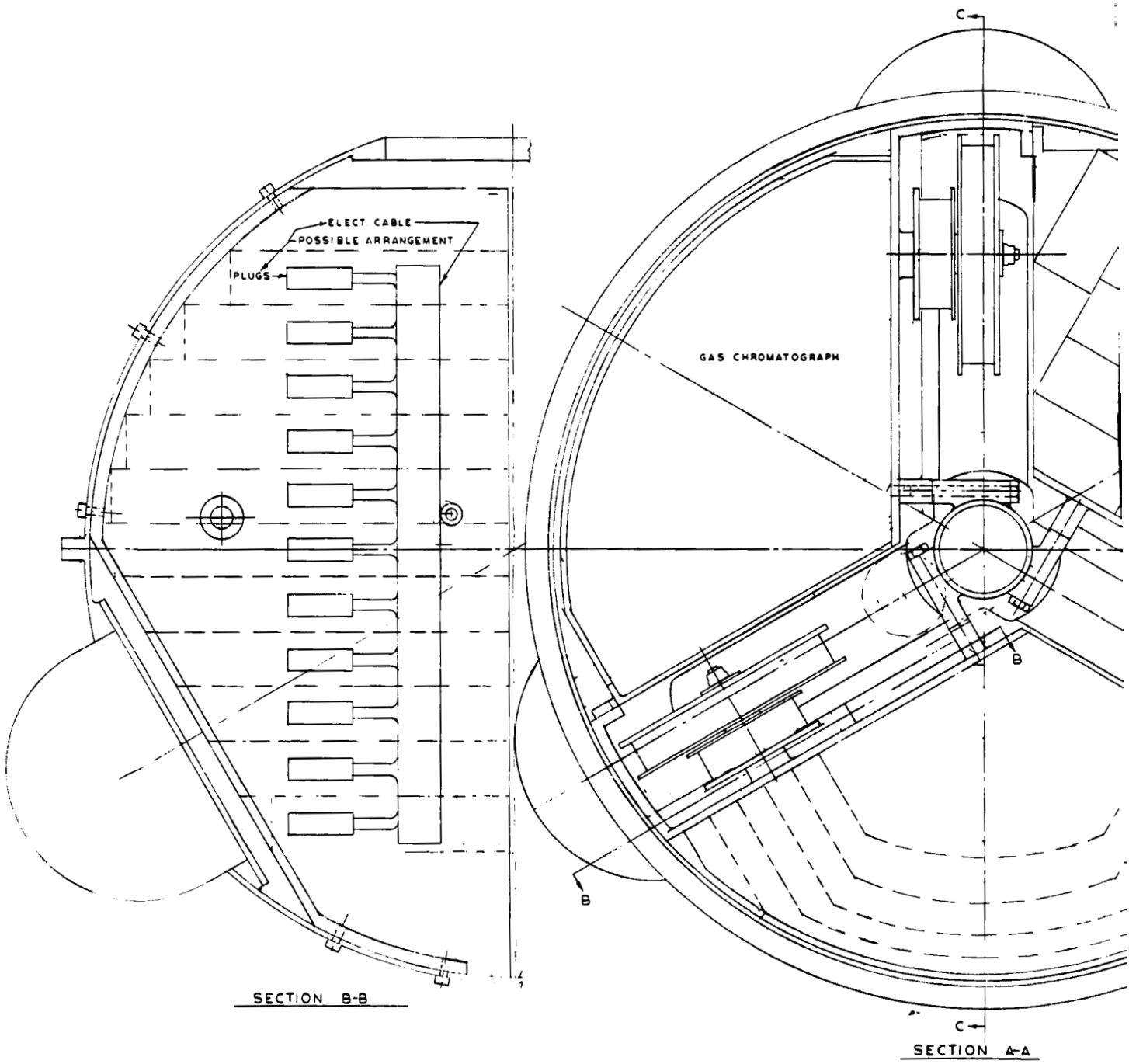

SECTION B-B

SECTION A-A

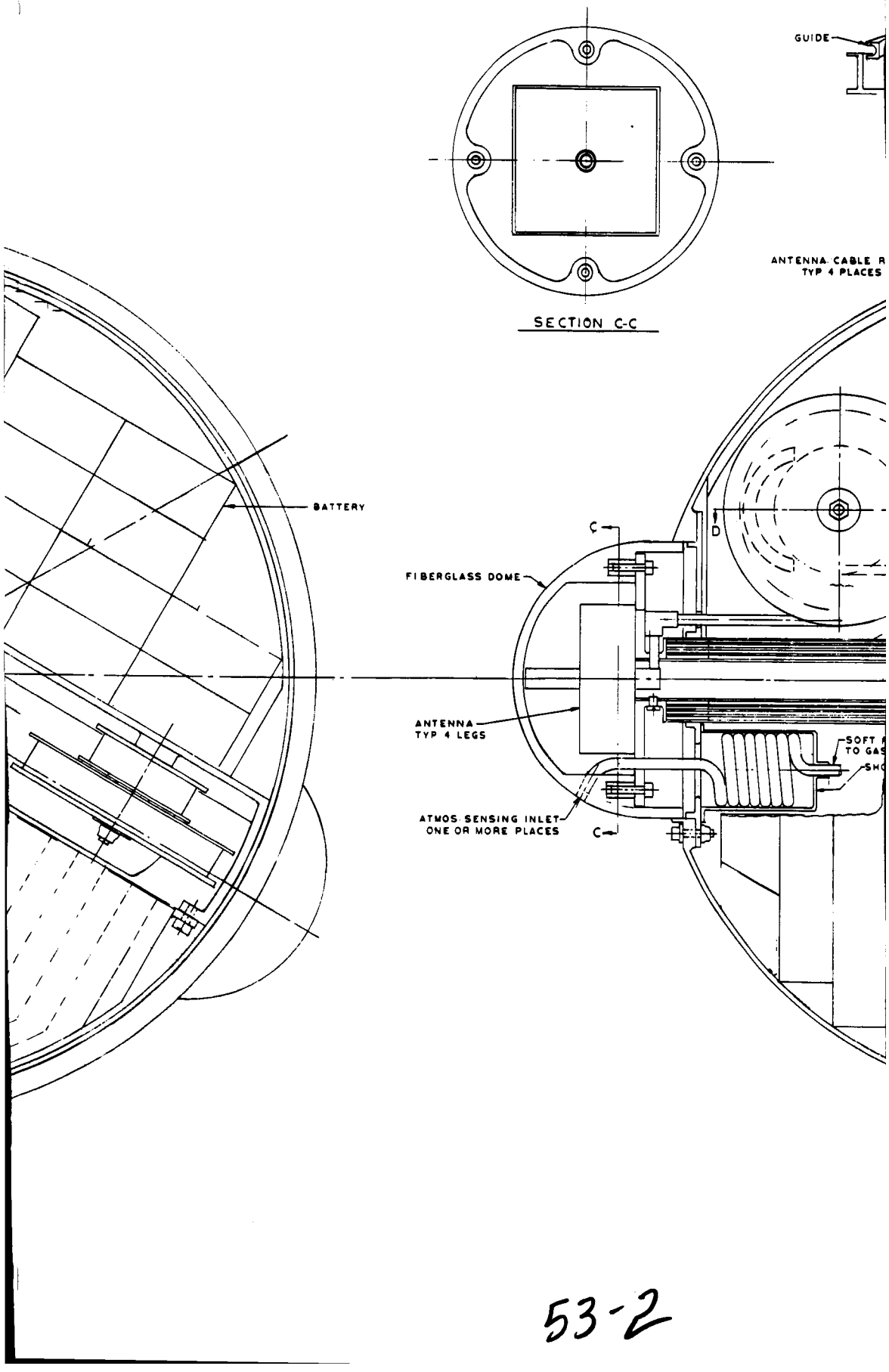
GUIDE
ANTENNA CABLE R
TYP 4 PLACES
SECTION C-C
BATTERY
C
D
FIBERGLASS DOME
ANTENNA
TYP 4 LEGS
SOFT
TO GA
SH
ATMOS SENSING INLET
ONE OR MORE PLACES
C

53-2

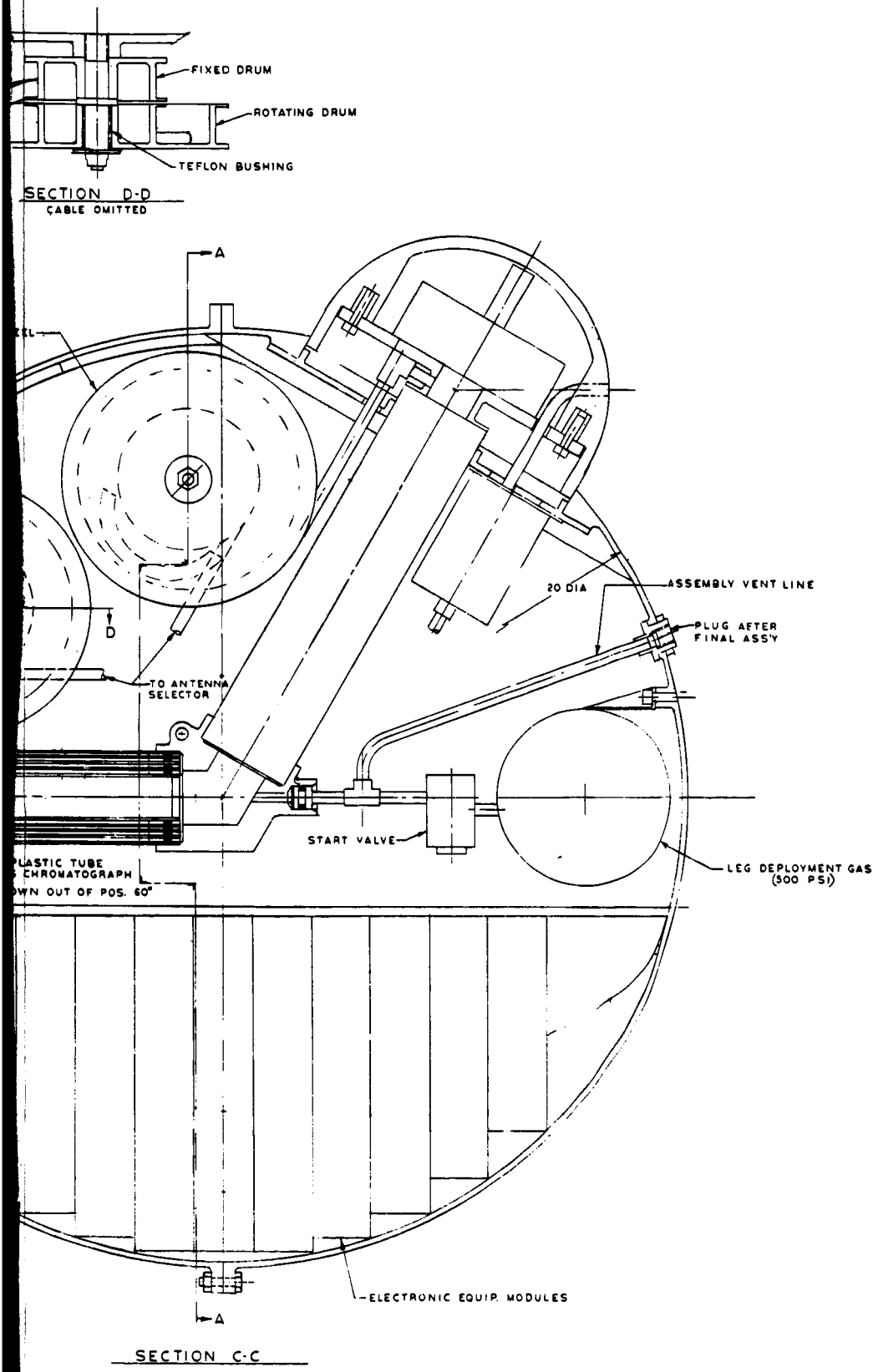

Fig. 51. Extendable-leg lander configuration

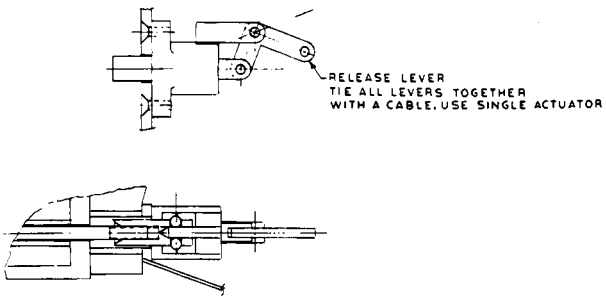

RELEASE MECHANISM
SAME FOR PAYLOAD TO LANDER, COVERS, AND PARACHUTE.
FULL SIZE

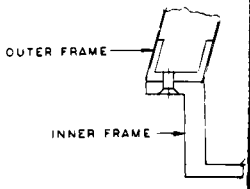

FRAME ASSEMBL
FULL SIZE

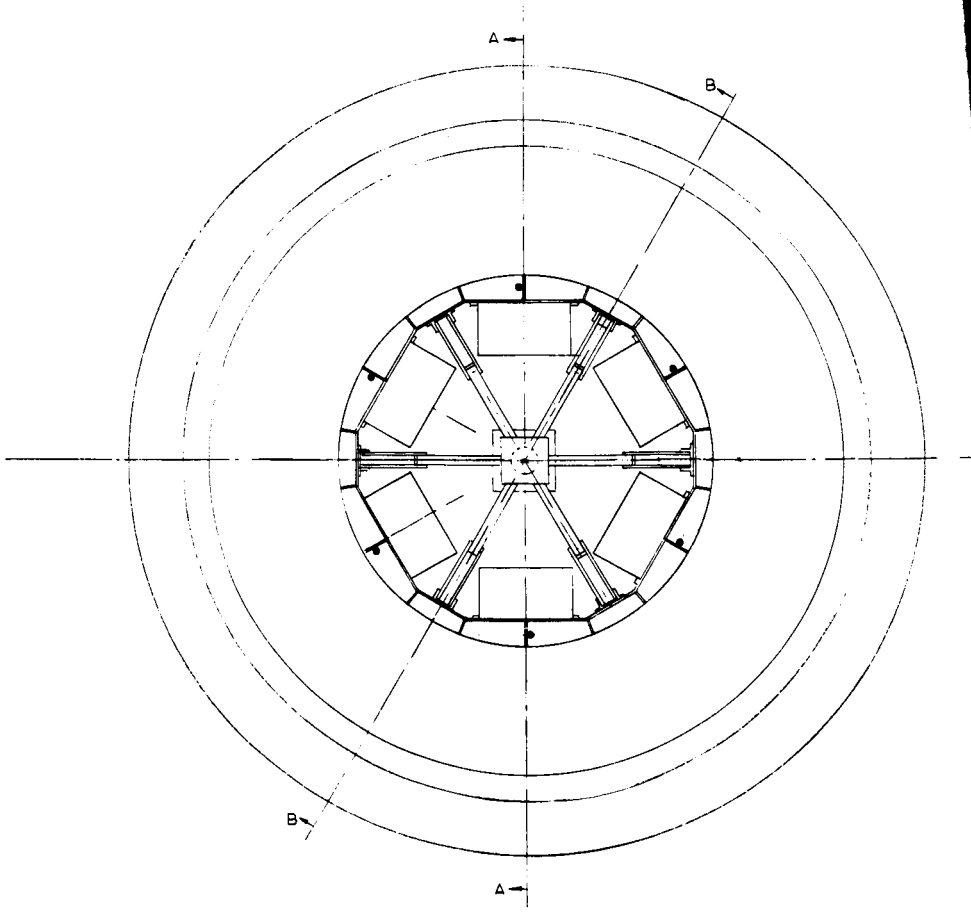

Fig. 52. Semi-selective orientation configuration (lenticular)

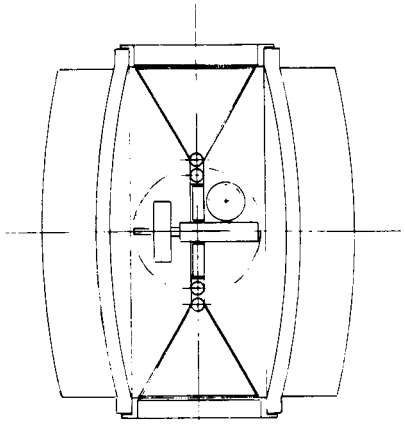

ALTERNATE ANTENNA ARRANGEMENT
USING ONE ANTENNA AND GIMBAL

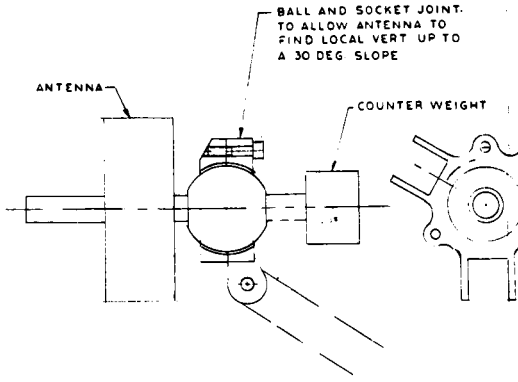

ANTENNA SUPPORT
FULL SIZE

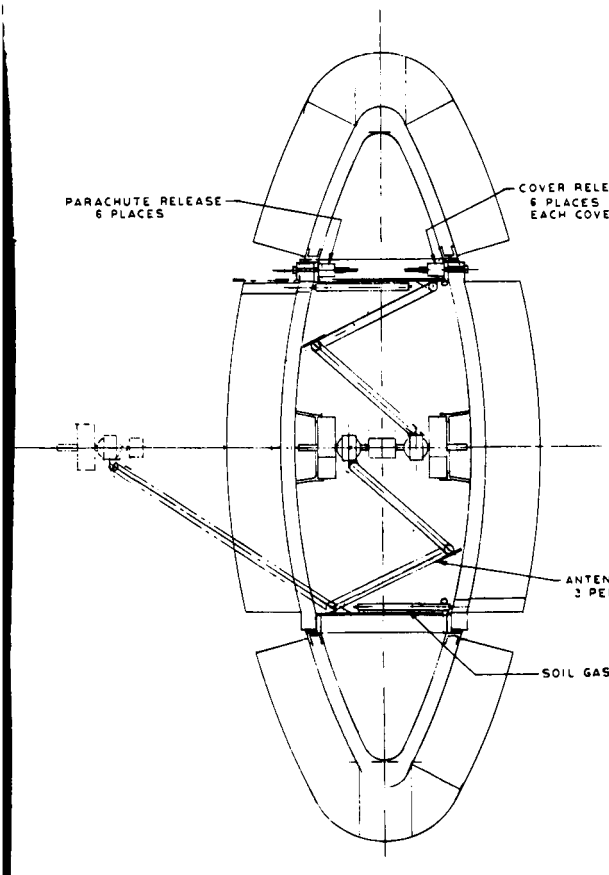

SECTION B-B

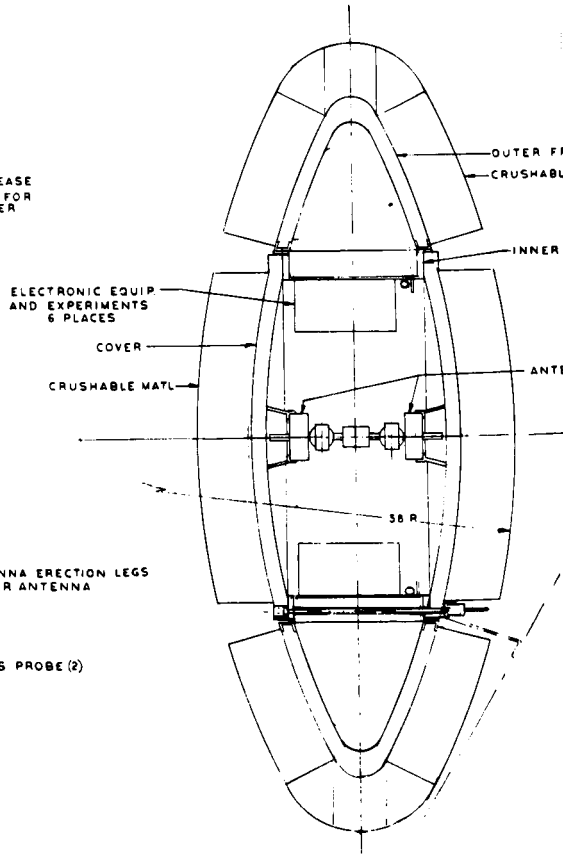

SECTION A-A

54.2

the resultant penalty of being off local vertical by the amount the payload orientation exceeds the design condition. It is not clear without detail design that the degree of freedom requiring 180-deg rotation could be safeguarded from physical interference if the design condition were exceeded.

3. Use of rf rotating joints across platform gimbals.

4. The "automatic" orientation feature of this geometry is the least positive and therefore the most susceptible to Mars surface obstructions and embedment in soft surfaces. This reservation is similar to the so-called "automatic" orientation feature of spherical payloads with eccentric center of gravity.

5. Approach E: Semi-Selective Orientation Configuration (Spherical Shape)

Because of the reasonable compromise of the "either-of-two orientations" contained in Approach D, a more positive method of obtaining the desired orientation was developed. While there is some difference in weight distribution from Approach D, the overall weight and adaptability to science instrumentation are the same and are not included in Table 11.

The landed geometry assumes a spherical payload configuration to eliminate the higher shock levels and structural weight penalties associated with the lenticular shape. After impact, the impact attenuator would be removed and a toroidal orientation bag would be inflated. (Such a bag is also mentioned in passing as a stabilizer for the floated payload requiring external sensor deployment.) Much attention was devoted to methods of payload orientation to at least local terrain reference. The toroidal bag seems to provide the best solution to the broad scope of terrain possibilities. By inflating at a slow rate to 1 psia (instead of instantaneous), the toroid will provide considerable mobility and versatility in extricating itself and orienting to the broad base. The toroidal bag will be fabricated of tear resistant material and sectioned to minimize effects of puncture. The spherical payload is supported in the center cavity of the toroid bag (suspended above the Mars surface) as shown in Fig. 53. Exact sizing of the bag and the attachment method require a great deal more consideration of detail conditions; however, for purposes of estimating weight, a toroidal section of 3-ft diameter (per circular section) is reasonable. Once the local terrain orientation has been established (inflation complete), the payload will deploy an antenna and science sensors, the latter requiring free-stream exposure, thus exposing the internal payload to the Mars environment for science instrumentation measurement. A boom is deployed downward to obtain soil measurements and sampling. The gimbal platform mentioned under Approach D is not applicable to spherical payloads as no useful area is left for packaging for a sphere of reasonable size.

In summary, the electromechanical operations required for an either-side-up lander (originally spherical shape) are:

1. Retraction of electrical umbilical prior to landing.

2. Impact limiter removal.

3. Gas bag inflation for orientation.

4. Antenna and soil gas sensor deployment.

Configuration-peculiar problems are:

1. The storing of the orientation bag and attachments, such that impact loads can be withstood.

2. Deployment of electrical and rf cable for antenna and science extension.

6. Summary

Several general considerations can be stated for short-life landers:

1. The configurations and therefore the post-landing operations are very sensitive to the amount and type of experimentation proposed for the mission. For example, on the basis of the foregoing considerations, one might decide upon:

   a. A flotation orientation (Approach B) if the science experiments were limited to gas analysis and pressure determination.

   b. An "either-side-up" approach, using a toroidal gas bag for orientation (Approach E) for missions requiring external exposure and access for conditions where surface environment was extremely uncertain (i.e., Mars dark area landing site).

   c. An extendable-leg orientation (Approach C) for missions requiring external exposure and access but where there is relative agreement on the Mars terrain to be encountered (i.e., a landing in a light area).

2. Some specific electromechanical operations that are likely require considerable advanced development. For example,
   a. Although development work has been done in the area of impact limiter removal, the operation under mission conditions (i.e., sterilization with its attendant effect upon payload electronics) must be more fully understood.
   b. Deployment mechanisms and gimbals capable of surviving high impact conditions require some development.
   c. Ruggedized packaging techniques for high-velocity impact survival and adaptable to spherical payload configurations must receive further consideration. Experience with the lunar landing capsule represents a starting point. However, special problems are posed by the amount and type of proposed science instrumentation in this area.
3. The configurations are strongly limited by assuming the presence of an omnidirectional impact limiter and the requirement to orient from a random orientation. Assurance of directional impact and final orientation would greatly simplify post-impact electromechanical operations and open up a great number of configuration possibilities.

B. Long-Life Landed Payload Considerations: 50 to 125 lb of Scientific Instruments

In order to "break new ground" for configuration and electromechanical operations on the Mars surface, a number of assumptions are made regarding mission objectives. This is primarily to avoid an unrealistic extrapolation of configurations developed under Section B to accommodate the larger scientific payloads.

The assumptions made are requirements consistent with the amount of sophistication required to satisfactorily accomplish a mission utilizing 50 to 125 lb of scientific instrumentation. These assumed requirements are:

1. A 6-month operating life time on the surface of Mars. The power source assumed to fulfill this requirement is a 175-watt raw output radioisotope thermoelectric generator (RTG) Rankine closed loop system.
2. A direct-link, S-band communication system with 10 bit/sec capability over 380×10^6 km. A medium-gain antenna (10-12 db) capable of tracking Earth was assumed to fulfill this requirement.
3. A requirement for taking 0.1- to 1-gram surface samples for growth and specific analysis experiments was assumed.

Because of the time constraints of the study and the dependence of such a study on the output of several concurrent investigations (i.e., RTG power source evaluation and directional antenna considerations), specific configurations applicable to the type of mission assumed were not developed. The study emphasized the factors controlling the general approach of applicable configurations. A consideration of these factors follows:

1. Effects of RTG Power Source on Configuration and Operations

There are three major configuration constraints imposed by the RTG power supply: (1) approximately 15 sq ft of unobstructed radiator area must be exposed to the Mars atmosphere after impact; (2) the scientific instrumentation (and other radiation-sensitive electronics) must be isolated from the RTG background by a combination of geometry and shielding—the degree of isolation required must be further evaluated; (3) the RTG power source location must be compatible with the thermal control requirements of the electronics subsystems.

2. Effects of Pointable Antenna on Configuration and Operations

The mechanization of the antenna drive system for tracking Earth may vary from one degree of freedom to six degrees of freedom, depending on the antenna pattern used and the orientation of the rest of the basic lander. It is assumed that the antenna used requires two degrees of freedom (azimuth and elevation) from a local vertical reference. The major effects of this type of antenna mechanization on the over-all configuration are: (1) a selective orientation of the basic vehicle—the basic vehicle or a reference platform on the vehicle must establish local vertical as reference for antenna articulation; (2) unobstructed physical clearance and line-of-sight view throughout the articulation range; (3) structural support of the antenna during entry and impact.

3. Effects of Surface-Sampling Mechanisms on Configuration and Operations

While a definite mechanization of the surface-sample gathering and processing experiments is not known at this time, it is obvious that a known gross orientation and some degree of access and orientation is required.

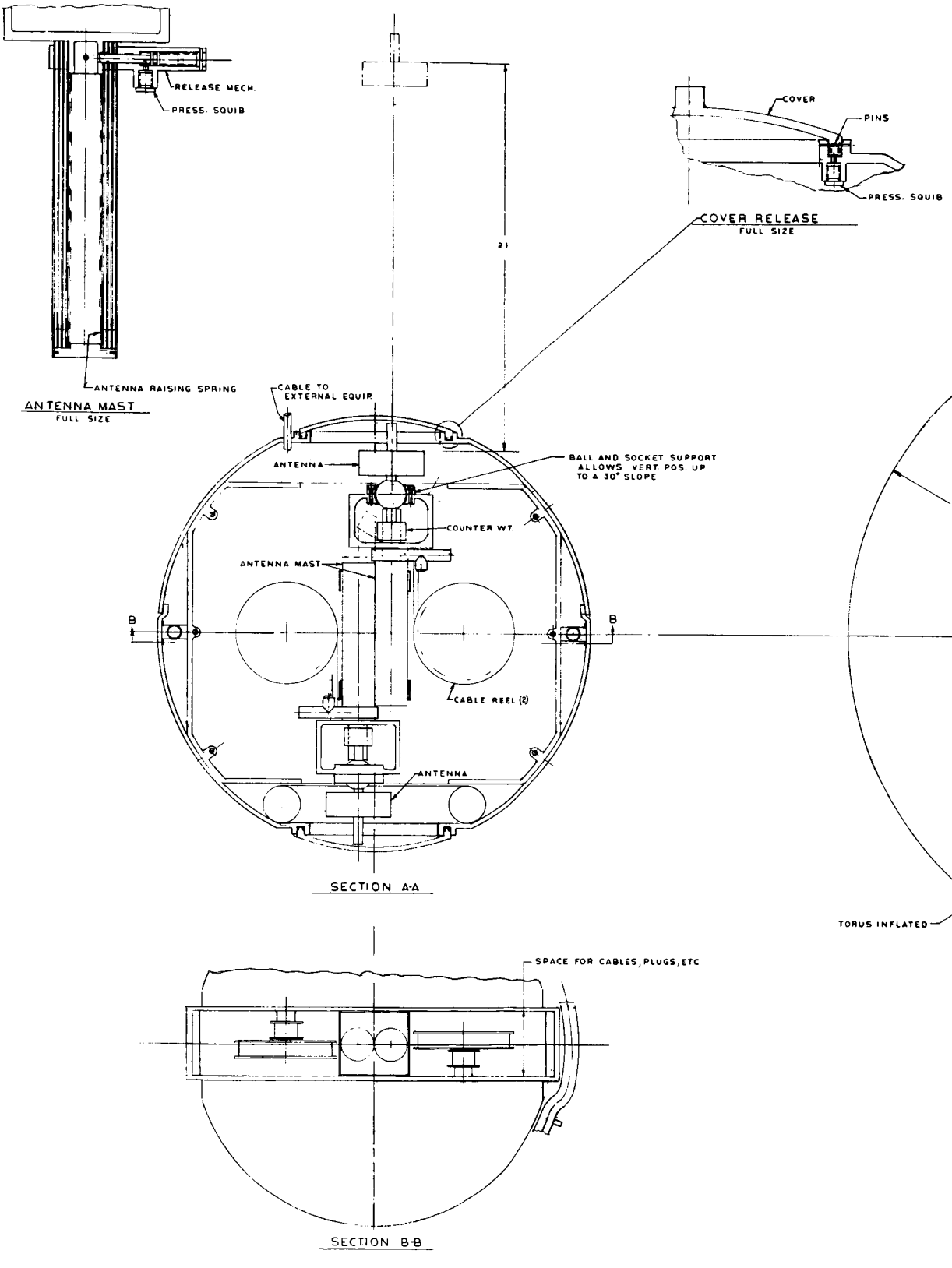
RELEASE MECH.
PRESS. SQUIB
ANTENNA RAISING SPRING
ANTENNA MAST
FULL SIZE
COVER
PINS
PRESS. SQUIB
COVER RELEASE
FULL SIZE
21
CABLE TO EXTERNAL EQUIP
ANTENNA
BALL AND SOCKET SUPPORT ALLOWS VERT POS. UP TO A 30° SLOPE
COUNTER WT.
ANTENNA MAST
B
B
CABLE REEL (2)
ANTENNA
SECTION A-A
36 DIA
TORUS INFLATED
SPACE FOR CABLES, PLUGS, ETC
SECTION B-B

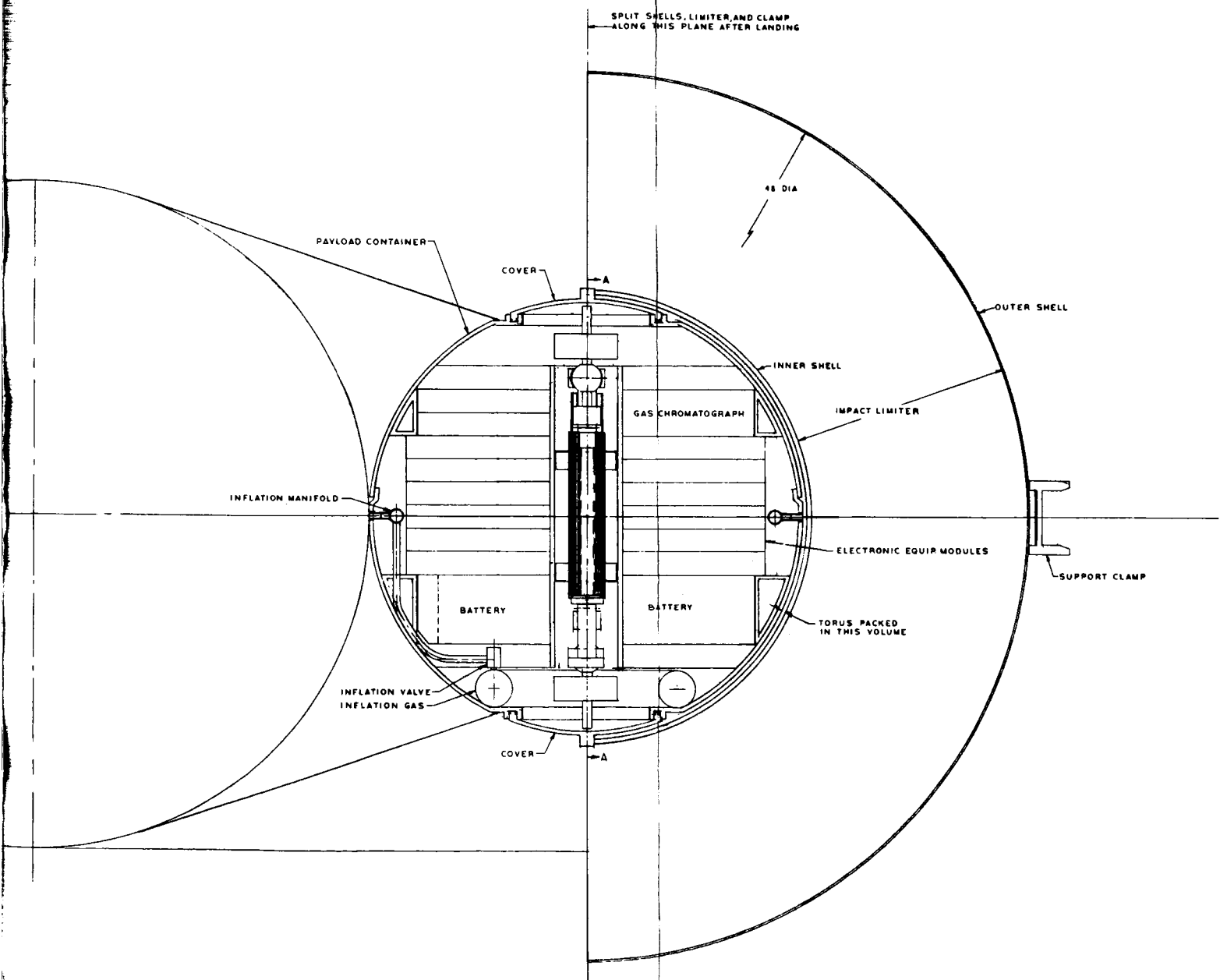

Fig. 53. Semi-selective orientation configuration (spherical shape)

4. Summary

From the gross consideration of the preceding factors, some general statements regarding configuration can be made:

a. Landing mode. It seems an obvious conclusion that an omnidirectional impact orientation is not feasible. There are a number of factors that determine this fact: (1) the useful weight of the lander (approximately 1000 lb) would make an omnidirectional impact attenuation system very heavy; (2) experiment and antenna access requirements; and (3) RTG radiator requirements. The feasibility of such a mission as outlined in this section is dependent upon a landing system that controls post-landing impact orientation within known limits or a definition of the Mars environment that assures a known post-landing orientation. Figures 54 through 56 illustrate, on a gross and simplified basis, the critical effect of landing environment on vehicle stability. From these curves (based on a lenticular configuration, but indicative of other configurations), the following observations concerning landing stability can be made:

1. Unless the Mars landing site is known well enough to assure that horizontal velocity can be dissipated by skidding, the horizontal velocity vector must be closely controlled for appreciable impact velocities (>50 ft/sec).
2. Ground slope strongly influences landing stability. For impact velocities in excess of 50 ft/sec, a ground slope less than 5 deg is required for a small horizontal velocity vector (5 deg or less from local vertical downslope).

The environmental constraints and effects noted above indicate in summary that unless the environmental conditions on Mars are very favorable (i.e., no wind, level

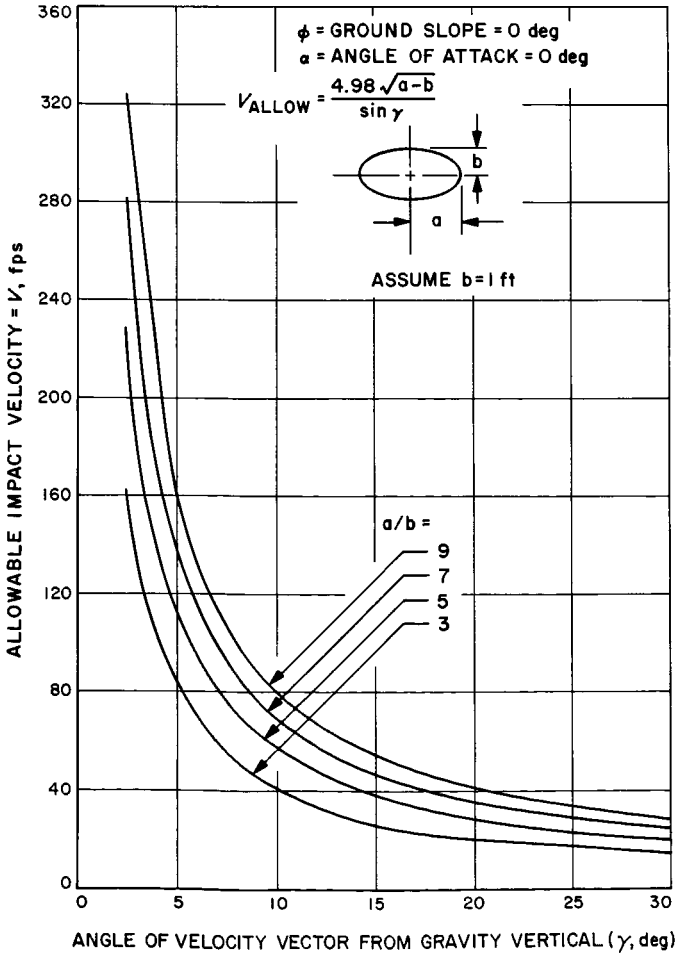

Fig. 54. Effect of horizontal velocity and geometric shape on landing stability

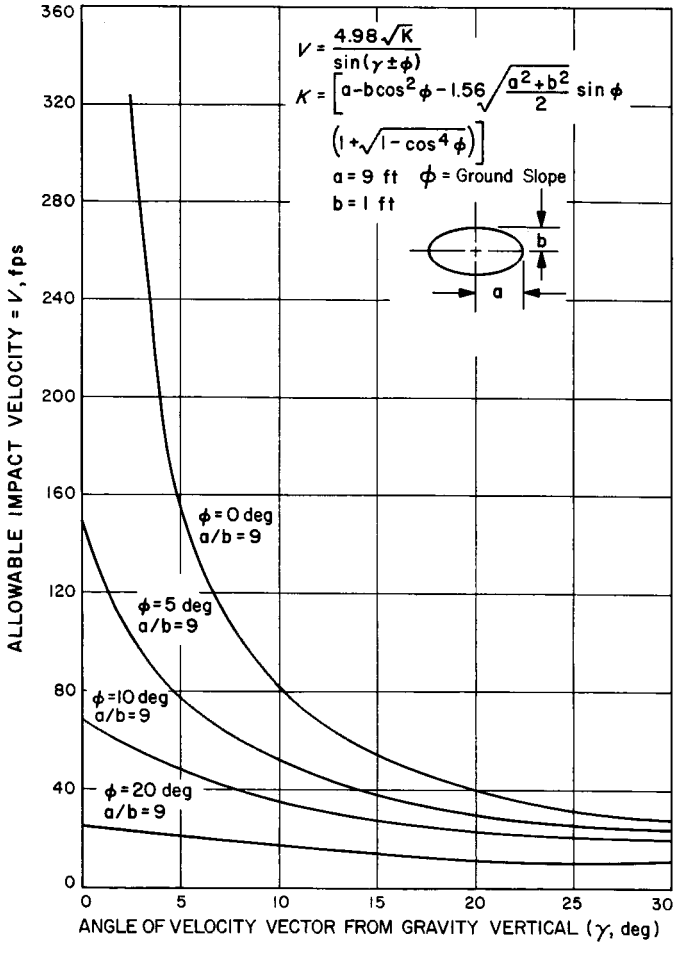

Fig. 55. Effect of horizontal velocity vector and ground slope on landing stability

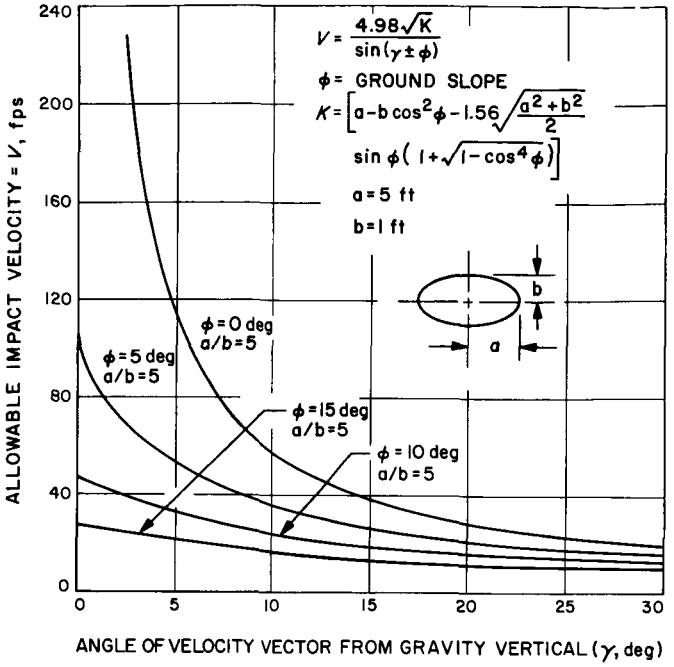

Fig. 56. Effect of horizontal velocity vector and ground slope on landing stability

ground, no obstacles or local depressions) and entry conditions extremely well defined (no vehicle oscillation, etc.) an active retrorocket system capable of controlling landing velocities and directions to very close limits will be required to maintain a known orientation during and after impact.

b. Post-landing operations. The major electromechanical operations after landing will be associated with establishing communications and starting scientific experimentation. Probable operations are:

1. Establishment of local vertical reference by vehicle leveling or uncaging of a gimballed platform.

2. Azimuth orientation of antenna to north pole reference.

3. Antenna deployment and Earth tracking.

4. Experiment exposure to applicable environment and deployment of sample-gathering devices.

5. Conclusion

A Mars landing vehicle capable of conducting sophisticated scientific experiments consistent with 50–125 lb of science instrumentation will have configuration and operational constraints incompatible with the "buttoned-up" configurations characteristic of omnidirectional impact landers. In order to maintain the necessary impact limits necessary for a known orientation during and after impact, it is probable that an active retrorocket landing system will be required.

C. *Spherical Gas-Filled Balloons — Mars Payload Terminal Decelerator and Impact Attenuator*

During a recent brief study of omnidirectional impact limiting techniques, a comparison was made between gas-filled balloon impact attenuators and spherical impact attenuators made from balsa wood. In this comparison the results of an analysis by E. Dale Martin and John T. Howe of Ames Research Center (Ref. 14) were used in sizing gas-filled balloon impact limiters, with extra weight allowances being added for rip stop cords in the balloon skin, for attachment of payload support cords to the balloon skin, and for balloon inflation apparatus. For a given impact velocity, the calculated balloon weights were less than the weights of balsa coverings; further, it is unrealistic to compare the two types of impact limiters for the same terminal or impact velocity. A capsule payload may either land with part of the entry body at velocities around 500 ft/sec or may be ejected from the entry body and land at its own terminal velocity (with or without an auxiliary parachute).

A typical payload using balsa wood as an impact attenuator may either land at about 600 ft/sec inside the entry body or be ejected and land separately at about 130 ft/sec with a parachute. In contrast, the gas-filled balloon can be designed as its own decelerator with a terminal velocity around 150 ft/sec, thereby combining the relative simplicity of inflating a sphere with the relatively low impact velocity of a parachute descent. An important point is that the gas-filled balloon can be designed to have a low descent velocity with no significant weight penalty while the balsa-covered payload must give up 10% of its own weight to a parachute if it is to land with a low descent velocity. As a sidelight, we might note that this entire discussion is concerned with dissipation of the impact velocity normal to the impacted surface. Dissipation of velocity tangent to the surface may be considered to require an appropriate additional amount of energy absorption material in either the balsa-wrapped or the gas-filled balloon impact limiting techniques.

1. Description of Gas-Filled Balloon Design and Operation

The gas-filled balloon impact limiter is simply a spherical balloon made of high-strength, relatively inextensible material, into the center of which is tied a payload on high-strength, relatively inextensible cords. The balloon absorbs impact energy by compressing its contained gas; then that energy is dissipated by release of the gas as the payload's vertical velocity approaches zero.

A typical landing operation would have an entry body carry the balloon-shrouded payload into the Martian atmosphere, slowing to a velocity between 600 and 1,000 ft/sec. The balloon-wrapped payload would then be ejected from the entry body and the balloon inflated, thereby slowing to a terminal velocity around 150 ft/sec. The payload would impact the Martian surface, compressing the balloon to approximately half its original volume and coming to a stop a couple of feet above the ground. As the payload comes to a stop, it releases the payload-to-balloon-skin attach cords; and the unrestrained balloon skin ruptures, expelling the previously entrained gas and clearing the payload to begin its operation.

2. Desirable Features of Balloon Impact Limiters

The balloon impact limiter offers several advantages over a balsa payload covering. One advantage previously mentioned is the inherently low impact velocity resulting from large size. An additional advantage of large size is the balloon's ability to land on an uneven surface without large projections penetrating to the payload. Furthermore, since the impacting balloon decelerates through a considerable distance, it imposes a relatively low (100 to 150 g) impact load on the payload as compared to the relatively high (3,000 to 5,000 g) impact load imposed by a crushable balsa-wood impact attenuator. It may be noted that payload designs for high-g-level, long-pulse-duration accelerations generally utilize a large percentage of their total weight for mechanical structure, leaving a relatively small percentage of payload weight for electronic equipment and scientific experiments.

3. Problems Associated with Balloon Impact Limiters

It seems natural that a device offering significant advantages would also present significant problems to the potential user; and in this respect the balloon impact limiter seems anxious to comply. The most obvious problem is the likelihood of a puncture occurring at impact, with a resultant rupture of the skin and loss of gas pressure. Calculations indicate that a very large tear (20 sq ft) is necessary to significantly depressurize and degrade the performance of a typical (26-ft-diameter) balloon. This is due to the short (70-millisec) duration of the impact. It appears from the leakage calculations that any normal puncture or tear at impact is no problem, and that only a catastrophic rupture of the entire balloon need be prevented for a successful soft landing. The criterion for prevention of a catastrophic rupture is that the balloon skin be ductile, with relatively large elongation after yield. This ductility insures that a sharp tear will yield into a circular hole with a stress concentration factor of about two. There are several rip-stopped fabrics and scrimmed film laminates which behave in this ductile manner, and all that need be done to prevent catastrophic balloon rupture is to make the balloon of such a material, with the design stress less than half of the material's yield stress.

A second problem which arises is the possibility that a very large hole will be ripped in the bottom of the balloon because of a high horizontal velocity imparted by winds and sloping ground. This hole might then turn up away from the ground and vent out the side of the balloon. The dynamics of such an event are difficult to analyze, and testing should be done to explain such behavior; however, a fairly conservative analysis shows that even for horizontal velocities as large as the vertical impact velocity, a hole ripped in the bottom of the balloon cannot turn up to the side for venting, and instead, impact deformation causes the upper portion of the balloon to come down and shroud the hole, thereby preventing leakage.

A third problem with the balloon impact limiter is how to time the payload-to-skin cord release so that the payload is at rest just as the cords are released. No detailed solution to the problem has been proposed during this brief study. However, the timing requirements (to within a few milliseconds) are not inconsistent with frequency response of accelerometers and position sensors which might be considered release-triggering sensors.

A fourth problem which must be considered is imposed by the sheer size of a gas-bag impact limiter: viz., the problem of testing a full-scale limiter to see if it actually works. Scale-model testing can easily be done on models up to about 6 ft in diameter with simple air gun accelerator inside a low-pressure (high-altitude) chamber. Full-scale testing might be accomplished with some sort of powered sled which would drive the large (26-ft-diameter) balloon into a target, but it is necessary to have the environmental pressure as low (0.2 psi) as that

on the Martian surface because the balloon's behavior varies as a function of external pressure.

A fifth problem which must be considered is that of balloon fabrication. Some very real problems develop when consideration is given to the details of attaching the payload support cords to the balloon skin without imposing severe stress concentrations on the skin. Some details of this design are presently being worked out as the study continues. It appears that no great concessions will have to be made to the real world, and, instead, that actual hardware will come fairly close to theoretical assumptions.

4. Conclusion

In summary, it appears that the relatively fragile-looking balloon impact limiter can withstand the rigors of a skidding tearing landing on a hostile jagged surface and still properly cushion its internally supported payload. At least to this point, no calculation has demonstrated that the balloon impact limiter will not withstand such an environment.

The balloon study is continuing in an effort to determine whether or not these preliminary conclusions are valid and to establish the feasibility of a gas-filled balloon impact limiter on an actual Mars lander design.

XII. CAPSULE WEIGHT SUMMARY

The guidelines for this study called for pursuing the configuration of a ballistic entry mode with a parachute experiment and, using the same capsule shell structure, a two-stage parachute terminal decelerator mode. The impact attenuator study showed that there was no science payload possible in the ballistic mode for the impact velocity determined in the entry trajectory calculations.

The parachute mode offers some potential for getting a payload on the surface because the descent velocity can be effectively reduced to about 130 ft/sec. The ballistic coefficient can be increased to approximately 0.25 and maintain velocity–altitude conditions acceptable for parachute deployment. These factors result in a landed payload for the 90-deg entry angle case. Further gains can be made in landed payload by decreasing the entry angle because the deceleration levels for which the structure must be designed decrease by at least a factor of two. These gains can be achieved by dropping the desired objectives of "one capsule shell for all missions" and designing to the lower deceleration values.

Table 12 presents an estimated weight breakdown for the various modes just described. The significant value is the weight available for the landed payload system. The allocation of this weight to the payload and attenuator comes from Section VIII and is highly dependent on the impact velocity and the assumed Mars environment. Though the impact velocity for the ballistic modes is so high that there is no landed payload, weights are given. In the case of the two-stage parachute mode, the center of gravity (Table 13) is well out of the acceptable limit of $0.17D$ as defined by the trajectories calculated. No iterations have been made to determine how critical the farther-aft center of gravity really is, but it is expected that a rearward entry instability problem may exist, since the center of pressure is at approximately $0.2D$. However, a single-stage subsonic parachute mode, at low angle of entry, could be a very possible mode of entry. The impact velocity would be down from the ballistic, and the center-of-gravity location could probably be tolerated. Add to these conditions an attitude-controlled 90-deg maximum angle of attack at entry, and it is most likely that a mission would be feasible.

Table 12. Weight summary: 16-ft-diameter *Apollo*-type capsule

Mode (V_{entry}, 25,000 ft/sec)	Ballistic mode	Ballistic and subsonic parachute experiment	2-stage parachute, 90-deg entry	2-stage parachute, 45-deg entry
Ballistic coefficient, slugs/ft²	0.17	0.17	0.25	0.25
Impact velocity, ft/sec	505	505	130 (vertical)	130 (vertical)
Entry weight	1540 lb	1540 lb	2260 lb	2260 lb
Shell structure weight	735	735	921	709 (100 g)
Heat shield weight	330[a]	330[a]	386[b]	365[c]
Solar array (20 ft²)	10	10	10	10
Attitude control	60	60	60	60
Assembly joint—shell	20	20	20	20
Aft cone separation joint and mechanism	—	45	31	31
Subtotal	1155	1200	1428	1195
Weight available for parachute and payload	385 lb	340 lb	832 lb	1065 lb
Supersonic chute	—	—	233	233
Subsonic chute	—	39	57	94
Sensors	—	10	10	10
Subtotal	—	49	300	337
Weight available for payload	385 lb	291 lb	532 lb	728 lb
Biological assay guarantee	10	10	10	10
Descent payload				
Science	10	10	10	10
Communications	25	25	35	35
Support equipment	40	40	40	40
Support structure	45	40	40	40
Payload separation and pyro	—	26	26	26
Umbilical and cabling	8	8	8	8
Subtotal	138	159	169	169
Weight available for landed payload system	247 lb	132 lb	363 lb	559 lb
Landed payload system				
Cover			21	21
Attenuator (10 cm rock, 100 ft/sec wind)	Impact velocity too high for landed payload		236	297
Landed payload	None	None	106	241

[a]Forebody, 1 lb/ft²; aftbody, 0.25 lb/ft² (should be 0.38 lb/ft²).
[b]Forebody, 1.05 lb/ft²; aftbody, 0.41 lb/ft².
[c]Forebody, 1 lb/ft²; aftbody, 0.36 lb/ft².

Table 13. Center-of-gravity calculation
(Center-of-gravity location used in trajectory calculations = 0.17*D* = 32.6 in. from forebody; center of pressure approximately 0.2*D* from forebody reference = 38.4 in.; cg must be forward of cp or body is unstable; Z is measured from forebody surface at the capsule centerline)

Item	Ballistic		Ballistic and subsonic parachute experiment		2-stage parachute, 90-deg entry		2-stage parachute, 45-deg entry	
	Wt., lb	Z, in.	Wt., lb	Z, in.	Wt., lb	Z, in.	Wt., lb	Z, in.
Structure	735	42	735	42	921	42	709	42
Heat shield	330	39	330	39	386	39	365	39
Solar array	10	43	10	43	10	43	10	43
A/C	60	12	60	12	60	12	60	12
Assembly joint	20	33	20	33	20	33	20	33
Separation joint	—	—	45	33	31	33	31	33
Supersonic parachute	—	—	—	—	233	125	233	125
Subsonic parachute	—	—	39	67	57	67	94	67
Sensors	—	—	10	14	10	14	10	14
Biological assay	10	30	10	30	10	33	10	33
Descent science	10	15	10	15	10	15	10	15
Communications	25	41	25	41	35	78	35	78
Support equipment	40	15	40	15	40	15	40	15
Separation structure	45	30	40	30	40	30	40	30
Separation joint	—	—	26	20	26	20	26	20
Cabling	8	20	8	20	8	20	8	20
Payload system	247	33	132	33	363	30	559	30
Total	1540	37.2	1540	37.7	2260	47.0	2260	46.4

REFERENCES

1. "Mariner Mars 1969 Lander Technical Feasibility Study," JPL internal communication.
2. *Mars Entry Capsule Shape Study*, Technical Memorandum No. 33-233, Jet Propulsion Laboratory, Pasadena (to be published).
3. Spencer, D. F., *Mars Engineering Atmosphere and Surface Models*, Technical Memorandum No. 33-234, Jet Propulsion Laboratory, Pasadena, July 6, 1965.
4. Speigel, J. M., private communication.
5. Swann, Robert T., and Pittman, Claud M., *Numerical Analysis of the Transient Response of Advanced Thermal Protection Systems for Atmospheric Entry*, TN D-1370, NASA, Washington, D. C., July 1962.
6. Nagler, Robert G., *Preliminary Analysis of the Importance of Materials Properties and Thermal Inputs on Heat Shields for Mars Entry*, Technical Memorandum No. 33-209, Jet Propulsion Laboratory, Pasadena, June 1, 1965.
7. John, R., Hoercher, H., Mitchel, B., Recesso, J., O'Connor, T., Debolt, H., Hanset, P., and Rosensweig, R., *Arc-Heater Characterization of Ablative Plastics*, ML-TRD-64-191, October 1964.

REFERENCES (Cont'd)

8. Lundell, John R., Wakefield, Roy, M., and Jones, Jerold, W., "Experimental Investigation of a Charring Ablative Material Exposed to Combined Convective and Radiative Heating in Oxidizing and Non-Oxidizing Environments," AIAA Entry Technology Conference, Williamsburg, Virginia, October 12-14, 1964.
9. Stuart, J. W., private communication.
10. Wolf, Fred, private communication.
11. *Collected Papers on Instability of Shell Structures*, TN D-1510, NASA, Washington, D. C., 1962.
12. *Study of a High Resolution Facsimile System Experiment on the Surface of the Planet Mars*, Publication, No. U-3034, Final Technical Report, Aeronutronic Division of Philco Corporation, February 25, 1965.
13. *Proposal for Ranger TV Sphere*, Report No. SGC P-3221A, Space General Corp., El Monte, Calif., October 24, 1963.
14. Martin, Dale, E., *A Design Study of the Inflated Sphere Landing Vehicle, Including the Landing Performance and the Effects of Deviations from Design Conditions*, TN 692, NASA, Washington, D. C., April 1961.